# SELF-ASSEMBLY OF MAGNESIUM ALUMINATE DUE TO DEWETTING OF OVERLAID GOLD THIN FILM

# SELF-ASSEMBLY OF MAGNESIUM ALUMINATE DUE TO DEWETTING OF OVERLAID GOLD THIN FILM

By Pouya Hosseini Vajargah, B. SC.

A Thesis Submitted to the School of Graduate Studies in Partial Fulfilment of the Requirements for the Degree Master of Applied Science

McMaster University © Copyright by Pouya Hosseini Vajargah, July 2016

McMaster University MASTER OF APPLIED SCIENCE (2016) Hamilton, Ontario (Engineering Physics)

TITLE: Self-assembly of Magnesium Aluminate due to Dewetting of Overlaid Gold Thin Film

AUTHOR: Pouya Hosseini Vajargah, B.Sc. (McMaster University)

SUPERVISOR: Professor John S. Preston

NUMBER OF PAGES: ix, 125

## Abstract

THE self-assembly of magnesium aluminate spinel as a result of dewetting an overlaid thin film of (chiefly) gold was investigated. Thin films of gold were deposited on single-crystalline spinel substrates and were heat-treated to dewet gold film which led to self-assembly of intricate structures consisting of faceted spherical particles atop of frustums. The current work was conducted in continuation of previous studies which reported formation of such intricate structures. The most recent studies had evidently overruled a pure gold self-assembly scenario as was pointed out in preliminary investigations. It was in fact proven that these structures consist of three distinct parts: (i) a single or polycrystalline gold faceted sphere, (ii) quasi-phase interfacial bilayer, and (iii) a crystalline $MgAl_2O_4$ necking structure spontaneously risen from spinel substrate. In the current work, samples were produced through different film deposition methods of sputter, thermal evaporation, and e-beam evaporation coating which underwent thermal annealing to induce dewetting of gold film and subsequent self-assembly of intricate structures. Several characterization methods such as electron microscopy, X-ray energy dispersive spectroscopy, electron energy loss spectroscopy, and atom probe tomography were utilized to survey the different features of the intricate structures with focus on chemical analysis of the gold-spinel interface. The results rejected the previous findings about formation of interface complexion at the boundary of gold-spinel. It was found out that gold-spinel interface is in fact an ordinary metal-oxide boundary with sharp atomic distinction and no inter-diffusion or formation of interfacial complexion. It was further discovered that dewetting pure gold thin films does not result in formation of spinel self-assembly and existence of elemental impurities of copper (Cu) in the initial film is vital in development of such structures. Finally, it was concluded that chemical composition of metallic overlayer and the heat treatment parameters most fundamentally influence formation and physical characteristics of those self-assembled structures.

**Acknowledgements**

I would hereby like to express my acknowledgment and my utmost gratitude to all of those who made this work possible:

Firstly, my supervisor, professor John Stuart Preston, for accepting me as a Master's student into his group at McMaster. I have always enjoyed working with him under his supervision and learned a lot from him throughout my project. I appreciate his constant feedback and encouragement at time of conducting this project and writing this thesis. My Master's degree has been a very influential opportunity in my life for which I'm truly grateful to John.

Also all members of the *P*ulsed Laser Deposition lab during my presence there: Dr. Kristoffer Meinander, Dr. Gabriel Devenyi, Mrs. Tara Majdi, Mr. Stephen Jovanovic, Mr. Michael Cino, Ms. Carely Miki, Ms. S. Rida Zainab, Ms. Fatemeh Rezapour, Mr. Joshua Rideout, and Mr. David Drake for their scientific advice and deeply helpful discussions associated with my project.

All the staff and associate members of Canadian Center for Electron Microscopy (CCEM), especially to Dr. Brian Langelier for conducting Atom Probe Tomography (ATP), Mr. Travis Casagrande for conducting Focused Ion Beam (FIB) microscopy, Mr. Chris Butcher and Mr. Andy Duft for providing training and assistance with scanning electron microscope (SEM), sputter coating system, and light microscopy, Dr. Andreas Korinek for conducting High Resolution Transmission Electron Microscopy (HR-TEM).

Mr. James Garrett, of the Brockhouse Institute for Materials Research (BIMR), for his patience and great assistance with the furnace design and setup.

Mrs. Doris V. Stevanovic, Dr. Zhilin Peng, and Dr. Sharam Ghanad-Tavakoli, of the Center for Emerging Device Technology (CEDT) for training and assistance on the sputtering system, e-beam evaporation coating system, spin coating system, and diamond precision cutting system.

All my professors and instructors at McMaster and Engineering Physics department, especially, professor Dr. La Pierre, professor Dr. Mascher, and professor Dr. Botton, from whom I have learned a great deal.

And last but not least, my family, my dearest mother, father, sister and brother, for their unconditioned love and support, for their belief in me, and for their constant

encouragement and guidance throughout my life. I am especially thankful of my mom and my sister, Dr. Shahrzad Hosseini Vajargah-also a McMaster alumnus, for being the most supportive of my academic career.

# Contents

# List of Figures

# List of Tables

# Chapter 1

# Introduction and Literature Review

## 1.1 Overview

In the course of past few decades, the study of metallic nanoparticles has attracted attentions of scientists because of their diverse applications in nanotechnology. Metal nanoparticles have found numerous applications in fields of optoelectronics and biotechnology. In particular, oxide substrate supported nanoparticles of noble metals such as gold are frequently used as a platform to catalyze chemical reactions and promote growth of semiconducting nanowires [1, 2].

A facile method of producing large scale oxide supported gold nanoparticles is to dewet a thin layer of gold deposited on an oxide substrate. Since thermodynamic balance of surface tensions at the interface of metal-oxide systems is in favor of formation of discrete metal particles rather than continuous films, dewetting can easily render uniformly distributed particles of metal by breaking up the metal film. Dewetting is usually induced through thermally annealing the system [3].

There exist a significant body of scientific research with regards to studying the various aspects of dewetting process and its dynamics both in solid and liquid states. Most of these research studies have been carried out on systems involving gold film and an oxide substrate such as sapphire, illustrating the role of "high-energy" oxide surfaces in dewetting metastable metal films. It is assumed that as a result of high thermal resistivity and chemical durability of oxides, substrate remains intact during

the the whole process of dewetting.

In wake of recent findings, unprecedented evidence of a novel film-substrate interactions exclusive to gold-spinel system has emerged. This interaction is unique in that a simple process of heat treatment not only cause dewetting the metal film, but also affects the underlying substrate, or at least its surface, by promoting spontaneous self-assembly of spinel in shape of pyramidal crystals underneath the dewetted gold particles, which mimic the surface symmetry of the hosting substrate. This self-assembly process is taking place on an oxide material known for its chemical inertness and thermal resistivity.

This interesting behavior has been the subject of current study with primary aim of discovering the causes of the phenomenon. In pursuit of this goal, fundamental topics that are relevant to this study have been gathered in this chapter and the following parts are concerned with brief overviews into relevant literature and explaining topics that are most closely related to the scheme of this thesis.

## 1.2 Thermodynamics of the Solid Surfaces

The objective of this section is to describe the physiochemical foundation of the interfaces which essentially helps to understand the phenomena like dewetting. Thermodynamics plays a central role in discussion of the main subjects involving energetics of the surfaces and the interfaces. Gibbs free energy, thermodynamic equilibrium, and wetability are the most important topics to be discussed in the following parts.

### 1.2.1 Surface Free Energy and Surface Tension

With any interface in general or any surface in specific (any free surface can be regarded as a coexistence of a semi-infinite solid with its vapor) there is an energy associated which corresponds to the amount of work required to create a unit area of the surface. From macroscopic point of view, creation of any interface (or free surface) occurs with external work disturbing the bulk equilibrium of two (infinite) phases and bringing them together at the interface to a new thermodynamic equilibrium [4]. In microscopic perspective however, this corresponds to breaking the chemical bonds of the atoms or molecules inside the bulk of each phase and forcing them to bond to the opposite phase at the interface. Thus, the *surface free energy* per unit of area is the total energy

added to the *Gibbs free energy* of the system as a result of creation of the interface as expressed by:

$$G = G_1 V_1 + G_2 V_2 + \gamma_{12} A_{12} \tag{1.1}$$

where G, $G_1$, and $G_2$ are the Gibbs free energy of the overall system, unit volume of phase 1, and unit volume of phase 2, respectively, and $\gamma_{12}$ and $A_{12}$ are the Gibbs free energy per unit area and the area associated with the interface separating two phases. The Gibbs free energy per unit area of a surface is consist of contributions from different factors, such that:

$$\gamma = \epsilon - T\eta + p\upsilon \tag{1.2}$$

where $\epsilon$ is the surface energy per unit area, $\eta$ is the surface entropy per unit area, $\upsilon$ is the surface volume per unit area, and T and p are absolute temperature and the pressure. The final term, $\upsilon$ is introduced to the Gibbs free energy of the surface as result of variations in atom density in topmost layers of the surface such as in cases that the bulk and surface crystal structures are different. This term, however, is very small and when neglected, reduces the above equation to the *Helmholtz free energy*. Gibbs free energy of the surface also accounts for the adsorption in the surface by adding the term $\mu_i \Gamma_i$ to the above equation in which $\mu_i$ is the *chemical potential* of the $i$th adsorbate species and $\Gamma_i$ is the surface density of the them.

As it pointed out, the Gibbs free energy of a surface equals the amount of work done to *form* a new surface. There is also a similar concept that is defined as the amount of work done to *stretch* or extend a surface in order to create new surface areas and is called *surface tension*. Surface tension and Gibbs free energy of the surface are equal for fluid systems because the work done to form a new interface is equal to the work done to expand the interface by the same area. But this is not the case in solids because the two processes are not equivalent unless the formation of interface through stretching is deemed to not deform the surface structure. This can be true when one assumes the temperature in which the work is done, is sufficiently high to allow for bulk and surface diffusion to rectify the distortions resulted from the work. Thus, allowing to use Gibbs free energy and surface tension interchangeably for solids as well.

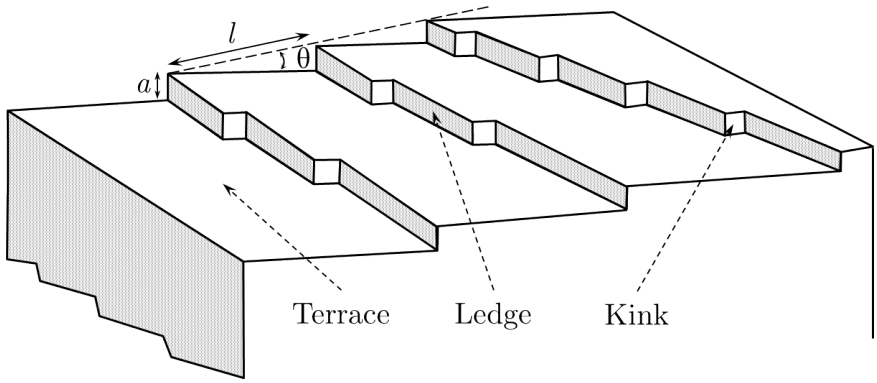


Figure 1.1: Terraces, ledges, and kinks as appear on the surface of cleaved crystalline solid (Adapted from [4]).

### 1.2.2 Equilibrium Shape of a Surface

In crystalline solids, atomic coordination is a function of crystal structure and hence the interfacial free energies depend on the orientation of crystallographic planes composing the interface. To fully identify the dependence of surface free energy on the crystallographic orientations, a polar diagram named "$\gamma$-plot" is conventionally used with the radial coordination proportional to $\gamma$ value of each plane [5]. In ideal situation, any arbitrary cleavage into the crystal, would create an interface exposing a finite number of planes with lowest possible indices (most densely packed, most stable) total energies of whose match the work of truncation. Such interface would appear as a series of terraces of low-index planes with a step (or ledge) density being characteristic of angular deviation of truncation from planes' normal. Figure 1.1 depicts a part of such interface. Now, the interface $\gamma_\theta$ can be expressed as sum of energies of low-index planes (per unit area), $\gamma_0$, the ledge energy (per unit length), $\beta$, and a term for kinks in more complex cases. Thus, for a surface with no ledges, the $\gamma_\theta$ is given by:

$$\gamma_\theta = \gamma_0 \cos|\theta| + \frac{\beta}{l} = \gamma_0 \cos|\theta| + \frac{\beta}{a}\sin|\theta|. \tag{1.3}$$

$\theta$ is expressed in absolute values due to the symmetry in crystallinity which also implies that creating a new surface always costs energy. Mathematically the $\gamma_\theta$ function will reach to minima on the $\theta = 0, \pi/4, \pi/2, ...$ and also local minima where ever the $\theta$ corresponds to planes with rational Miller indices, forming "cusps" in the $\gamma$-plot. Mapping out the $\gamma_\theta$ for all $\theta$ values yields the $\gamma$-plot that schematically looks like the

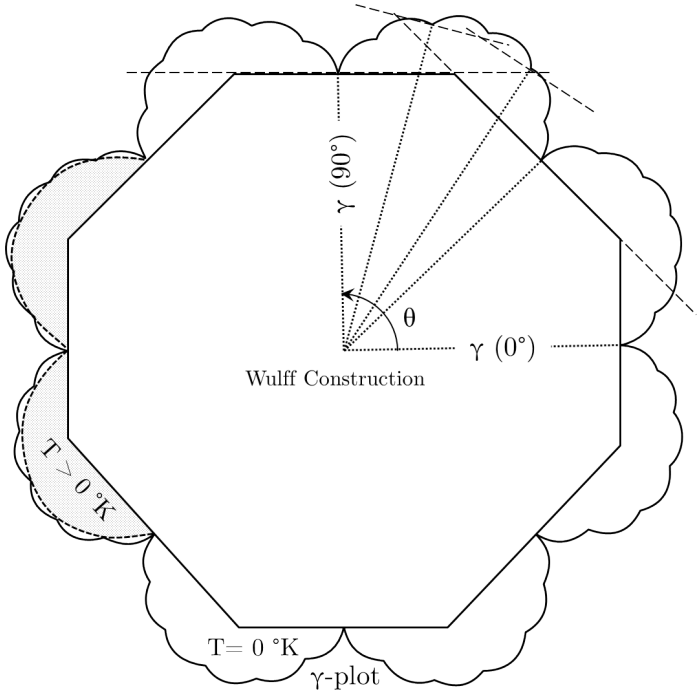


Figure 1.2: $\gamma$-plot for a solid interface in absolute zero and elevated temperatures with the corresponding Wulff octagonal construction contained inside (Adapted from [4]).

one depicted in Figure 1.2 dubbed as a 'raspberry' figure [4].

With increasing the temperature from absolute zero, the shape of the $\gamma$-plot would smooth out with removal cusps of higher index planes. At finite temperatures the term associated with the entropy in equation 1.2 becomes more pronounced as local fluctuation in position of adatoms increases. This also leads to inhibition of high-index planes since adatoms now have enough kinetic energy to diffuse and sit in front of those kinks that provide higher number of bond (deeper potential trap) namely on low-index planes. Eventually, higher rate of expansion will cause low-index planes to outgrow the high-index ones and decrease the density of steps in the final shape of surface after the thermal transition.

However, at specific temperature, the equilibrium shape of a surface and accordingly the equilibrium shape of the solid crystal will be determined with the anisotropy in the surface tension at that temperature. Wulff proposed a theorem that predicts the equilibrium shape of a crystal when the $\gamma$-plot is completely sketched for all values of $\theta$ [6]. The result of the Wulff theorem is Wulff construction obtained by drawing

perpendicular planes to $\gamma$ vectors at the intersection points of the corresponding cusps. The resulting convex figure that is enveloped with the (deepest cusp) planes determines the equilibrium shape of the crystal. It is noteworthy that driving force for obtaining such faceted shape, is the desire of the system (the crystalline particle in this case) to minimize its internal energy by means of reducing surface free energy in the equilibrium configuration. A two dimensional Wullf construction is illustrated in Figure 1.2.

### 1.2.3 Wetting and Dewetting Phenomena

#### 1.2.3.1 Spreading and Contact Angle

A direct consequence of the surface tension is the affinity (or aversion) of different materials with different surface tensions at their interface. One way to investigate such affinity is through examining the wettability of a liquid phase on a solid substrate where a liquid droplet placed atop of a solid surface and is in thermal equilibrium with its saturated vapor covering the surrounding atmosphere on substrate. In thermodynamical steady state, two possible equilibrium regimes may appear: partial wetting, or complete wetting. Wettability is then defined as the tendency of the liquid phase to cover the substrates surface. In the former case, the force balance cause formation of a triple junction between solid, liquid, and gas phases through which the liquid droplet attains a hemispherical shape with a contact angle characteristic to the wattability of liquid on solid. In the latter case, the total affinity of solid- liquid causes the droplet to completely spread on the substrate and reach zero contact angle [7].

*Thomas Young* (1773-1829) proposed the equation that governs the thermodynamic equilibrium in the triple junction when observed in macroscopic scales:

$$\gamma_{SV} - \gamma_{SL} - \gamma_{LV} \cos\theta_{eq} = 0 \tag{1.4}$$

where the $\gamma_{SV}, \gamma_{SL}, and \gamma_{LV}$ are the interface free energy of solid-vapor, solid-liquid, and liquid-vapor per unit area and $\theta_{eq}$ is the contact angle. The macroscopic constraint on the equation is necessary to avoid anomalies caused by pinning of the triple line on defects of the solid surface in atomic scales which leads to a hysteresis of the contact angles and can obscure experimental determination of $\theta$. It is convenient to assume the substrate surface is smooth and chemically homogeneous. Figure 1.3 schematically shows the distinct equilibrium wetting phenomena of a liquid droplet deposited on a

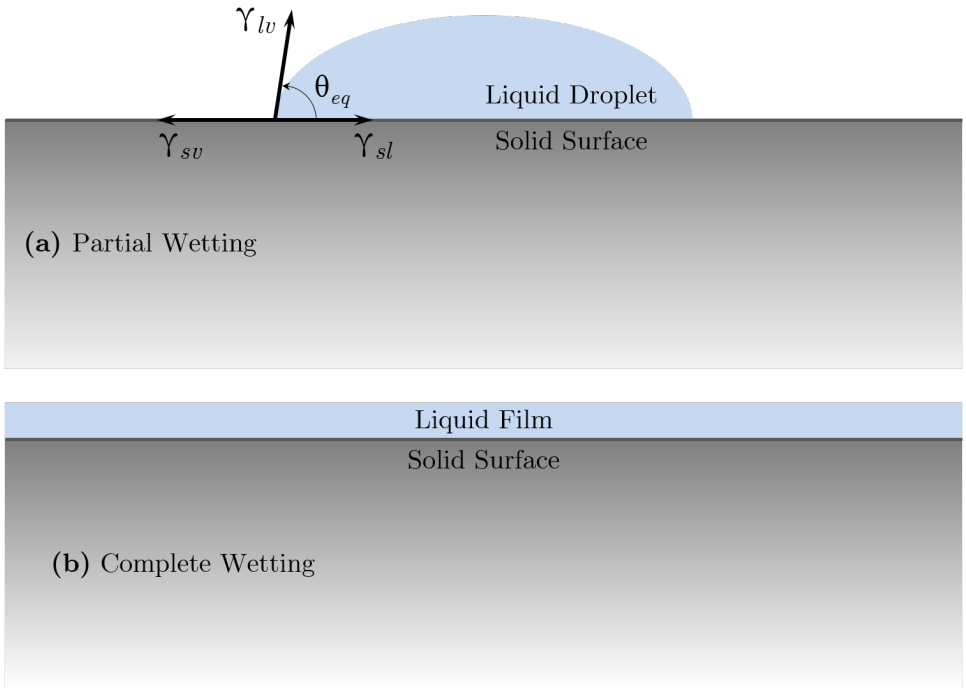


Figure 1.3: Equilibrium shape of a liquid droplet on a solid flat substrate: (a) Partial wetting, and (b) Complete wetting (Adapted from [8]).

solid substrate [8].

Complete wetting in Figure 1.3 (b) corresponds to the situation where $\theta_e = 0$ and a liquid thin film covers the whole solid surface. It can also be inferred that $\gamma_{SV}$ can never be larger than $\gamma_{SL} + \gamma_{LV}$ in thermodynamic equilibrium. More so generally, is that neither $\gamma_{SL}$ nor $\gamma_{SV}$ can be larger than the sum of two other surface energies. Any deviation from equilibrium towards $\gamma_{SL} + \gamma_{LV} < \gamma_{SV}$ or $\gamma_{SV} + \gamma_{LV} < \gamma_{SL}$ would cause the free energy of a solid-vapor interface to be lowered by intercalation of a liquid film of macroscopic thickness (via spontaneous vapor condensation on substrate, for instance) so that the true $\gamma_{SV}$ is again identical to $\gamma_{SL} + \gamma_{LV}$.

Partial wetting happens when the $\gamma_{SV} < \gamma_{SL} + \gamma_{LV}$ and a liquid droplet with finite contact angle minimize the free energy of the system. In order to differentiate between partial and complete wetting states and to predict the dynamical endpoint of the system (triple junction point), *equilibrium spreading coefficient* $S_{eq} \leqslant 0$ is defined by

*Young-Dupré* equation as:

$$S_{eq} \equiv \gamma_{SV} - (\gamma_{SL} + \gamma_{LV}) = \gamma_{LV}(\cos\theta_{eq} - 1) \tag{1.5}$$

where $S_{eq} < 0$ corresponds to partial wetting state and $S_{eq} = 0$ corresponds to complete wetting state. In other words the Young equation set the thermodynamic limits for wettability while the spreading coefficient predicts the dynamics for reaching thermodynamic equilibrium [8].

A partially wet solid-liquid interface forces a sufficiently thin continuous film to break up and bead off the surface of solid substrate. The rupture and disintegration of film into islands and droplets occurs when the kinetic conditions are met and last until the interface energy is minimized to achieve thermodynamic equilibrium. This phenomenon is known as *dewetting* and can be regarded as the opposite process of spreading [9].

To identify the dewetting behavior of a liquid film on a solid substrate, two major parameters should be defined: (i) the surface chemistry of solid substrate, and (ii) the thickness of liquid film. Solid surfaces are generally divided into *high-energy* and *low-energy*. High-energy surfaces are those that require high amount of energy (work) inputs to be created and vise versa. The amount of energy depends on the bulk nature of solid, that is, the type of chemical bonds. Thus, ionic, covalent, and metallic solids fall into the category of "hard solids" that have high-energy surfaces for which the chemical binding energy is of the order of 1 eV and on which nearly any liquid spreads. The surface tension of this category is given by [7]:

$$\gamma_{SV} \approx \frac{E_{binding}}{a^2} \sim 500 - 5,000\ mN/m \tag{1.6}$$

where, $a^2$ is the surface area of a single exposed molecule in the topmost layer of solid. "Soft solids" are, on the other hand, made of large organic molecules held together by weak physical bonds such as van der Waals and hydrogen bonds including molecular crystals and plastics. The chemical binding energy of such substances is of the order of $kT$, which are generally hardly wettable. The surface tension of this category is given by [7]:

$$\gamma_{SV} \approx \frac{kT}{a^2} \sim 10 - 50\ mN/m \tag{1.7}$$

Most organic liquids would achieve complete wetting on high-energy surfaces as a result of no effective interactions in the interface. But, other liquids with high surface tension may dewet on high-energy surfaces as a result of high energy cost of interfacial interactions. To predict the state wettability, the sign of the spreading parameter S, in addition to the surface energy $\gamma_{SV}$ is required. To do so, the relationship between S and the *electric polarisabilites* $(\alpha_S, \alpha_L)$ of solid and liquid should be established. Bringing together two semi-infinite media (solid and liquid for instance) and merging them cause the energy gain of van der Waals $V_{SL}$ (per unit area) onto initial $\gamma_{SV} + \gamma_{LV}$ which is related to the polarizability as of the medium via the relation: $V_{SL} = \kappa\alpha_S\alpha_L$; where $\kappa$ is a constant. Overall, one will reach the following equation [7]:

$$\gamma_{SL} = \gamma_{LV} + \gamma_{SV} - V_{SL} \tag{1.8}$$

This approach can also be used for a pair of similar semi-infinite liquid or solid phases and determine $\gamma_{SV}$ and $\gamma_{LV}$, individually and the results would be as following:

$$2\gamma_{SV} - V_{SS} = 0 \tag{1.9}$$

$$2\gamma_{LV} - V_{LL} = 0 \tag{1.10}$$

Combining equations 1.5 for non-equilibrium state and 1.8 - 1.10 will render spreading factor S as following [7]:

$$S = \gamma_{SV} - (\gamma_{SL} + \gamma_{LV}) = V_{SL} - V_{LL} = \kappa(\alpha_S - \alpha_L)\alpha_L \tag{1.11}$$

With $\gamma_{SV}$ dropping out of the equation 1.11, one can conclude that a positive spreading factor will yield to total wettability and that corresponds to a situation where: $\alpha_S > \alpha_L$; meaning that *a liquid less polarizable than a solid will completely spread on the interface.*

An experimental criterion of wettability is also available from *Zisman*'s studies. In his theory any solid substrate has a critical surface tension $\gamma_C$ such that [7]:

$$\begin{cases} \gamma > \gamma_C \Rightarrow \textit{partial wetting}; \\ \gamma < \gamma_C \Rightarrow \textit{total wetting} \end{cases} \tag{1.12}$$

where $\gamma$ is the surface tension of liquid. Zisman studied the critical surface tension $\gamma_C$ by investigating the wetting behavior of a series of organic liquids and plotting $\cos\theta_{eq}$ as a function of $\gamma$. He found out that for non-polar liquids, the value of $\gamma_C$ is

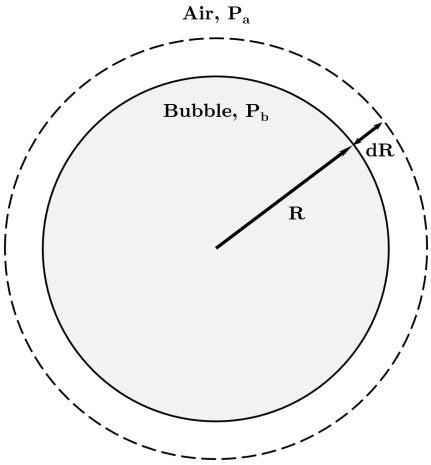


Figure 1.4: A bubble in the air reaching equilibrium state under work $\delta W$ (Adapted from [7]).

a property of the solid upon which the contact angle of liquid droplet becomes zero independent from the type of liquid used. This result correspond to a state in which $\alpha_S = \alpha_L$.

#### 1.2.3.2 Laplace Pressure and Capillary Length

The overpressure existing in the interior of drops and bubbles cause their surface to bend inwards and create what the final shape of the bubble or drop is. As a consequence of this pressure, drops and bubble adopt spherical shape in equilibrium, smaller drops disappear in favor of larger ones (Ostwald ripening), and capillary adhesion forms between plates and fibers [7, 10].

In the example of bubble in air as illustrated in Figure 1.4, in the mechanical equilibrium state, any work done to displace interface must equal to zero; that is:

$$\delta W = -p_b dV_b - p_a dV_a + \gamma_i dA = 0 \tag{1.13}$$

where, $dV_b = -dV_a = 4\pi R^2$, and $dA = 8\pi R dR$, and the *Laplace pressure* can be calculated from 1.13 as:

$$\Delta P = p_b - p_a = \frac{2\gamma_i}{R} \tag{1.14}$$

and the general form of *Laplace theorem* can be stated as:

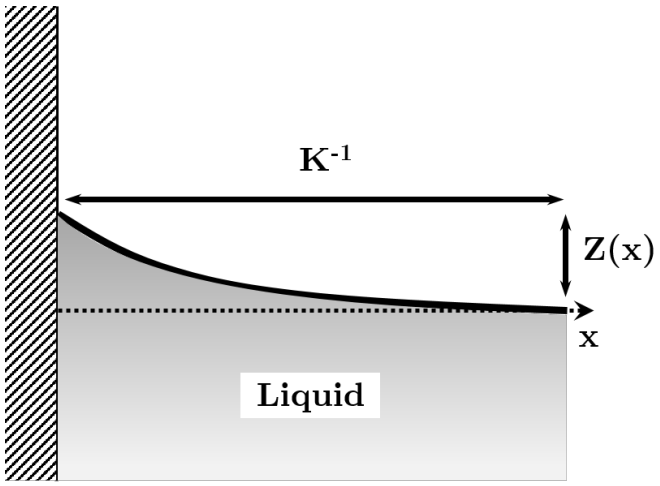


Figure 1.5: Perturbation decaying in a characteristic distance relative to capillary length of liquid from an object inserted in liquid (Adapted from [7]).

*The hydrostatic pressure difference $\Delta p$ between two fluids is equal to product of the interface tension $\gamma$ and the curvature of the interface $C = \frac{1}{R} + \frac{1}{R'}$.*

Laplace pressure when compared to the hydrostatic pressure of a liquid of density $\rho$ at a certain depth of the liquid $\kappa^{-1}$, shows at what point the force of gravity g becomes negligible. At sizes $r < \kappa^{-1}$, the eventual equilibrium shape of a droplet will dominantly be determined by capillary effects. Beyond this particular length $\kappa^{-1}$ however, the gravitational acceleration g($\simeq 9.8\ m/s^2$) becomes important in shaping the droplet. $\kappa^{-1} = \sqrt{\gamma/\rho g}$ is called the *capillary length* of the liquid [7].

Capillary length is a characteristic of any liquid and it also determines the distance at which perturbation from an object on the surface of liquid decays which essentially means that perturbation amplitude decays exponentially in a distance relative to characteristic constant of capillary length $\kappa^{-1}$. The dispersion equation of the perturbation can be derived when equating the pressures obtained from Laplace equation and hydrostatic law for the curved region in the vicinity of the object [7]:

$$\begin{cases} p^* = p_{atm} - \gamma \dfrac{\partial^2 z}{\partial x^2} \\ p^* = p_{atm} - \rho g z \end{cases} \quad \Rightarrow \gamma \frac{\partial^2 z}{\partial x^2} = \rho g z \tag{1.15}$$

and solving the equation 1.15 under (z = 0 @ x$\rightarrow \infty$) will yield:

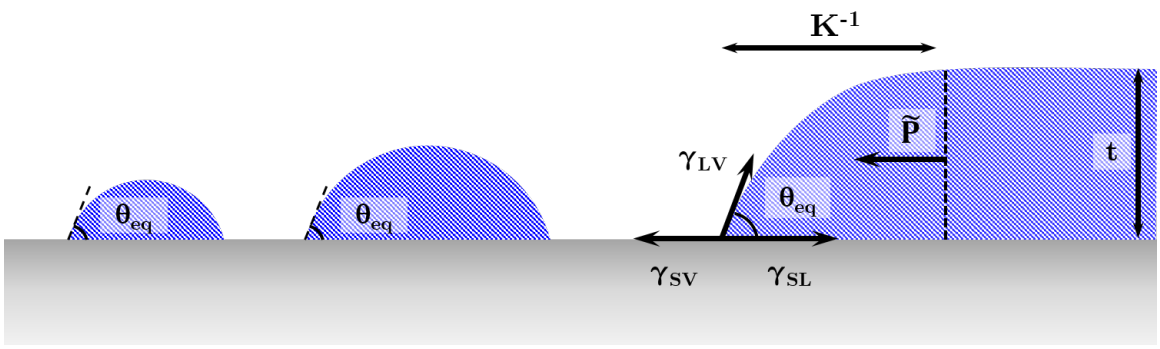


Figure 1.6: Shapes of different size drops atop of a solid substrate (Adapted from [7]).

$$Z(x) = Z_0 \; exp \; (-\kappa x) \tag{1.16}$$

Capillary length may also be utilized to determine the thickness of drops atop of solid substrates. To do so, drops of different sizes are categorized into two groups: one, drops of radii smaller than $\kappa^{-1}$ for which the capillary forces are dominant and second, drops of radii larger than $\kappa^{-1}$ where the gravitational effects dominate. For the former group, the Laplace law imposes a constant curvature throughout the liquid/vapor interface and a spherical cap shape at contact with substrate at an angle equal to $\theta_{eq}$. For the latter group, on the other hand, dominant gravitational force tends to flatten the liquid/vapor interface and the equilibrium shape is similar to that of a pancake with thickness $t$ [7, 10].

The thickness of the liquid *pancake* can be calculated by equating the mean hydrostatic pressure and the surface forces at equilibrium [7]:

$$\begin{cases} \tilde{p}_{hyrdostatic} = \int_0^t \rho g(t-\tilde{z})d\tilde{z} = \frac{1}{2}\rho g t^2 \\ S = \gamma_{SV} - (\gamma_{LV} + \gamma_{SL}) \\ Young : \gamma_{SV} - (\gamma_{LV}\cos\theta_{eq} + \gamma_{SL}) = 0 \end{cases} \Rightarrow \gamma(1-\cos\theta_{eq}) = \frac{1}{2}\rho g t^2 \tag{1.17}$$

Rearranging the equation 1.17, when $\sqrt{\gamma/\rho g} = \kappa^{-1}$, yields to:

$$t = 2\kappa^{-1}\sin(\frac{\theta_{eq}}{2}) \tag{1.18}$$

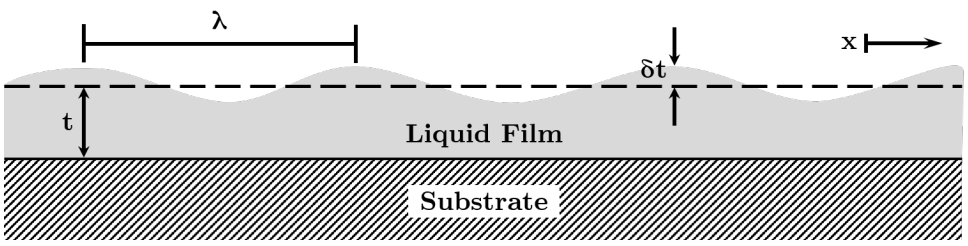


Figure 1.7: A small disturbance in the surface of a liquid film causing regular ripples in x direction (Adapted from [7]).

Capillary length is also useful in studying the behavior of a perturbation disturbing the liquid/vapor interface of a film with flow of ripples. Such disturbances tend to generally attenuate as result of gravity force damping the surface waves in denser medium, and tendency to lower surface tension by straightening the rippled surface. Assuming a stable film on a solid surface and if the thickness of the film is much smaller than the wavelength of the ripples ($t < \lambda$) and the viscous force prevail over inertia, then it can be expected through reasonable approximations that in a certain period of time the ripples will die off [7, 10].

According to Figure 1.7 the hydrostatic and Laplace pressures are higher underneath a crest than underneath a trough. This will set a net flow from crests towards the troughs to level the liquid surface. However, one the two mechanisms (gravity and capillarity) will be dominant over the other. The hydrostatic pressure difference between a crest (or a trough) and the average height of the film is $\rho g \delta t$. The Laplace pressure for a weakly curved surface *i.e.* $|\frac{dt}{dx}| \ll 1$, is $C \approx -\frac{d^2t}{dx^2}$. The difference in curvature between a crest/trough and the median line is about $\frac{\delta t}{\lambda^2}$ and the ratio of the hydrostatic pressure to the Laplace pressure is $(\lambda\kappa)^2$. So for the ripples with short wavelength ($\lambda < \kappa^{-1}$), the surface tension of the liquid is dominant, making so-called *capillary waves* [7].

However, if a stable film is replaced with an unstable film on the substrate, that is $\gamma_{SV} < \gamma_{SL}$, then a capillary wave through the film surface will be amplified instead of attenuating and cause spontaneous ruptures in the film.

#### 1.2.3.3 Dewetting of Liquid Films

If a non-wetting film is deposited on top of a substrate ($S < 0$) it has to become thin enough to be destabilized by interfacial forces and eventually break up into stable

phases through dewetting. This critical thickness is the thickness of liquid pancake discussed in previous section [7, 8].

It is common to ascribe an *effective interface potential* V(t) to a film of liquid deposited on a surface which is a function of thickness t. V(t) shows the energy per area dependence of a film to thickness. The boundary conditions impose that when (t $\rightarrow \infty$), total energy contribution from surfaces amount to independent solid/liquid interface and liquid/vapor tensions $\gamma_{SV} + \gamma_{LV}$, hence V($\infty$) = 0. And when film becomes very thin (t $\rightarrow$ 0) the surface tension of bare solid $\gamma_{SV}$ to be solely retrieved, hence V(0) = S = $\gamma_{SV} - \gamma_{SL} - \gamma_{LV}$ [7].

The effective interface potential is an outcome of solid/liquid and liquid/vapor molecular interactions. If the product of such interactions results, for instance, in strong adhesion between solid and liquid phases, then the tendency of the system would be to increase the distance between solid/liquid and liquid/vapor interfaces to lower the free energy and a net repulsive force per unit area so called *disjoining pressure* $\Pi(t)$ forms between the interfaces. $\Pi(t)$ is equivalent to $-\frac{dV(t)}{dt}$; *i.e.* $\Pi(t)$ the tangent line to V(t) vs. t curve. Since, the volume is generally conserved during the process of spreading, for S > 0, the static thickness will be governed by minimizing the free surface energy which leads to the condition [7]:

$$\frac{V(t) - V(0)}{t} = \frac{dV(t)}{dt} \tag{1.19}$$

so that the static thickness can be determined through tangent rule in V(t) plot. It can be realized from the V(t) plot that a liquid film is stable only if the curvature of the V(t) is positive ($\ddot{\text{V}}$(t) > 0). When the curvature turns negative, any film of thickness $t$ will split up into two separate films of thicknesses $t_1$ and $t_2$, as illustrated in Figure 1.8, occupying fractions $X_1$ and $X_2$ of surface ($X_1 + X_2 = 1$) and the sum of energies becomes $X_1V(t_1) + X_2V(t_2)$ which is lower than the initial V(t) [7].

One special scenario is when the dry solid (t = 0) is exposed together with a liquid film of thickness $t_c$ through dewetting. Thus, three different types of wetting situations can be devised: (i) *Total wetting*; where S > 0 and the thickness dependence of function V(t) looks like that of Figure 1.9.a. By drawing the simple tangent a threshold thickness $t_c$ could be realized beyond which all the films are stable and can coexist with dry solid. (ii) *Partial wetting*; where S < 0 and the thickness dependence of function V(t) looks like that of Figure 1.9.b. any simple tangent to the V(t) curve shows that the dry solid can only coexist with a drop of t $\rightarrow \infty$. (iii) *Pseudo-partial*

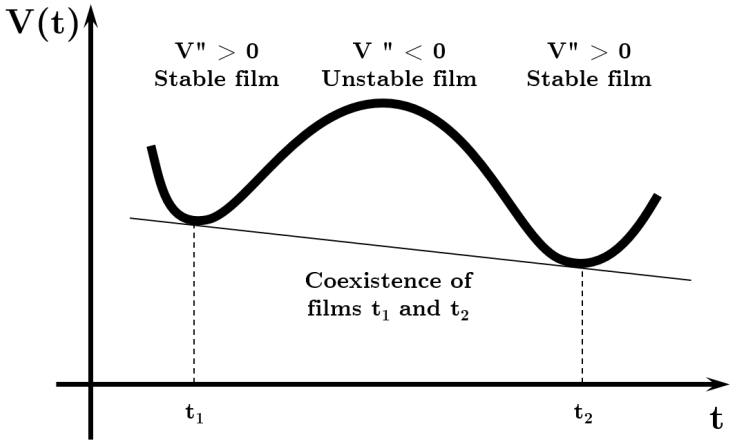


Figure 1.8: A generic plot of effective interface potential V(t) and a common tangent line to two local minima indicating the stable films with thicknesses $t_1$ and $t_2$ coexisting on a substrate surface (Adapted from [7]).

*wetting*; where a common tangent line to the curve at point m and at a point at infinity, implies the coexistence of a film of thickness $t_m$ and a macroscopic drop (t $\rightarrow \infty$) [7].

To realize the critical thickness $t_c$ of a liquid deposit on a non-wettable solid surface, the free energy of the liquid film should be defined as a function of its thickness. This function for macroscopic films (where gravity plays a dominant role) is defined as:

$$G(t) = \gamma_{SL} + \gamma_{LV} + \frac{1}{2}\rho g t^2 \tag{1.20}$$

where; $\frac{1}{2}\rho g t^2$ term is the mean gravitational energy of the film. This function does not act smoothly when t $\rightarrow$ 0, because at the microscopic levels van der Waals forces are dominant and add more terms to the G(t) function. However, Maxwell's construction of double tangent onto the G(t) function reveals an equilibrium between the dry solid and a film of thickness $t_c$, corresponding to the liquid pancake thickness. Figure 1.10 describes this situation where a metastable film of thickness t $< t_c$ ($\ddot{\text{G}}$(t) $> 0$) breaks up into two phases, dry solid and a stable film of thickness $t_c$, and the total energy is minimized [7].

The process of drying (dewetting) in this case takes place through nucleation and growth of a dry zone. The classical thermodynamic equations of nucleation and growth governs the formation of the dry zones so, one would expect that any nucleated dry area should have reach a critical size in order to pass the energy barrier to further

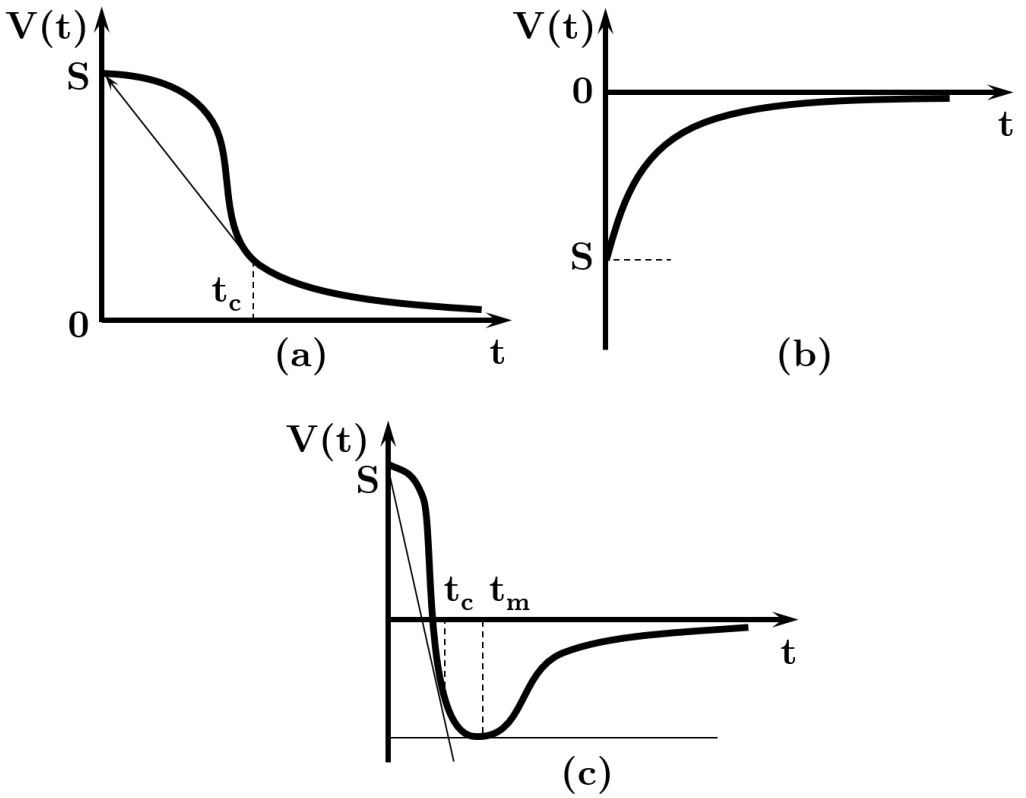


Figure 1.9: Three different types of wetting: (a) total wetting, (b) partial wetting, and (c) pseudo-partial wetting (Adapted from [7]).

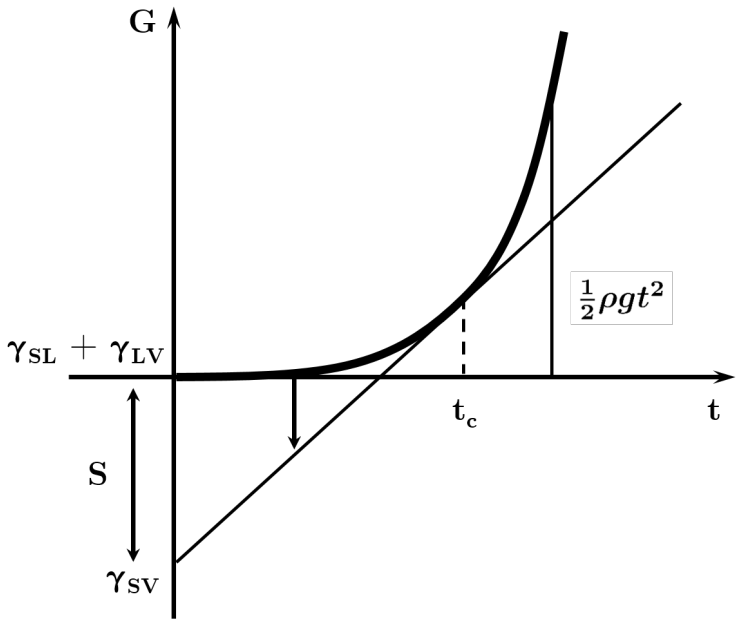


Figure 1.10: Free energy G(t) as a function of the thickness t of a liquid film deposited on a non-wettable substrate. Maxwell's double tangent indicates the coexistence between the dry solid (t = 0) and a liquid pancake of t = $t_c$ (Adapted from [7]).

grow to a stable dry region [7].

For the case of thin films on the other hand, the G(t) function should be modified by adding the contributions of van der Waals forces in terms of effective interface potential V(t), thus rendering the modified form of equation 1.20 as [7]:

$$G(t) = \gamma_{SL} + \gamma_{LV} + V(t) + \frac{1}{2}\rho g t^2 \tag{1.21}$$

where V(t) is $\frac{A}{12\pi t^2}$, and A is the renowned *Hamaker* constant and defined as the amount of energy required to cleave through an interface and create two fresh surfaces. The value of A is an indication of the amplitude (strength) of the molecular interactions at the interface and its sign affects the slope of tangent line to the V(t) curve and thus, influence the wetting behavior of two phases [7].

A more general G(t) function is illustrated in Figure 1.10. In the microscopic film scales the curvature of G(t) is negative and the film is unstable. In this region, any perturbation, in form of capillary waves for instance, gets amplified and the film spontaneously breaks up into multiple droplets. This process of spontaneous rupture

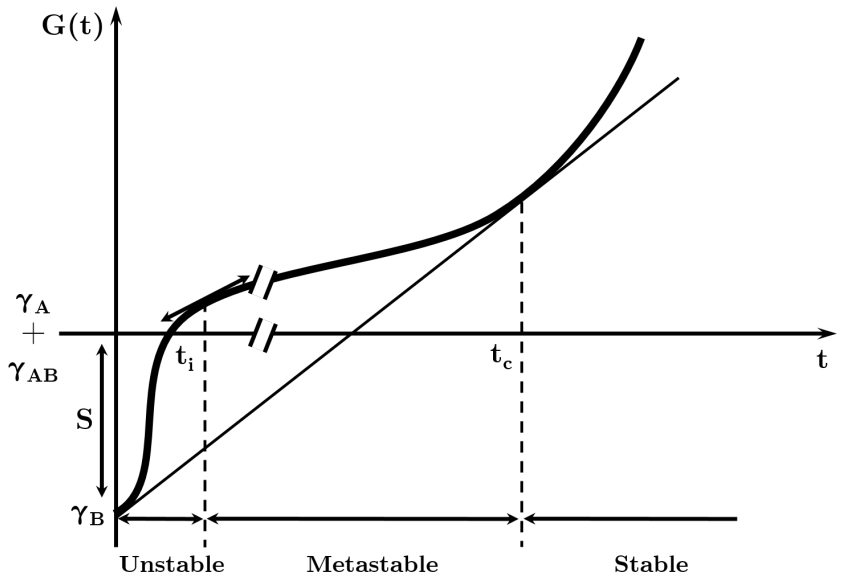


Figure 1.11: A more general curve of G(t) function covering thicknesses from 0 to $\infty$. For $t < t_c$ and based on the curvature of G(t), two distinct dewetting mechanisms can be realized: if $\ddot{G}(t) > 0$, the film is metastable and nucleation and growth of dry zones is the main dewetting process, and if $\ddot{G}(t) < 0$, the film is unstable and spontaneous dewetting occurs through spinodal decomposition (Adapted from [7]).

is called *spinodal decomposition* [7].

#### 1.2.3.4 Solid State Dewetting

The idea of wettability of thin films can be extended to also include solid thin films. Since most of technologically important solid thin films are grown through condensation of a vapor or liquid phase on a solid substrate, it is helpful to imagine such films as supercooled liquids with much lower dynamic energy. Solid films deposited on non-wetting substrates are expected to dewet if the energy to carry the process is provided. From this perspective, all causes that induce liquid film dewetting also apply to solid films and that is, capillary effects.

For liquid state dewetting, the energy barrier amounts to the heat required to melt the solid film plus enough thermal energy to induce surface perturbation to trigger surface break up. However, it is also possible for films to undergo a process of solid-state dewetting with a lower energy barrier below their melting point. Solid state dewetting is mainly mediated through atomic diffusion rather than balk transportation of mass

as liquid flow [11]. As a result, the rate of dewetting process is highly temperature dependent.

Theoretically, it is known that a series of *fingering* (where some parts shrink to extremely narrow neckings like fingers) and subsequent *Rayleigh-Plateau* instabilities bring about homogeneous dewetting of the solid films. However, from kinetics point of view such processes are too slow to effectively transform metastable films to stable islands and particles. In reality, most thin films are formed under conditions that cause residual stress and structural defects. These are energetically more favorable sites for holes and cracks to form and subsequently lead to heterogeneous rupture of thin films. Grain boundaries in polycrystalline films and the locally strained parts are among these sites [12].

Capillary effects due to surface instabilities can drive solid thin films to unstable state in which the chemical potential of surface varies with the curvature of undulation. The *Gibbs-Thomson* equation for a perturbed surface is given by:

$$\mu = \mu^{\circ} + \kappa\gamma\Omega \tag{1.22}$$

where $\mu$ is the chemical potential of perturbed surface, $\mu^{\circ}$ is the chemical potential of the flat surface, $\kappa$ is the local curvature of the surface, $\gamma$ is the surface tension, and $\Omega$ is the atomic volume. The curvature added term means that any sufficiently large perturbation can cause mass transportation in the film and evolution of the surface. However, it is argued that flat surfaces with isotropic surface tensions are stable in the face of any perturbation whose amplitude dose not exceed the thickness of the film and therefore, a mechanism of hole formation in the film is necessary to initiate solid dewetting [13, 14]. The holes reach from surface of the film to surface of the substrate, creating a cite where the force balance of tensions is far from equilibrium and allowing surface perturbation to amplify and split the non-wetting film.

As shown by Mullins, in polycrystalline films, grain boundaries are ideal place for hole formation [15]. The force balance at top of a mutual grain boundary leads to the shape evolution shown in a simple case as Figure 1.12 in which a *groove* can form and gradually reach the substrate and for which we have:

$$\begin{cases} \phi = \arcsin(\dfrac{2\gamma_f}{\gamma_{gb}}) \\ \delta = R(\dfrac{2 - 3\cos\phi + \cos^3\phi}{3\sin^3\phi}) \end{cases} \tag{1.23}$$

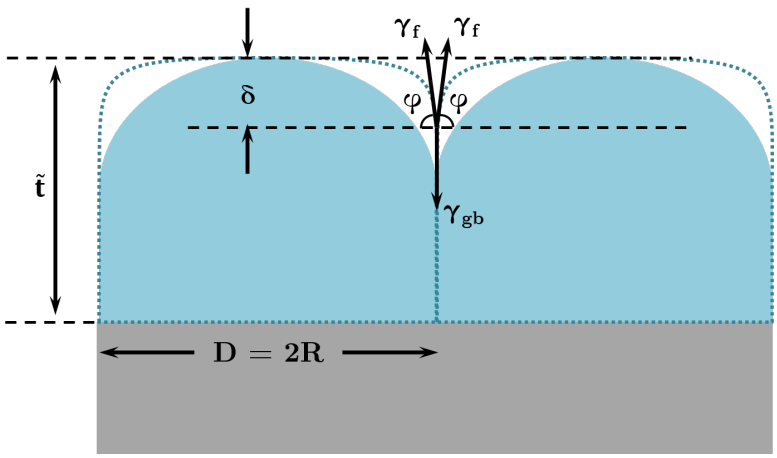


Figure 1.12: Formation and development of a groove in a grain boundary in polycrystalline films (Adapted from [14]).

where, $\delta$ is the depth of a groove that when becomes greater than thickness t, it can result in formation of a hole. Therefore, for any grain with R > $R_c$, a groove can advance to create a hole:

$$R_c = \frac{3\sin^3\phi}{(2 - 3\cos\phi + \cos^3\phi)t} \tag{1.24}$$

Once a hole is formed, the capillary forces further expand it by *retracting* its edges. Retracting occurs to reduce the high curvature of the edges. During edge retraction, material transports from the hole edge and wall over to the flat surface of the film surrounding the hole, but since the curvature of the flat film surface is always less than the edge, a net flux of film material from hole edge over to the hole rim will continue leading to hole growth [14].

There exist two mechanisms through which the mass transport can occur from hole edges: bulk *self-diffusion* and *evaporation-condensation*. Amongst the two, self-diffusion is believed to be the dominant process, considering the evidence from morphology of the film in consequent stages of the dewetting process. The driving force for the diffusion mechanism is the gradient in local surface curvature and the driving force for the evaporation-condensation is the gradient in local vapor pressure. Combination of the paths of each of the mechanisms results in the flux and the evolution of hole rim that previously described [13].

The process of solid state dewetting continues further by detachment of the thickened

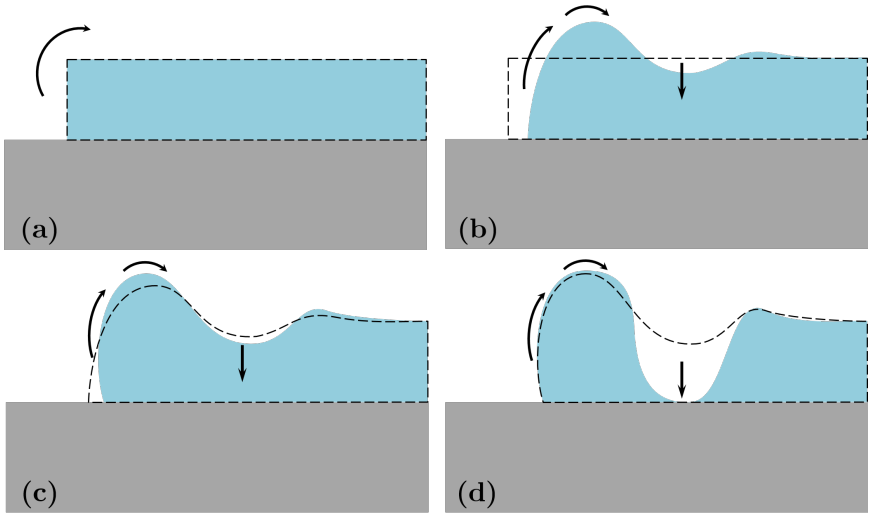


Figure 1.13: Formation and development of rims and valleys and the pinch-off process. Arrows show the paths of mass transport through self-diffusion and evaporation-condensation processes (Adapted from [14]).

rims from rest of the surrounding film material through a *mass shedding process*. Studies by Srolovitz & Safran on 2D models of hole edges revealed that the formation of the thicker rims is associated with an oscillation in the film's surface ahead of the rim, which gradually develops a valley immediately after the rim [16]. The valley then deepens until it touches the substrate surface and the rim is completely *pinched off* from the rest of the film. Figure 1.13 schematically illustrates the edge retraction of a hole, formation of a rim and valley, and final pinch-off the rim ring.

Mass shedding through pinch-off process proceed until all of the film has disintegrated into rings of formerly existed as rims in the edge of holes. The rings themselves are not the most stable shapes of dewetted solid films and they should break up further into more stable bodies as the dewetting process goes on. Sometimes, the rims of adjacent holes can meet and form narrow finger-like strands (fingering instability). These strands (fingers) along with the rings undergo subsequent Rayleigh-Plateau instability because of their cylindrical nature and eventually, break up into arrays of more equiaxed agglomerates that reduce total energy of the system to minimum [14].

## 1.3 Magnesium Aluminate ($MgAl_2O_4$) Spinel

### 1.3.1 Bulk Properties

Spinel is a crystallographic structure of a large family of minerals, of which *magnesium aluminate* is the best known and often interchangeably referred to as *spinel*, itself. This group of minerals are family of ternary oxides with chemical formula of $A^{II}B_2^{III}O_4(\equiv A^{2+}:2B^{3+}:4O^{2-})$; where A and B are metal cations of valence 2 and 3, respectively, and O is oxygen anion [17, 18].

A and B, based on their chemical bonds, coordinate in different sites of the crystal structure. Accordingly, in *normal* spinels, divalent A species occupy one-eighth of the relatively smaller tetrahedral sites and trivalent B species occupy half of the larger octahedral sites such as in $MgAl_2O_4$. Normal spinels are usually classified as cubic close-packed oxides with two tetrahedral and one octahedral sites per formula unit. On the other hand, *inverse* spinels have different cation coordination, where A and half of the B species occupy all of octahedral sites and the other half of the B species occupy tetrahedral sites. Inverse spinel occurs for the case of cations of transition metals such as in $NiFe_2O_4$ [17, 18].

The primitive tetrahedral unit cell of spinel consists of two molecular $AB_2O_4$ units in form of two octants. Four primitive unit cells form a cubic unit cell of spinel. Overall, there are 32 anions and 24 cations in each cell. The Bravais lattice of the spinel unit cell is face-centered cubic (fcc). The oxygen sublattice itself has also a cubic closed-packed (ccp) arrangement. Spinel has a lattice parameter of 0.80898 nm [17]. Figure 1.14 is a schematic illustration of spinel lattice consist of four tetragonal primitive cells.

The chemical bonds in magnesium aluminate are mostly of ionic nature [19]. Thus, as expected, spinel is a transparent insulator and chemically inert with high mechanical strength and high melting point of 2135 ℃ [20]. Due to aforementioned properties, spinel has found many application in refractory industries and protective shields for optical systems [21, 22]. Single crystalline spinel is also frequently utilized as substrate to grow thin films of various semiconductors and oxides [23–25].

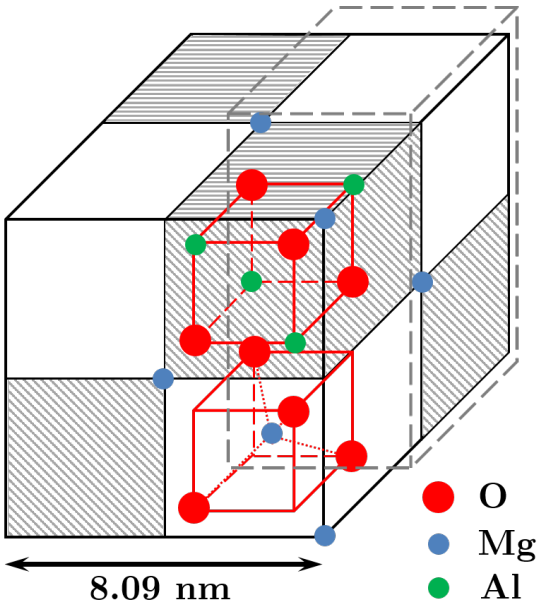


Figure 1.14: An illustration of spinel unit cell with tetragonal primitive cell marked in hatched borderline and arrangement of oxygen, magnesium, and aluminum inside. (Adapted from [17]).

### 1.3.2 Surface Properties

As can be expected, the lowest energy surfaces of $MgAl_2O_4$ are those of lowest miller indices which are: (100), (110), and (111) with energies of 2.27 , 2.85 and 3.07 $J.m^{-2}$, respectively [26]. Figure 1.15 illustrates a ball-and-stick model of spinel lattice rotated in directions aligned with or perpendicular to the (111) and (110) planes, same termination planes on the spinel substrates that are used in the experimental section of this study.

Due to its complex crystal structure, truncations along most crystallographic orientation of spinel yield an unbalanced net charge on each of exposed surfaces, hence causing microscopic *polarity* in the crystal structure. Perpendicular to the polar surfaces, any repeating unit bears a non-zero dipole moment causing an electrostatic instability. Electrostatic instability can be compensated in the outer planes by mechanisms involving change of surface stoichiometry—spontaneous desorption of atoms, adsorption of charge-compensating species, electron redistribution in the topmost layers of the crystal face, faceting, large-cell reconstructions due to the ordering of surface vacancies, etc [28, 29]. Such mechanisms alter the surface features such as planar crystalline

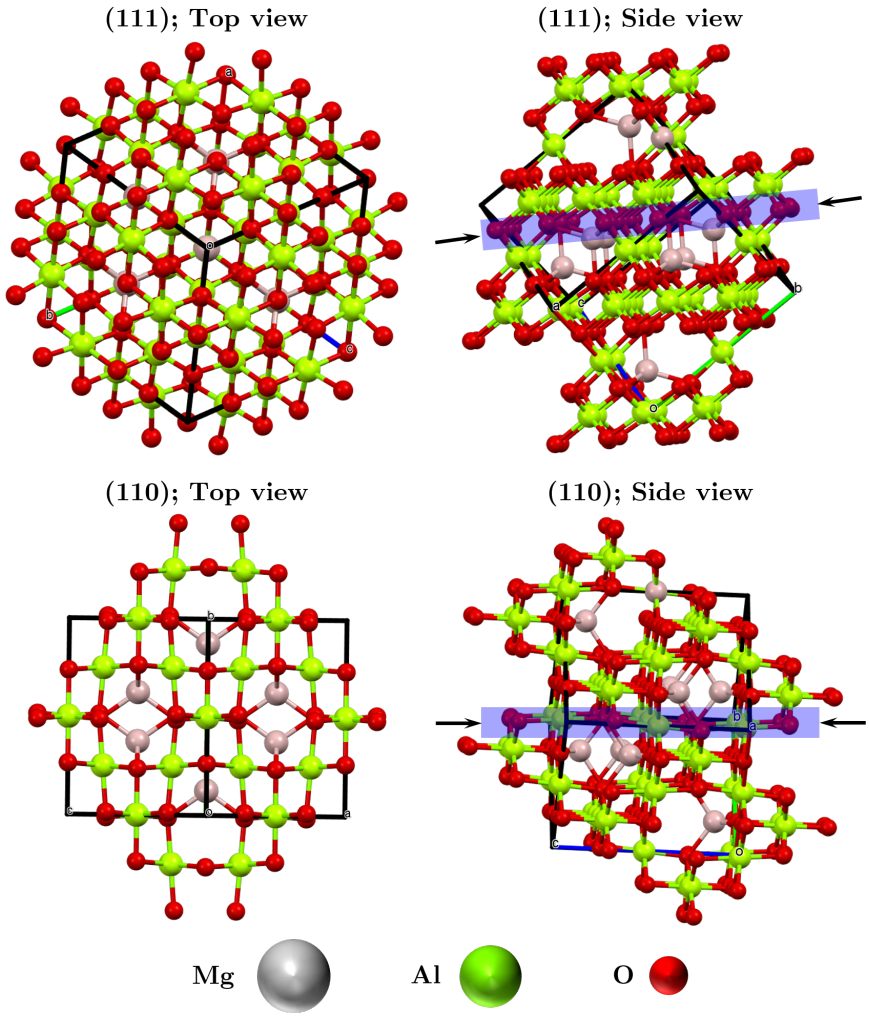


Figure 1.15: Top and side views from (111) and (110) planes of spinel lattice. (Generated by *Mercury* from a *.cif* dataset as provided by [27].)

order from those of the bulk.

Reconstruction is a process of reconfiguration of surface atom in a fashion that surface energy is minimized to equilibrium state through cancellation of unbalanced surface charge. In a specific case of (111) plane of spinel, freshly cleaved surfaces along this plane are often oxygen terminated, as the most stable (111) termination, and bear a negative charge. Providing the right conditions results in polarity relaxation through surface reconstruction. In a pioneering study by Rasmussen *et al.*, the reconstruction of this particular surface termination is investigated, using non-contact atomic force microscopy (NC-AFM) and X-ray photoelectron spectroscopy (XPS) in UHV. Their results indicate the formation of a new hexagonal (diamond) superlattice. Thus, they have concluded the most stable state of (111) surface is achieved through relaxation by reconstruction in annealing at high temperatures [29].

In their study, samples were prepared through successive cleaning cycles of argon sputtering followed by a heat treatment up to 1150 °C in an oxygen atmosphere. The process removes surface impurity, exclusively identifying Mg, Al, and O components. The excess of oxygen pressure guarantees the O-termination on the surface. In the course of process, reconstruction occurs by removal of 42 % of the topmost O atoms. NC-AFM reveals the reconstructed superlattice (or superstructure as described by authors) to be made of two patches of triangular sublattices, large and small, oriented in a way that small ones surround the large ones and are only separated by triangular outline of removed oxygens. An schematic view of the reconstructed surface is illustrated in Figure 1.16.

Formation of the outlines is argued to be necessary in order to both balance surface charge and to account for structures characterized by NC-AFM. Rasmussen *et al.* have then concluded that annealing spinel at temperatures about 1150 ℃ leads to surface reconstruction in which, oxygen anions are removed in a way that expose lines of Al cations and balancing the net charge on the surface to zero. Since there is a $O_3O - Al_3 - OO_3 - Mg - Al - Mg$ stacking sequence along [111] direction and since Al cations have two different coordination numbers, anion removal favors the formation of line vacancies exposing under-coordinated Al oriented on low-density lines of an underlying Kagomé lattice. The reconstructed superlattice still retains a 3-fold symmetry.

In a separate study, Yu [30] has reported on diffusion reactions at metal-oxide interfaces and the effect of an applied electric field. In this study, the effect of heat

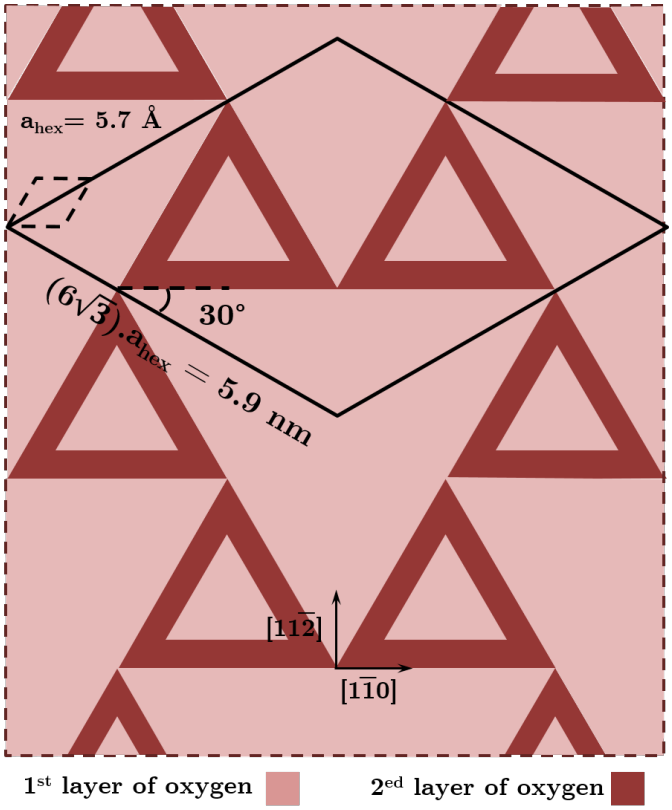


Figure 1.16: Reconstructed (111) surface of spinel with 2D lattice structure before and after the reconstruction. (Adapted from [29])

treatment and combination of heat treatment with applied electric voltage on the interface of $Al : MgAl_2O_4$ has been investigated. The temperature range used in this study is significantly lower than those used in Rasmussen's report. When system annealed (620 - 630 ℃) without an applied electric field, a {111}- and {100}-faceted phase of $\gamma - Al_2O_3$ formed at the interface because of diffusion of O into Al film and replacement of Mg ions by Al.

However, when $Al : MgAl_2O_4$ interfaces were annealed with an applied electric field, different results depending on the polarity of the applied voltage were observed. In case of a positive bias to the aluminum film, Mg ions diffuse deep into the $MgAl_2O_4$ substrate from the interface, leaving a Mg-deficient layer at the interface. But, in the case of a negative bias, pyramidal islands of 111-faceted $MgAl_2O_4$ form at the interface.

It can be deduced from Rasmussen's and Yu's studies that providing proper conditions (combination of metallic thin coat, heat treatment, and external electric potential) for an already unstable freshly cleaved (111) spinel may alter the surface structure and lead to growth of surface features mimicking the chemical composition and crystallographic symmetry of the underlying substrate. As it is shown in this thesis,utilization of gold coatings and high-temperature heat treatments can provide a better condition for achieving more pronounced surface alterations (self-assembly) of spinel.

## 1.4 Gold (Au)

### 1.4.1 Crystallographic Features

Gold has a face-centered cubic crystal with a lattice constant of 4.065 Å [31]. Golds lowest energy surfaces are those with the highest packing factors, *i.e.* (111), (100), and (110) with energies of 1.28, 1.63, and 1.70 $J.m^{-2}$, respectively [32]. Accordingly, these surfaces are the most stable ones and given thermodynamic equilibrium conditions, any single crystalline particle of gold would acquire a shape of truncated octahedron enclosed with only (111) and (100) planes, which can also be assessed through Wulff's construction [33]. Figure 1.17 shows the most stable facets of a gold fcc crystal and the equilibrium shape of a gold particle.

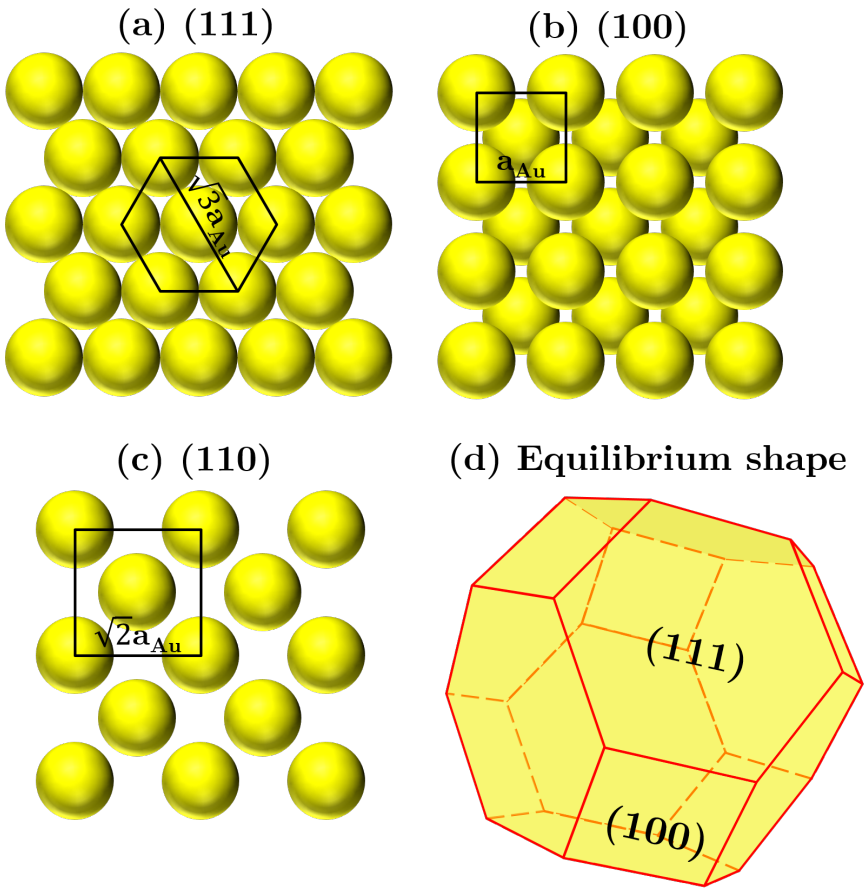


Figure 1.17: Three less energetic and most stable facets of a gold crystal; (a) (111), (b) (100), (c) (110), and (d) the equilibrium shape of a gold single-crystalline particle.

### 1.4.2 Physical and Chemical Properties

Gold is a transition metal with atomic number of 79. It is malleable and chemically noble, thus can be shaped in very thin foils of high purity by a few rounds of rolling. Although it is most stably found in pure state, it can readily form alloys with other metals. Most acids do not affect Gold. One of the few ways to dissolve gold is through reaction with aqua regia, a 1:3 volumetric mixture of nitric acid and hydrochloric acid. Nitric acid oxidizes the metal to +3 state, only in minute amounts. It is the role of hydrochloric acid that draws the equilibrium to the left side of the oxidation equation by forming soluble chloroauric ions, $AuCl^{4-}$, thereby enabling further oxidation [34].

Of other relevant physical properties of gold to this study is melting point of the gold. Bulk gold melts at 1064.18 ℃ and boils at 2856 ℃ [35]. However, melting-point depression is known to occur when the dimensions of a solid matter approaches the atomic scales. Due to this size effect, nanoparticles tend to melt at lower temperatures than that of bulk material and the melting temperature difference depends on diameter of the particle. Size effect can be justified by considering the increase in vapor pressure of solid due to highly curved shape and in ratio of surface tension to total energy, both resulting in instability of the nanometric solid particles and readiness to melt.

This effect has been studied theoretically and experimentally by Buffat and Boral on gold particles of different sizes, down to 2 nm, and a drastic drop in melting point has been observed in comparison with bulk gold. Figure 1.18 shows a diagram of the dropping trend of gold's melting point based on its particle size [36].

### 1.4.3 Relativistic Effects

Gold is somewhat unique amongst elements in that the relativistic effects play an influential role in its physical and chemical properties. Relativistic effects arise as a consequence of velocity of electrons in orbitals approaching speed of light and thus required to be described by relativistic quantum laws as opposed to non-relativistic Schrödinger equation. Accordingly, electrons moving within a considerable fraction of speed of light ($v \geq 0.1c$) have effective masses heavier than their masses at rest [37]. Electrostatic attraction between gold's nucleus and electrons is very high due to its high atomic number of 79. Based on special relativity the average radial velocity of the 1s electrons is $v_r = Z$ [atomic units], where Z is the atomic number. Knowing that $c = 2.998 \times 10^8 m.s^{-1} = 137\ a.u.$ electrons in the 1s orbital would have orbital

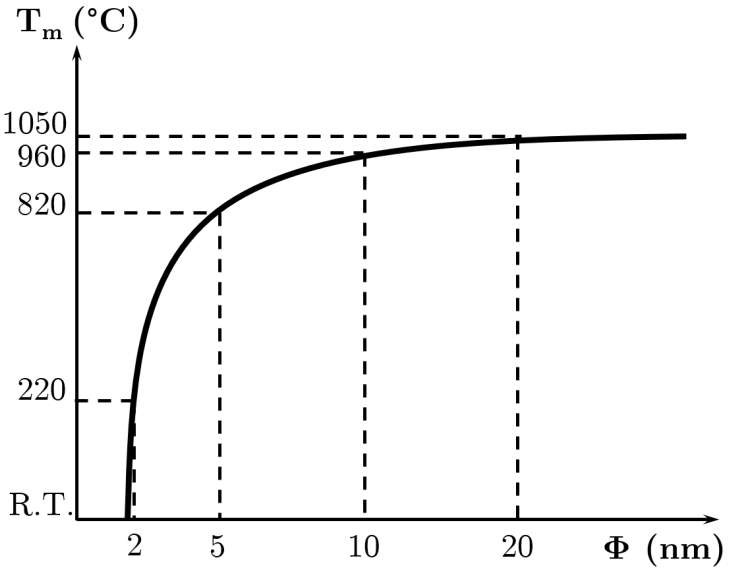


Figure 1.18: A curve of melting-point depression as a function of size shrinkage of gold particles. The temperature values indicated on vertical axis are only approximations intended to demonstrate the trend and do not represent exact experimental or theoretical values. (Adapted from [36])

velocity of $(79 \div 137) \times 100 = 58$ % that of light. Therefore, the mass of the electron will increase considerably [38, 39].

As Bohr's *solar system* model suggests, (Bohr) radius of an electron orbiting the nucleus is inversely proportional to the electron mass. By accounting for relativistic effects, any increase in mass of the electron causes a proportionate relativistic contraction of its orbit with constant angular momentum. To put this in Quantum mechanical terms, one can replace the Bohr orbits with a *probability distribution* of the electron's position and the Bohr radius defined as the distance from the nucleus to where the peak probability occurs. Relativistic effects most distinctly affect electrons in s orbitals even in outer shells, because their probability density remains high near the nucleus. However, to a lesser degree, the higher angular momentum p, d, and f orbitals are also affected. Relativistic effects also cause a stronger coupling between each electron's spin and orbital angular momentum [39].

This effect is translated as a high contraction of 6s orbital of the gold towards the inner shells, drastically increasing its ionization energy and reducing its chemical reactivity. Many other apparent anomalies in the physical and chemical properties of

gold compared with those of the other elements of Group 11 (IB), *i.e.* silver and copper, including color, specific resistivity, electrical heat capacity, melting and boiling points, and oxidation states can be understood only when relativistic effects are accounted for. Oxidation states of copper and silver are Cu(I) and Cu(II) and Ag(I) whereas, Au(I) and Au(III) are the most stable cations of gold. Increased Van der Waals interaction, increased physisorption energies on gold surfaces, and higher surface tension on low-index planes of gold are direct consequences of relativistic effects which in turn, affect the catalytic activity of gold [38, 40].

### 1.4.4 Catalytic Activity

Catalytic activity of gold is relevant to many technological applications. As a catalyst, gold can accelerate chemical reactions in effect, by reducing the activation energy barrier through formation of transient complexes and finally, reemerge intact at the end of reaction. Application of gold catalysts have been studied in two distinct systems; one, being the use of gold nanoparticles-on-oxide catalyst in charge exchange in gaseous reactions and the other is the use of gold seeds as preferential nucleation sites for the growth of semiconducting nanowires. It is noteworthy that gold in nanoscale (nanoparticles, nanometer-thick coatings, etc.) demonstrates catalytic properties.

Oxide-supported gold is able to catalyze hydrogen and oxygen transfer reactions under relatively mild conditions such as in case of oxidation of $CO$ to $CO_2$ and reduction of $NO$ to $NH_3$ and $N_2$ in presence of $H_2$. Catalytic activity of gold is reinforced when supported on a oxide such as $SiO_2$, $Al_2O_3$, and $MgO$. It is suggested that increased electron density at the Au sites (steps and kinks) facilitates electron exchange between gold surface and the adsorbed species, weakening the reactants bonds and catalyzing the formation of products [41, 42].

In their studies of gold catalyst, Okumura and Haruta cited reports of unsupported gold fine particles catalyzing the oxidation of $CO$ with apparent activation energies around 0 $kJ.mol^{-1}$ implying that $CO$ oxidation could be detected even at room temperature if unsupported gold (also referred to as homogeneous catalyst) particles are small enough to give larger surface area. They also noticed that when gold is deposited on the oxides of other metals (heterogeneous catalyst), the catalytic activity is remarkably enhanced. Such gain is more pronounced in case of reducible metal oxides having p-type or n-type semiconductivities such as $TiO_2$, $Fe_2O_3$, $Co_3O_4$, and $NiO$ compared with insulating, covalent bonded metal oxides like $Al_2O_3$ and $SiO_2$

[43, 44].

Hashmi and Hutchings have also reviewed various oxide supported gold catalysis for various chemical reactions as hydrogenation of alkenes and aldehydes, epoxidation, and the archetypal oxidation of $CO$ and several theoretical and experimental models explaining the catalyst mechanism. Although still a subject of debate, most mechanistic models emphasize the role of active sites on which reactants catalytically turn undergo oxidation reaction[45].

These active sites are found to be small crystallites of gold of 2-4 nm in diameter on a oxide surface. Some suggest that the peripheral atoms of gold at the interface, as well as the presence of defect sites, are the active oxidation centers, however, it is unclear whether $Au^{3+}$ (cationic) or $Au^0$ is the active form of gold. It is also argued that quantum size effects and the associated transition of electronic properties involved with such small gold particles may be a cause for catalytic reactivity of the system. Some models also point out to the role of oxide support, its size and stoichiometry, and its effect on the electronic properties of the gold maintaining the electron transfer and orbital hybridization at the interface as the source of catalytic activity [45].

Vapor-Liquid-Solid (VLS) deposition methods of semiconductors often involve utilization of a gold seed layer as a catalyst. It is believed gold seeds act as a liquid alloy source formed from the seed particle and the precursor(s) upon deposition process, leading to crystal nucleation and growth by precipitation from a supersaturated solution. Other catalytic mechanism has also been put forth pointing out to preferential decomposition of precursors at or near the seed particle surface which significantly heightens the growth rate in one (vertical) dimension [46].

In the case of Au:Si system, for instance, it is assumed that a liquid alloy of Au-Si forms at the seed particle and by constant dissolution of Si from vapor phase to the seed alloy, the concentration of Si reaches beyond the saturation levels of the system and thus, Si crystallizes through precipitation. Other works, however, suggest that catalytic decomposition of precursors on the particle surface in a process of dissociation of precursors at the particle surface, diffusion into the seed particle, and nucleation at the particle-substrate interface is responsible for the one-dimensional growth of the wires [46].

Forming deep-trap sites in semiconductor's band structure, gold severely alter the electronic properties of semiconductors. Therefore, there have been attempts to substitute gold with other metals as seed with lesser degrading effects. However, Au

is superior in producing well-oriented, narrowly size-selected nanowires compared to most other metals [46].

## 1.5 Complexions at Interfaces

Recent developments in high-resolution transmission electron microscopy have enabled novel revelations on the existence of intergranular films (IGFs) of equilibrium thickness in various ceramic-ceramic, metal-metal, and metal-ceramic interfaces. This discovery has linked two apparently unrelated phenomena in materials science that were not fully understood mechanistically in atomic scales only until recently: Abnormal Grain Growth (AGG), and Liquid metal embrittlement (LME) [47, 48].

IGFs along with surficial amorphous films (SAFs) are the two classes of the recently-discovered interfacial phases that collectively are referred to as interface complexion. Interfaces, surfaces, and grain boundaries cannot be defined as thermodynamic phases for they cannot be realized as stand-alone entities and therefore to be stable. Thus the term complexion refers to a state distinct from bulk and in form of a quasi-phase. Complexion represents an equilibrium state of matter at an interface and they are neither amorphous nor crystalline but show local order in their atomic coordination [49]. Complexions can be defined by thermodynamic variables (*i.e.* P, T, $\mu_i$, etc.) and, in that sense, they are similar to bulk phases. Equilibrium quantities such as entropy, adsorption $\Gamma_i$, and equilibrium thickness can also be associated with these interfacial phases. However, these properties cannot be separated from the bulk of material immediately adjacent to them [47].

Based on classical theories there are three distinct interfacial phases at grain boundaries: (i) intrinsic (clean) grain boundaries, (ii) Langmuir-McLean adsorption monolayer (or submonolayer), and (iii) complete wetting films. Recent developments in high-resolution transmission electron microscopy have enabled novel revelations on the existence of intergranular films (IGFs) of equilibrium thickness in various ceramic-ceramic, metal-metal, and metal-ceramic interfaces [48].

Thermodynamically induced phase changes in form of layering transitions of adsorbates from monolayers to multilayers in SAFs and the conditions and composition of constituents dictating what kind of complexion to form at IGFs underline complexions as equilibrium states for which, interfacial phase diagrams analogous to those of bulk phases can be constructed [49]. Dillon *et al.* have extended Gibbs definition of

phase (which applies to identifiable volumes that differ in their state, composition or symmetry, but not their geometrical features) to interface complexions. Complexion diagrams provide a means to predict and control equilibrium and kinetic properties that derive from interfaces [47].

There are also thermodynamic models that predict the existence and transitions of grain boundary complexions [49]. Complexion diagrams can be constructed to predict interfacial structure and chemistry based on different thermodynamic models of Gibbs isotherm, Cahn's critical point wetting theory, and force-balance. IGFs, they can be defined by the Gibbs adsorption isotherm [50]:

$$d\gamma = -\sum_i \Gamma_i d\mu_i \tag{1.25}$$

where an interfacial energy ($\gamma$) is reduced by the presence of interfacial excess ($\Gamma$) and a change in chemical potential ($\mu$). The Gibbs isotherm is a mathematical plane between the two phases that contains the interfacial excess which can be spread over several atomic planes [50].

Dillon *et al.* have pioneered identifying and categorizing different complexion layers at interfaces of alumina doped with different concentrations of calcia, silica, neodymia, and magnesia. Although, the system they have studied is a ceramic-ceramic interface, but any known complexion so far, at any ceramic-ceramic, metal-metal, and metal-ceramic interface, whether IGF or SAF, falls into their proposed categories of six complexions [47]. These six categories of complexions are [47, 49]:

I pure (no layer between the grains) or intrinsic boundary,

II sub-monolayer and monolayer adsorption of the solute cations,

III bilayer segregation of the dopant to the aluminum cation sites on the face of each adjacent grain,

IV trilayer (multilayer) adsorption of the dopant onto three cation layers within the grain boundary,

V amorphous nanofilms with a thickness that does not scale monotonically with dopant concentration and has a composition that does not correspond to the equilibrium bulk composition, and

VI wetting films with thicknesses that depends only on the amount of available liquid phase.

Dillon *et al.* measured activation energy (enthalpic contribution) for grain growth of all of the different aluminas and found it to be approximately constant, while the exponential prefactor (entropic contribution) varying significantly. So in correlation with their kinetic measurements, they concluded that highly disordered complexions at grain boundaries are the key to AGG phenomenon [47].

In another study, Baram *et al.* equilibrated 1.2-nanometer-thick films of anorthite glass at gold-sapphire interfaces and measured the solid-solid interface energy. They demonstrated that equilibrated film significantly reduces the interfacial energy. Unlike conventionally deposited thin films, these films do not suffer from rupture during equilibration by thermal means, indicating that these films at interfaces and surfaces can be an equilibrium state (complexion). Some key characteristics of these IGFs are that (i) their thickness and average composition are not subject to change along a particular interface or surface, and (ii) they are composed of Ca and Si at a different concentration than in anorthite. The reduction in energy due to the existence of IGFs was found to only exist at high angle (high-energy) grain boundaries, causing their energy to be reduced to the levels of low-angle (low-energy) grain boundaries [50].

Similar to IGFs, surficial amorphous films (SAFs) are stable quasi-phase at surface. Luo *et al.* demonstrated formation of the SAFs in systems such as $Bi_2O_3$ on $ZnO$, $VO_x$ on $TiO_2$, $SiO_x$ on $Si$ by heating up and cooling down the interface and observe the phase transition and wetting behavior of the system. SAFs can be stable well above the complete wetting transition coinciding with eutectic temperature analogous to frustrated-complete wetting. Therefore, SAFs are often referred to as prewetting metastable phases between complete wetting and dewetting states [51, 52].

SAFs discovered by Luo *et al.* are considered to be an intermediate regime between Langmuir submonolayer adsorption and complete wetting films and hence, fit to the categorization suggested by Dillon *et al.*. Equilibrium thickness in these surface complexions are adopted due to balance between several attractive and repulsive interfacial interactions including London dispersion forces, short-range repulsions of structural and chemical origins, electrostatic interactions, volumetric free-energy terms, and capillary and applied pressures [52].

The surface films observed in the study by Luo *et al.* have the following characteristics: they are partially or fully disordered; they conform to a nearly constant

thickness; they appear in single as well as multiphase samples; they have no apparent discontinuity in thickness, composition or structure at known bulk phase transition temperatures; and they are different in composition from the bulk phases [51]. All of these features are common among all types of complexions, IGFs and SAFs, as observed and explained due to aforementioned studies.

The studies by Baram *et al.* on dewetted gold on sapphire in presence of equilibrium anorthite IGF is very remarkable in that it is both fundamentally relevant to the topic of this thesis and also, until recently, was the only case of known ceramic-metal interface complexion. More recently, however, Majdi *et al.* have published their findings on the gold-spinel system announcing evidence for an *'epitaxial complexion'* at the $Au : MgAl_2O_4$ interface. The so-called epitaxial complexion is interpreted to be a complexion that is lattice matched to both adjacent phases. These epitaxial complexion bilayers, as argued by the authors, are associated with self-assembly of intricate gold-spinel nanoparticles (through dewetting gold overlayers atop of spinel) which also coincide with a strong epitaxial alignment of the three regions near the interface. Therefore, it is concluded that the bilayer is a complexion formed to minimize the free energy cost of the transition from the spinel to gold structures [53]. The conclusions by Majdi *et al.* are further investigated in Section 3.6: "Investigation Into the Interface of Gold-Spinel".

## 1.6 Characterization by Electron Microscopy

Electron microscopes are versatile instruments that provide us with well-rounded chemical and physical information about the materials, thanks to the variety of signals produced from electron-matter interaction. Superior resolution of electron microscope (EM) versus light microscope lies in the fact that electrons as (negatively) charged particles can be accelerated to such high velocities that can gain characteristic de Broglie wavelength much smaller than that of X-rays and hence, surpass the diffraction limitation of visible light by orders of magnitude. As such, illuminating probe of modern electron microscope, focused by means of 'magnetic lenses' can resolve images of extremely small objects.

The fundamental components of a normal electron microscope-much alike to those of a light microscope- comprise of: (i) an *electron source*, comparable to light source in LM, to emit beam electrons, (ii) a series of *magnetic coils* (*lenses*) and *physical*

*apertures*, as equivalent to optical lenses in a LM, that accelerate, focus, filter, and scan (or collimate) the beam of electrons, (iii) a *specimen chamber* including *sample holder* and various *detectors* to analyze the different signals coming off the specimen, after interaction with primary beam of electrons, and finally, (iv) a *column* evacuated down to high vacuum levels, encapsulating gun, lenses, apertures, specimen, and detectors in order to avoid undesirable interaction of electron beam with atmospheric species.

Electron microscopes are found in two major configurations; *Scanning Electron Microscopes* (SEM), and *Transmission Electron Microscopes* (TEM).

### 1.6.1 Optics of Electron Microscopy

Wave-like behavior of electrons manifests when they interact with orifices, thus the term "*electron optics*" is used to describe the phenomena associated with this interactions. Electrons waves diffract when passing through a narrow enough aperture restraining the resolution to a fundamental limit. *Resolution* is defined in terms of 'resolving power' of the microscope in distinguishing the smallest distance separating two clearly seen features via microscope. *Rayleigh criterion* gives the maximum achievable resolution in terms of diffraction conditions of a known wavelength passing through a aperture of known diameter. This criterion sets a minimum of 400 nm as the optimal resolution for an LM (using monochromatic green light as standard reference light), whereas a resolution of 0.006 nm can be achieved by modern high-resolution TEMs [54, 55].

Another outstanding feature of (scanning) electron microscope is its large *depth of field* (also referred to as depth of focus) compared with LMs. It is defined as the range of positions above and below the focal plane of convergent beam that remains in focus such that no notable loss of sharpness is observed in the image. Similar set of restraints applies to depth of field that it does to resolution *i.e.*, whatever that decreases the resolution also lessens the depth of field. Thus, a trade-off between resolution and depth of field produces best quality images. Nevertheless, the depth of field of SEM supersedes that of light microscope by orders of magnitude (in a same magnification and working distance) [54, 55].

*Optical aberrations* influence the process of making a convergent beam and consequently the quality of imaging; Diffraction aberration is the most fundamental one as discussed and only circumvented by avoiding apertures with openings smaller than the electron wavelength. *Achromatic* aberration which unfolds as emergence of different focal points due multicolored nature of electron beam. *Spherical* aberration manifesting

as electron rays of different energy converging into a disk instead of a focal point as the rays fall farther from optic axis. *Astigmatism* due to non-axisymmetric lens field that causes convergence of rays in different planes into different focal points. *Barrel* and *pincushion* distortions of image due to different magnification on off-axis rays [54, 55].

Lastly, formation of image and magnification mechanisms in electron microscopy should be considered. Although the mechanisms for image formation are different in scanning and transmission modes, a main characteristic of both is the utilization of set of magnetic lenses to manipulate the electron beam to restrict it to interact with a predetermined area upon arriving onto the specimen. This manipulation is in form of either converging and sweeping (by condenser lenses and scanning coils) the beam across the surface of specimen to form a raster in case of scanning mode electron microscopy, or collimating the illuminating beam and diverging the transmitted beam to form a projection in case of transmission mode [54, 55].

The *contrast* in SEM image is formed when the signals of rastered beam electrons are collected, processed, and assigned with a certain level of brightness proportional to the intensity of original signal. Magnification in SEM arises from the projection of each point on specimen surface to corresponding pixel on the screen. The ratio of pixel diagonal to the diameter of beam spot on the sample is the magnification value. On the other hand, contrast in a TEM micrograph is formed as a result of transmission of primary beam after partially being absorbed and scattered by the specimen leading to different signal intensities from each region on the specimen. Magnification in a TEM is achieved by multiple divergence of the transmitted signals via consecutive lenses and projecting it onto a viewing screen [54, 55].

### 1.6.2 Electron-Matter Interaction

Due to the impact of electrons onto the specimen and their interaction with specimen atoms, a burst of different signals is generated. Therefore, physics of electron-matter interaction reveals the nature of each type of signal generated which also provides an insight to material's structure. Due to high penetrating power of electron beam, an *interaction volume* forms right underneath the beam spot inside the specimen. In practice, this volume is assumed to encompass a region in which 90 % of the electrons-matter interactions occurs such that a high probability of leaving the specimen exists. Electrons can lose energy due to successive collisions and get absorbed before reaching SEM detectors. The maximum traveling distance of electrons inside the matter is

called *electron range* which is also used to simulate the shape of interaction volume. Such simulations suggest a hemispherical to pear-like shape for the interaction volume depending on electron range inside of a material [54, 55].

Interaction events are principally collisions between primary beam electrons and the specimen atoms which from a classical viewpoint are categorized into *elastic* and *inelastic* events. The distance between each scattering event is called *mean free path* of electron, $\lambda$, and is mainly affected by probability of elastic scatterings [54, 55].

During elastic collisions, primary electrons undergo repetitive rounds of Compton scattering, mainly from electric field of nuclei, such that almost all of their kinetic energy is still retained and only a minor portion (due to change of direction of motion) is converted to continuous X-ray emissions known as *Bremsstrahlung* radiation. Eventually, a fraction of electrons can turn their paths and exit the surface of material after cumulative changes of direction over the course of successive elastic collisions. These electrons are called *back-scattered electrons* (BSEs). The probability of back-scattering, or the elastic scattering cross-section, increases as a function of $Z^2$ (Z = atomic number). Thus, BSE signal and BSE contrast are atomic-mass sensitive. As Z increases, the interaction volume turns into a hemisphere due shortening of the electron range [54, 55].

In the course of inelastic collisions, primary electrons collide with the electronic orbitals of atoms in target material and therefore transform a large portion of their kinetic energy to the electrons of target atoms causing some of them to escape their atomic orbitals. The now itinerant electron, known as *secondary electron* (SE) can only leave the specimen surface if produced near the surface. As a result, SE signal and SE contrast are surface sensitive and are used for topography. Thereafter, an electron in higher orbital decays to fill in the vacant orbital to stabilize the atom and emits a *characteristic X-ray* radiation of that transition. Sometimes, another transition known as *Auger emission* is more favorable and that is when energy released from a decay is absorbed by an outermost electron and causes that electron to leave the atom [54, 55].

The chance of detection of each signal type depends on kinetic energy of signals which in turn, depends on the depth of their origination. As previously stated, secondary electrons have very low kinetic energy ($\sim$ a few tens of electron volts) and their yield of production decreases by going into depth, therefor only a fraction of them that are very close to surface ($\sim$ a few tens of nanometers) can escape. Same can said about the Auger electrons which leave the surface at extremely shallow depths ($\sim$ a few

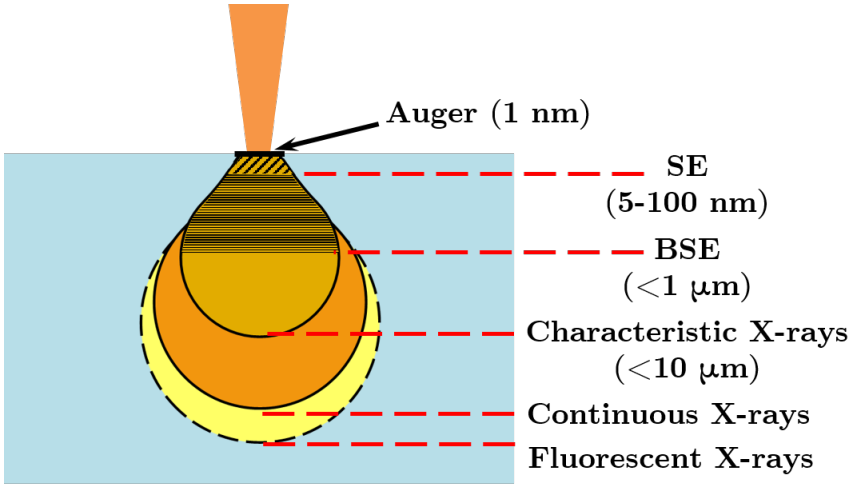


Figure 1.19: Interaction volume and the generation depths of different signals.

monolayers) whereas, primary electrons need to travel a lot inside the specimen before successive elastic interactions could render a back-scattering event. Consequently, BSEs come from a few hundreds of nanometers down the surface. X-ray radiations are also very energetic so they can escape from very deep under the surface without losing too much intensity [54, 55]. Figure 1.19 illustrates an interaction volume of electron-matter along with the depth of generation of each signal for a normal range of operating voltages.

### 1.6.3 Scanning Electron Microscopy

Scanning mode electron microscopy provides versatile analyses thanks to variety of signals being generated and detected in SEMs. In this configuration, a convergent beam of electrons is produced from a electron gun, filtered and focused through series of magnetic lenses and apertures, and rastered on the surface of a specimen by two pairs of scan coils. All the parts involved in generating the electron beam are contained inside beam column and permanently maintained in very high vacuum level. Beam column sits on a chamber, but completely isolated from it. The chamber houses the specimen holders and various detectors and is evacuated to high vacuum levels. Major parts of an SEM are illustrated in Figure 1.20.

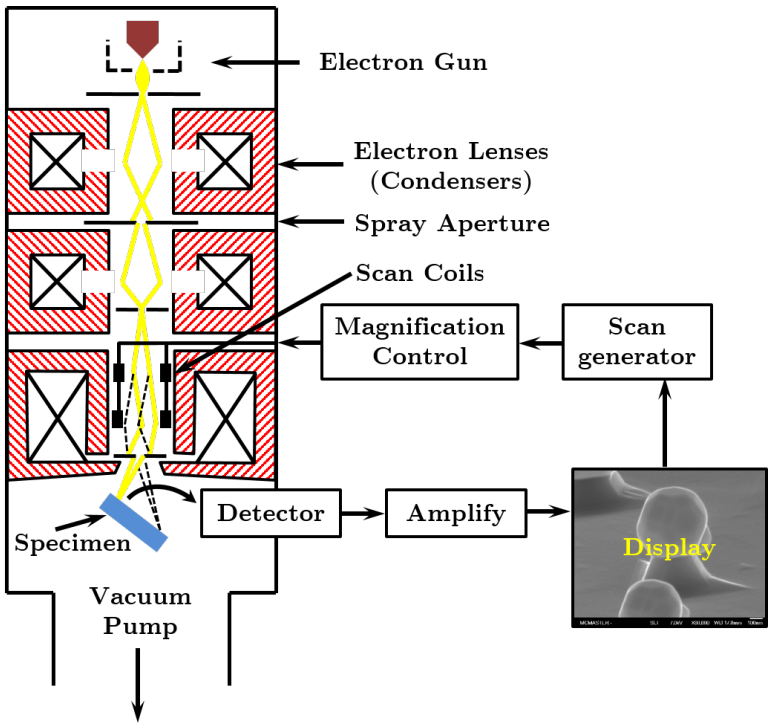


Figure 1.20: Schematic diagram of a scanning electron microscope showing the electron gun, lenses, scanning coils, and detection unit (Adapted from [55]).

#### 1.6.3.1 SEM Detectors

The main types of detectors inside an SEM comprise of Everhart-Thornley (E-T) detector, BSE (solid-state) detector, and characteristic X-ray detector in form of either Energy Dispersive X-ray Spectrometer (EDS) or Wave-length Dispersive X-ray Spectrometer (WDS). There are other types of detectors that are less frequently used and include Electron Back-Scatter Diffractometer (EBSD) and Auger Electron Spectrometer (AES).

Everhart-Thornley (E-T) detector: is widely assembled to SEMs to detect both BSE and SE signals with a main objective as to efficiently collect secondary electrons, however the BSE signal is often the dominant signal in proportion. Located in an acute angle with respect to specimen surface, the small take-off angle limits its field of view, but its large solid angle atones this limitation. A Faraday cage is also mounted on its end which once positively charged can collect electrons from a very large field of view. This Faraday cage can also be negatively biased to repel the low energy SEs and only attract high energy BSEs to conduct a pure Z-contrast analysis. In order to get a high flux of SE signal reaching the detector, Faraday cup is positively biased to +250 V, nonetheless the final contrast is a convolution of both surface topographic features (SE) and chemical characteristics (BSE) of the specimen [54, 55].

BSE detectors: are those that solely dedicated to BSE detection. Directionality and asymmetric position of E-T detector on one side of sample reduces detection efficiency. Higher BSE detection efficiencies is increased in dedicated BSE detectors as a result of large solid angle. Main types of these detectors include multichannel plate (or chevron) detector, passive scintillator detector, and solid-state diode array detector. Solid-state diode array detectors are more frequently used and consist of several diode chips assembled in form of annular or square plate located right below the pole piece. Each diode chip can operate autonomously so the detector can produce images of BSE signals coming from particular region of the specimen accepted from particular set of chips. Compound contrast is also possible by adding or subtracting the output signals of individual chips to emphasize a specific feature in this configuration [54, 55].

EDS detector: is most commonly used to analyze the characteristic X-ray

radiations from the specimen. For a sensor, this detector uses a reverse biased p-i-n semiconductor junction to convert X-ray photons of different energies to charge pulses. These pulsed are then converted to voltage pulses and after being amplified and shaped, are passed to a computer that creates a intensity versus photon energy histogram. Number of charge pulses and intensity of peaks in the diagram are proportional to the number of characteristic X-ray photons and indicate the abundance of a particular element in the specimen. Higher energy X-rays (heavy elements) generate a larger pulse and appear to the right of horizontal axis of diagram. Inversely, low energy X-rays from very light elements cannot incite intense pulses and thus blend in the noise level. Even modern EDS detectors cannot detect elements lighter than Boron [54, 55].

EDS detector is sealed from any environmental radiation and shielded against radiations created inside the chamber to avoid excitement of random pulses (noise). It is maintained in cryogenic temperatures by liquid nitrogen. Achieving a reasonable energy resolution depends upon the speed of electronic system of the detector. Since the sensor is incessantly producing a continuous train of pulses from incoming X-rays, the electronic system can easily get overloaded and pile up the peaks of distinct energies together. Therefor, for each measurement, detector only analyze fraction of pulses acquired while the electronic system is 'ON' and takes input (live time). It rejects the rest of pulses during the time the system is 'OFF' (dead time). Dead time can be adjusted by the operator through setting up the acquisition time and number of pulses wished to be analyzed [54, 55].

### 1.6.4 Generic Procedure for Specimen Preparation and SEM Analysis

Preparation procedure differs for the specimens of different types. For instance, treatments for organic samples are different from those of inorganic samples. However, a general process is inclusive to all kinds of the specimens which includes (i) mounting the specimen on a stub by conductive tapes or by applying metal (Ag, Ni, etc.) adhesive suspension; and (ii) coating the specimen with a very thin layer of conductive coatings such as C, Au, Pt, etc. thin enough to be transparent to electron beam and conduct the surface charge to ground. Otherwise, through constant bombardment of specimen by beam electrons, its surface gets saturated by negative charge and deflects the beam

from imaging area. This effect is known as charging effect and causes formation of exaggerated contrast and image drift on the screen in extreme cases.

To conduct a successful SEM analysis, the system parameters should be tuned according to the type of desired analysis. For instance, to perform surface topography, lower operation voltage (2-10 kV), medium probe current, and a small working distance ($\sim$ 6 mm) is generally advised, however the exact values should be selected based on prior knowledge on the features of the specimen to be analyzed such as chemical composition and size scale of the features on the surface. On the other hand, to conduct EDS analysis, it is important to have relatively high voltage ($>$ 10 kV) to ensure excitement of all characteristic lines and to have medium-high probe current adjusted such that the detector's dead time is between 10-40 % and the input\output signals are always above 4000 cps. Acquisition time should also be selected according to response time of the detector (normally around 20 s).

### 1.6.5 Focused Ion Beam Microscope

FIB microscope utilizes a beam of positively charged ions to produce images and perform other tasks as well. FIB is similar to SEM except it has an ion gun to produce the ion beam. Ion gun has a tungsten needle attached to a reservoir of liquid metal source. Gallium is most frequently used as the source material because of its low melting point (29.8 ℃), low chemical reactivity, low inter-diffusivity at melting temperature, and low surface free energy promoting its wettability on W needle. To extract and emit ions from the metal source, the reservoir is heated to melt the gallium and to wet the tungsten tip. Then, an electric field (on order of $10^8$ $V.cm^{-1}$) is applied to the tip causing the liquid Ga to form a *Taylor cone* with a tip diameter of 2-5 nm which is small enough for the *extraction voltage* to pull off field-evaporated Ga ions and produce a current density of $\sim 1 \times 10^8$ $A.cm^{-2}$ [56].

Single ion beam FIB can be used as stand-alone instrument, however it is generally incorporated to other microscopy systems and most commonly to SEMs as a FIB\SEM dual platform in which electron column is vertical and the ion column is mounted at some angle. Such instrument is highly flexible and versatile in performing variety of tasks as imaging, precision ion milling, and site specific micro-deposition. To conduct latter, FIBs are equipped with organometallic gas delivery systems that inject a gaseous source of material (normally Pt or W) into the specimen chamber through inlet needles. Real time deposition can be done as the ion beam reacts with the ambient gas (causing

its metallic part to break apart from organic molecule and be deposited on specimen) while the electron beam can image real time on the scene [56].

Typical FIB accelerating voltages range from 5 to 50 keV. Similar to billiard ball collisions, when an energetic ion hits the specimen, large amount of momentum is transfered to the specimen and release a burst of atoms and ions. Therefor, ion beam imaging is destructive. However, destruction can be useful when ion beam is deliberately focused on a region to carve away material on the specimen. Programming the beam parameters via computer enables us to deliver sophisticated cuts in different shapes and depths in nano- and micro-scales.With such capabilities FIB produces site specific samples from regions of interest to be further analyzed in other instruments such as TEM and atom probe tomography [56].

### 1.6.6 Transmission Electron Microscopy

The main parts of TEM, similar to SEM, are the vacuum column, the electron gun, magnetic lenses, and the detectors. The major difference between the TEM and the SEM is in the type of the specimen each of them can analyze. TEM samples should be electron transparent *i.e.* the sample should be thin enough so that a large fraction of beam electrons can pass through and not get absorbed or reflected. The accelerating voltage used in TEMs is higher than the SEMs, generally in range of 50-300 kV. Considering the electron range in different materials for this voltage range, the specimen thickness should not exceed 100 nm in the area of interest as it is required to have high enough signal transmittance for TEM analysis [54, 57].

Modern TEMs have extremely high resolving power with versatile configurations. For instance, scanning transmission electron microscopes (STEMs) can perform a basic TEM task while scanning the electron beam on sample. The state-of-art instruments have built-in aberration correction systems capable of correcting spherical and chromatic aberrations boosting the resolution to less than 1 Å.

### 1.6.7 TEM Analyses

Most of TEM analyses are done by TEM-specific detectors of which the viewing screen (for image and diffraction pattern acquisition) and the EELS detector (for chemical analyses) are the most important ones.

#### 1.6.7.1 Viewing screen

Viewing screen is simply a means of forming the electron image or diffraction pattern through the conversion of electron signal intensities to the optical contrasts visible by eye. This has been traditionally done by introducing a photographic negative film on the screen and chemically developing of an image after certain amount of exposure. Modern TEMs nowadays utilize charged couple cameras (CCD) arrays in order to form instant digital images form the electron projections.

#### 1.6.7.2 EELS detector

EELS detector is a spectrometer dedicated to chemically analyze specimens. EELS stands for Electron Energy-Loss Spectroscopy and measures the energy loss in the inelastically scattered beam electrons that are transmitted from the specimen. The principal mechanism of EELS detection is to bend paths of electrons inside the magnetic field and disperse the transmitted beam into a spectrum of different energies. Each electron lands on a different position of the detector depending on its kinetic energy. The arrival position of electrons will then be used to calculate the energy loss of scattered electrons from primary beam electrons.

In the course inelastic electron-matter interactions, the electrons lose a characteristic equal to the amount consumed to excite a transition process in electronic shell of atoms. These processes may be single-electron or multiple-electron (collective) excitations. Single-electron events include *inner-shell* and *outer-shell* electron excitations, *intraband* transitions of valence electrons, and liberation of *secondary electrons*. Collective excitations, however, involve oscillations of the electron density of an ensemble of atoms known as *plasma resonance* or *plasmons*. Plasmon energy lies within the range of 5–30 eV for most solids [58].

The resolving power of EELS system is evaluated in terms of *spatial* and *energy* resolutions. Lower energy spread of primary beam, high accuracy of magnetic field in EELS prism, and high spatial resolution of the detector (more pixels) yields in better energy resolution. Modern EELS's can achieve energy resolution in order of meV. To further enhance the energy resolution, some EELS systems use a combination of electric and magnetic fields to increase the energy spread of transmitted beam by decelerating the electrons. De-excitation processes, in the case of single-electron events, result in characteristic X-ray or Auger electron emissions. Characteristic X-ray are

collected and analyzed by the EELS counterpart, EDS. EELS is superior to EDS in that it has higher spatial and energy resolution and it is more sensitive to light elements. However, in terms of quantitative analysis, both EELS and EDS have roughly the same detection limits [58].

EELS results are typically represented as electron energy-loss spectrum, showing the count of electrons as a function of decrease in their kinetic energy. However, it is also possible to create elemental maps of an area with different elements.

### 1.6.8 TEM Modes of Operation

#### 1.6.8.1 Imaging and Selected Area Diffraction

When a parallel electron beam is illuminating the specimen, an 'objective lens', immediately after specimen, focuses all the diffracted and transmitted electron rays. Below that a set of 'projector lenses' magnify the image of objective lens onto the viewing screen. Of these lenses, the first one is often called *intermediate or diffraction lens*. Intermediate lens is a strong magnetic coil that can change focal point by adjusting it's magnetic field strength and place it whether on image plane of objective lens to render an image of specimen or place it on 'back focal plane' of objective lens, where there is a diffraction pattern of specimen formed, and magnify the diffraction pattern. In this latter mode, by positioning an intermediate physical aperture in the image plane of the objective and just allowing the rays from desired area of the specimen to pas through, selected area diffraction (SAED) is implemented. These two modes are represented by ray diagrams of Figure 1.21.

#### 1.6.8.2 Bright and Dark Field Imaging

All transmitted and all diffracted rays leaving the specimen combine to project an image at the viewing screen. As can be seen in Figure 1.22, a full image forms with only those rays passing through one point in the back focal plane. All rays entering a given point have all been scattered by the specimen into the same angle which distinguishes the points in the back focal plane. By positioning an *objective aperture* at a given point in the back focal plane, an image is made with only those electrons that have been deflected by a certain angle: when the aperture is positioned to pass only the transmitted (un-diffracted) electrons, a *bright-field* (BF) image is formed.

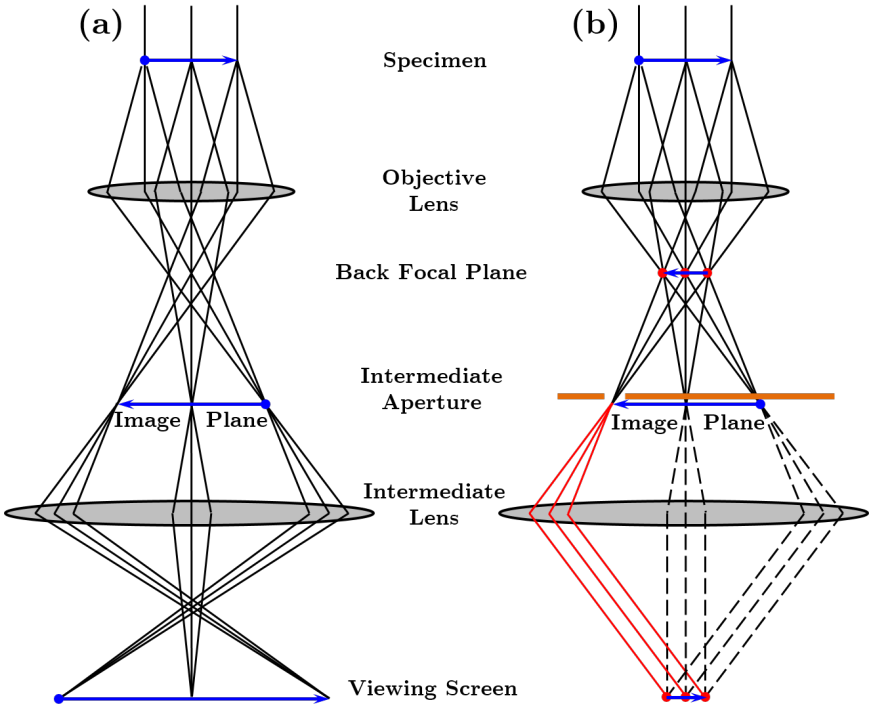


Figure 1.21: The ray diagram of (a) imaging mode and (b) diffraction mode in a TEM. The different components of each mode and their positions are schematically shown (Adapted from [57]).

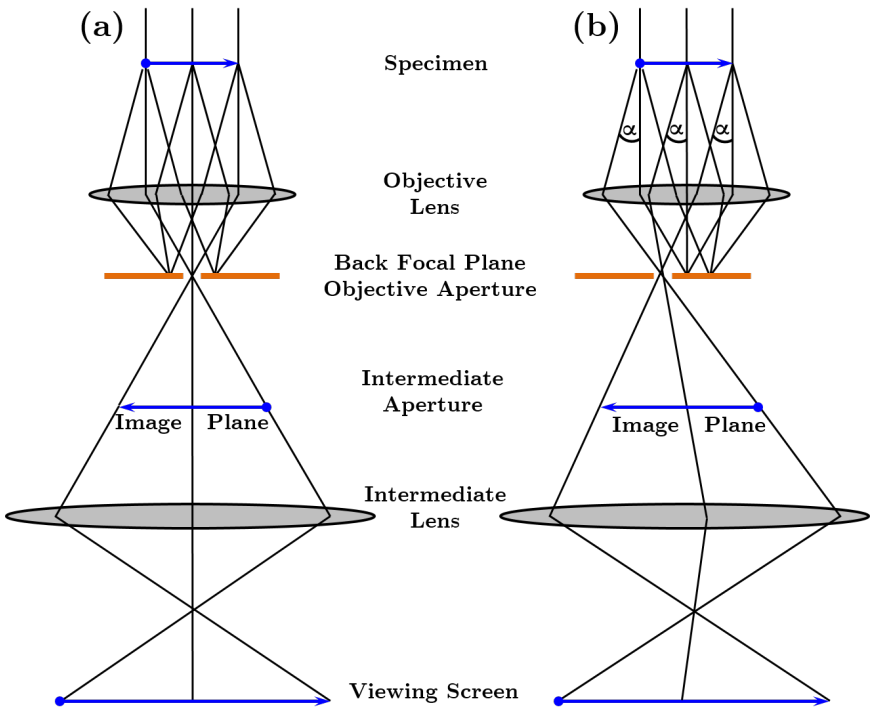


Figure 1.22: Specific position of objective aperture in the back focal plane in order to image at: (a) in bright field; and (b) in dark field (Adapted from [57]).

When the aperture is positioned to pass only some diffracted electrons, a *dark-field* (DF) image is formed.

#### 1.6.8.3 High Angle and Low Angle Annular Dark Field Imaging

Conducting the HAADF and LAADF modes requires an STEM with extremely narrow electron probe and annular detectors located below the sample as shown in Figure 1.23. The scattering profile of primary electrons depends on their incident energy, as well as, the atomic number of the scattering atom. Heavy atoms tend to scatter electrons in high angles (similar to Rutherford experiment) and have brighter contrast in HAADF mode. Crystallinity of the sample is also important to image contrast, since HAADf transforms the signal intensity of a 'column' of atoms to contrast [57, 59].

HAADF detector collects elastically scattered electrons that are deflected in angles larger than typical Bragg diffractions (in range of 75-15 mrad). The detector collects those signals that fly outside the $\beta$ angle, which is 2-3 times larger than the beam convergence angle $\alpha$ (as in Figure 1.23). In LAADF, however, the scattered signals

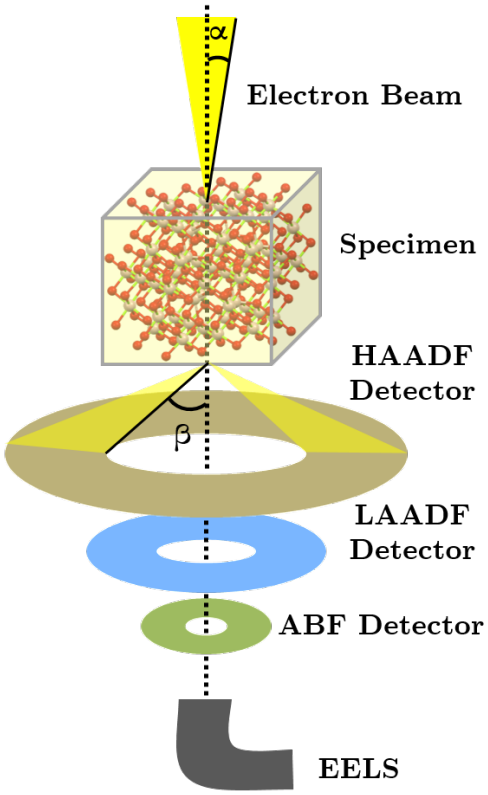


Figure 1.23: Configuration of HAADF, LAADF, ABF, and EELS detectors inside a high-resolution STEM (Adapted from [59]).

within the inner cone of $\beta$ are collected for imaging. Unscattered and inelastically scattered signals may be collected to perform annular bright field imaging (ABF) and EELS analysis [57, 59].

## 1.7 Characterization by Atom Probe Tomography

Atom Probe Tomography (APT) is a member of family of techniques known as field microscopy that are based on electric field desorption of atoms from surface of a needle-shaped specimen and projection map of the atoms onto a detector illustrating the atomic configuration of the specimen tip. Field Ion Microscopy (FIM) was the first technique to resolve atoms. State-of-art APT instruments are based on FIM and are also capable of chemically analyzing the specimens.

### 1.7.1 Field Ion Microscopy and Tomography: Principles of Field Microscopy

In this method a narrow needle-like specimen with a tip diameter smaller than 100 nm is made, inserted to a VHV apparatus in extremely low temperature (5-80 K) that applies a high positive voltage (generally up to 10 kV) to the specimen. Electric field at the apex of the specimen reaches to $10^{10}$ $V.m^{-1}$. At this point, an inert *imaging gas* like helium or neon is introduced to the vicinity of positively charged specimen. Gas atoms become polarized as they approach the specimen and migrate to the tip of the specimen, where the electric field density is highest. The gas atoms cover the surface and undergo a field induced ionization as an electron of the gas atom tunnels through the vacuum barrier into the specimen tip. The probability of ionization in the vicinity of the hemispherical tip is higher where the charge density is higher. So, the adsorbed gas atoms on atomic steps and ledges of the tip have higher chance of ionization and acceleration towards the detector. Th ions projected on a screen would show field distribution on surface of the specimen tip [60, 61].

Since the surface of the cathode (detector) is very large in comparison with the specimen tip, the positively charged ions traverse a diverging pathway towards the negative pole following the electric field lines and project a highly magnified map of the atomic configuration of the specimen tip onto the detector. The atomically resolved image of the tip forms on the detector illustrating a crystallographic coordination of topmost surface atoms. The magnification is proportional to the ratio of tip-to-detector distance to tip radius [60, 61].

Increasing the electric field in a field ion microscope could result in ionization and desorption of surface atoms of the specimen in process known as *field evaporation*. Successive removal of slices of atoms from the surface exposes deeper layers of the specimen lattice with each layer mapping the crystallographic configuration of surface. If each slice of the ionized atoms is imaged in order of arrival time on detector screen, then a 3-dimensional arrangement of the specimen can be reconstructed by arraying the images together based on temporal precedence [60, 61].

Effectively temporal detection is possible by avoiding the slices to intermingle during their flight towards the detector. To achieve this goal, specimen evaporation is pulsated. Doing so, the ion accelerating voltage is separated from evaporation voltage, *i.e.*, the ion accelerating voltage is applied as a constant moderate DC voltage, which

normally does not surpass 2-3 kV and the evaporation voltage is applied in form of a train of high voltage pulses with known and controllable duration and separation. The high voltage can reach up to 10 kV. This gives a time window between each detected slice so that the stacking order of the layers can be retraced following their precedence [60, 61].

It is also important to note that as result of large Coulombic force, very high electrostatic field puts a lot of stress on a 100 nm diameter specimen even if the specimen is a ductile metal. For instance, in case of an aluminum sample the so-called *electrostatic pressure* reaches to 1.6 GPa, enough to plastically deform pure aluminum. So in this regard, specimen failure chance is very high due to sudden fractures. Although, pulsed removal of atoms substantially decrease the time that the specimen is under electrostatic pressure, but cyclic nature of the stress increases odds of fatigue failure [60].

### 1.7.2 Time-of-Flight Mass Spectroscopy

Time of flight mass spectroscopy (ToF-MS)is an elemental analysis of species by measuring the time of flight of their ions accelerated in an electric field, of known strength, and determining their mass-to-charge ratio. The mass-to-charge ratios are unique characteristics of any chemical element so that chemical identification of a specimen is possible by attributing the right mass-to-charge ratios to the corresponding element [60, 61].

Field desorption and photo-ionization are two of the most frequently used ionization techniques in mass spectrometers. Furthermore, in a ToF mass spectrometer an electric field is used to accelerate ions towards the detector. Ions constantly gain momentum directly proportionate to their charge states and inversely proportionate to their masses as they traverse in the electric field. For a known flight path and acceleration voltage, the calculated mass-to-charge ratio would match to a unique element in unique isotopic form and charge state providing a very high resolution of chemical characterization [60, 61].

Most of Mass spectrometers use chevron-based micro-channel plate (MCP) as detector which further increase the resolution and sensitivity of the mass spectrometer. Chevron microchannel plates are basically arrays of micrometer diameter V shaped glass tubes biased at about -1 kV at the end facing towards the ions. The inner walls of the tubes are coated with thin conductive films. When an ion enters the tube and

hits the tube wall, it knocks out a bunch of electrons. These electrons then accelerate towards the other end of the tube constantly hitting the wall in a zig-zag path and creating a cascade of free electrons that ultimately generate an amplified signal and induces a current pulse into detector [60, 61].

The collected data is called the *mass spectrum* and is represented as a histogram of ion abundance versus mass-to-charge ratio. The units of mass-to-charge ratio are expressed in *Daltons*. 1 Dalton defined as the ratio of 1 atomic mass unit (amu) over 1 elementary charge unit ($1.6 \times 10^{-19}$ coulombs). Any ionized element that is detected during spectroscopy would appear as a peak on its corresponding Dalton number(s) [60, 61].

### 1.7.3 Modern Atom Probe Tomography

Modern day atom probe tomography methods are developed by incorporating the principles of time of flight spectroscopy to field ion tomography in a single instrument that is capable of providing the outcomes of both methods. They further use femto-second pulsed laser with ultraviolet wavelengths as ablation sources for ion desorption advancing the application of technique to various types of materials (alloys, ceramics, etc.) and lowering the chance of electrostatic stress failure. The result of the atom probe tomography is a 3-dimensional elemental reconstruction of the specimen thus, the technique is also referred to as three-dimensional atom probe (3DAP) [60, 61].

The state-of-art atom probes are the *Local Electrode Atom Probe* (LEAP). The basic parts of the LEAP are same as the traditional atom probes and based on field ion microscopes. Needle shaped specimen, UHV chamber, and an aerial detector. The only exceptions are the introduction of a local counter electrode that provides the electrostatic potential to accelerate the evaporated ions and the utilization of ultrafast pulsed lasers as the evaporation source [60, 61].

### 1.7.4 Acquisition, Reconstruction, and Interpretation

Since laser ablation is not a perfect ionization process species like atoms and complex ions and fragments can also reach the detector and complicate the chemical analysis. During APT run, a '*golden ratio*' of ions to all registered species is constantly surveyed to be above 90 %. By adjusting the laser power and accelerating electric field, golden ratio can be regulated [60, 61].

For the purpose of even evaporation, the laser scans the tip surface which also complicates z-axis reconstruction. This problem is overcome by using advanced reconstructing functions. There is also a '*detection ratio*' set to ignore most of species and accept only those that fly within a 'reasonable' angle. The ratio lies within a range of 0-1 percent. Thus, not all positions in specimen tip are represented and the final reconstruction is actually of an inner cone enclosed in sample. The advantage of low detection ratio is, however, the impurities on the surface from milling and the coating substances are not present at 3-d reconstruction [60, 61].

Theoretically, material is evaporated in order of successive hemispherical slices top-down. In practice, however, the tip imperfections results in charge concentration at sharp edges and the order of removal might not match the z-axis (specimen axis) profile. Though, the process is self-regulatory and the almost hemispherical shape gets restored [60, 61].

As each laser or electrical pulse is applied, a few atoms ionize and reach detector. Time-of-flight ($t_{flight}$) of each species is calculated and recored as the time between end of pulse and the species registration on detector. The aerial detector of APT is also sensitive to geometry and can record x and y coordinates of species arrival spot. The z-axis component of each species simply emerges by keeping the order of its arrival so that the earliest species makes the topmost position of reconstructed sample. The 4-coordinate ($t_{flight}$,x,y,z) data point are assigned to each registered species at detector [60, 61].

4-coordinate ($t_{flight}$,x,y,z) data points are reconstructed to a specimen representation by APT software. Firstly, a mass spectrum is created based on ToF data and each peak is manually assigned to corresponding elements. The 3-d graphic reconstruction begins with generation of 2-d slices (of removed atoms) using x,y, and (already known) chemical identity. Then using the z-axis order, slices are stacked upon each other to give the 3-d shape. Operator can input parameters like tip shape (from prior imaging), d-spacing of crystal planes, and the zone axes that appeared on desorption map which helps crystallographic positioning and alleviates more representative reconstruction [60, 61].

## 1.8 Related Literature on Metal Film Dewetting

In this section a review on major studies about dewetting different metals on various substrates for different applications is given. Then, different aspects of complexion layer quasi-phase from formation to characteristics are reviewed. And finally, the most relevant studies on the dewetting of gold thin films on spinel substrates are apprised.

### 1.8.1 Dewetting of Metals on Oxide Substrates

Dewetting metals on a substrate is a cost-effective means to produce supported metal particles of different shapes and sizes [62]. The group of metals dewetted to produce particles comprises of Au, Ni, Ag, etc. [63–65]. The types of oxide substrates used as supports are $Al_2O_3$, $SiO_2$, $TiO_2$, $SrTiO_3$, etc. [66–69]. Dewetting, as discussed in previous sections, is performed through promoting the rupture in metal thin films deposited on oxide substrates by providing thermal energy. Several less conventional methods are applied to initiate and promote dewetting such as laser-induced, microwave plasma, ion-beam-induced dewetting, etc. [70–72]. These techniques are capable of geometrically patterning particles, also allowing for higher control over heating time scales and a better insight into film relaxation.

Although unrestrained metallic nanostructures have applications in numerous technological fields, the applications of oxide supported metallic nanoparticles, to great extent, are limited to catalytic templates for growth of semiconductor nanorods, catalyzing chemical reactions, surface enhanced Raman scattering efficiency, and plasmonics and producing negative index materials (metamaterials) [44, 46, 73–75]. Among metallic nanoparticles Au and Ag are the most utilized for plasmonic and catalytic purposes.

The catalytic applicablity of oxide supported gold particles are specifically relevant to this work, because it underscores the gold reactivity in metal-oxide interfaces as it was elucidated in Section 1.4.4. Oxide supported gold nanoparticles catalyze reactions of a third phase (*i.e.* semiconducting nanorods and gaseous reactants) and direct reactivity between gold and its oxide support has never been reported before except by those working on the same project as current thesis at McMaster university [76, 77]. The following section explains the previously done research on the catalytic-like behavior of gold when a thin film of it is dewetted atop of spinel substrate.

### 1.8.2 Preceding Studies on Dewetting of Gold on Spinel

Previous experiments on dewetting gold thin films on top of single crystal spinel substrates by heating the system at temperatures near or above the melting point of gold have shown self assembly of intricate particles that resemble a spherical grain sitting atop of a frustum (truncated pyramid). Such intricate structures are considered to be unique to this particular film-substrate system and have never been observed in similar systems.

Early studies by Devenyi *et al.* on dewetted extremely thin gold layers have concluded that the formation of such intricate structures is a result of self-assembly of gold. The self-assembly process takes place through initial epitaxial rearrangement of gold atoms form the dewetted islands of gold at high temperature on spinel, followed by formation of a necking region and a spherical dome to minimize the surface free energy. The overall shape and size of the structure is then determined by an interplay between competing constraints imposed by epitaxy and the surface free energy, as the author suggests [76].

The analogous behavior of soap bubbles affixed to wire frames with the system in study has driven the proposed hypothesis and the "continuum elastic surface" model of gold nanostructures presented in their report has yielded satisfactory results in predicting the structure of nanoparticles during the heating process. The geometry of the faceted footprints were known to be adapted form the crystallographic symmetry of the underlying spinel substrate where the (100), (110), and (111) surfaces with four-fold, three-fold, and two-fold symmetries impose square, triangular, and rectangular geometries to the epitaxially formed footprints [76].

Further studies on the system were done by Majdi *et al.* in order to get a better insight as to how and why such intricate structures form. During these studies, the effects of principal parameters like temperature profile and the thickness of initial gold overlayer on the shape, size, and structure of the ultimate structures were investigated in order to corroborate the hypothesis that epitaxy (crystallographic) and surface tensions (thermodynamic) are the chief driving force of the intricate structures formation [53, 77].

Preliminary observation revealed that the gold intricate structures are not uniformly consist of gold and in fact are made of two completely separate bottom and top parts that are spinel pyramids/frustums and gold spherical caps, respectively. First

hint to suggest such odd composition had come from the different contrasts of the bottom and top parts observed from electron micrographs taken through carefully adjusted operating parameters in a extremely high resolution SEM. This observation along with the presence of some uncapped pyramids and frustums on some samples which seemed to be inexplicable by continuum elastic surface model, reinforced the suggestion of a hybrid gold-spinel compound rather than a monolithic gold structure. Further experimental analyses of the samples by HR-STEM and electron back-scatter diffractometry (EBSD- done by S. R. Zainab [78]) confirmed the compound nature of the intricate structures. Cutting through the structures with FIB and observing the exposed surface in HR-STEM, along with the electron diffraction patterns from EBSD had revealed the distinct boundary in gold-spinel interface and made distinguishable the chemical and crystallographic characteristics of each phase[53, 77].

In addition, It was demonstrated from HR-STEM and XRD analyses that gold particles are single-crystalline with epitaxially arrangement of gold atoms in the gold-spinel boundary. Diffraction results also point out to preferential alignment of the gold's [111] direction with that of (111)-spinel substrate, or $[100]_{Au}$ and $[110]_{Au}$ directions with those of (100)- and (110)-spinel substrates, respectively [53, 77].

It is thus concluded that despite the shortcomings of continuum elastic surface model suggested by Devenyi for describing the intricate shape of particles, the assumption of epitaxy force and surface energy as the driving forces of shaping the structures is still correct. Careful experimentation by Majdi on the effect heat-treatment profile and the thickness of initial gold film yields to the observations that are compatible with the idea that epitaxy and surface energy are the main cause of spinel self-assembly and formation of intricate structures. These observations include the increase in number density of the intricate structures per surface area and the enlargement of self-assembled spinel necking structures with the increase in annealing temperature and duration [53, 77].

Overall, most important results and conclusions from the studies by Devenyi and Majdi can be summarized as follows [53, 77]:

i Heat treating a thin film of gold on single-crystalline spinel substrate at temperatures around that of surface reconstruction of spinel will cause the gold film to dewett and motivate self-assembly of spinel.

ii Intricate gold-spinel structures, consist of a bottom part of spinel necking and

a top part of gold spherical nanoparticle, are almost always separated by a flat abrupt boundary.

iii The driving forces behind the formation of intricate structures can be attribute to an interplay between epitaxy and surface energy taking place during a rather long heat-treatment process.

iv Gold particle almost always appear as single crystalline with a preferential alignment of gold's crystallographic direction with the matching direction of spinel's surface normal due to epitaxial restraints; that is, $[111]_{Au}||[111]_{spinel}$ in (111)-spinel substrate and so forth.

v High resolution transmission electron imaging and electron loss spectroscopy reveal formation of a 2-dimensional crystal of gold-oxygen bilayer dubbed as complexion layer which is believed to be formed as a result of quasi-phase equilibrium only adjacent to gold and spinel at each side.

# Chapter 2

# Equipment and Methodologies

This chapter is dedicated to describe the experimental procedures that were implemented to first produce and then characterize the samples. Production stage begins with preparing the substrates and then depositing the desirable thin film, heat treating the system, and characterizing the ultimate product via several methods follow. Each of these steps are briefly explained in following sections:

## 2.1 Substrate Preparation

Spinel substrates come as single crystalline wafers of 2.5 in diameter, one and/or two side polished, with chemical formula of $MgAl_2O_4$ and a quoted roughness of less than 5 Å on various surfaces of (111), (110), and (100), packaged in a class 1000 clean room, and sold by MTI corporation. Wafers were unpacked in a class 1000 clean room, coated with positive photo resist solution of MICROPOSIT S1808 (Shipley Company) on a spin coater instrument to protect the polished surface of $MgAl_2O_4$ dust, and dried to be subsequently cut into desired sizes. Dicing was done using a LoadPoint MicroAce 3 dicing saw, with a diamond impregnated resin blade, made by CISCO, G1A851 SDC320R13B01. Spindle speed of 15000 rpm, feed rate of 2 mm/sec, and water lubricant (does not dissolve photo resist) were used during dicing. Wafers were cut to sample sizes of $5 \times 10mm^2$.

It is necessary at this point to thoroughly clean the substrate surface to prepare them for the deposition step. The cleaning procedure involved three-stage ultra-sonic bath rinsing; in a proper sized beaker and using a Teflon holder, substrate(s) were

dipped into hot high purity liquid chromatography (HPLC) acetone (60 °C), cold HPLC acetone (room temperature), HPLC methanol, and HPLC isopropanol baths, respectively, each for sonication periods of 45 minutes. Before, changing the sonication bath's solvent, all parts and containers in contact of substrates were manually irrigated with the solvent of next step to avoid cross contamination. All chemical solvents were of analytical grade (HPLC) purchased from Caledon Laboratory Chemicals. Consequently, substrates were dried and stored in desiccator to be used for deposition in future. Light microscopy (Zeiss Axioplan 2) utilized to check for traces of remaining particulate and solvent residue and if found the cleaning procedure reiterated until no sign of contamination observed via light microscope.

## 2.2 Thin Metal Film Deposition Methods

Deposition of metal thin films was done using three different systems: sputter coating system, thermal evaporation system, and e-beam evaporation system. each system is different from another in terms of vacuum pressure, rate of deposition, and creating film-substrate binding that ultimately affect the quality of sample. The preparation of samples with each if these systems is described in following sections with regards to the quality of their outcome.

### 2.2.1 Sputter Coating

Sputter coating is a Physical Vapor Deposition (PVD) method in which material is deposited by ejecting its atoms from a target source onto a substrate. During sputtering an electric field is formed between positively biased target (cathode) and negatively biased anode with the substrate atop. Sputtering reaction is done through (positively) ionization and acceleration of sputtering gas (noble gases like argon) towards cathode that when reaches a certain kinetic energy can knock out atoms from target material. Those atoms that gain enough energy through collision with gas ions can reach to the substrate surface and ultimately form the thin film.

In this project sputter coating was utilized to deposit thin films of gold, copper, aluminum, platinum, and carbon (only for purpose of making conductive layers on electron microscopy samples). Sputtering conducted via Ar plasma which the Ar gas constantly is fed into chamber. Other parameters such as voltage and current were

adjusted according to the target specifics like density of target material and desirable rate of deposition. The rate of deposition along with the base pressure of vacuum in sputtering chamber are the most important parameters that control the quality of deposited film in terms of purity, integrity, smoothness, and binding to substrate. The optimum rate of deposition is determined through a compromise between a reasonable deposition time and quality of film. It is observed through experience that the optimum rate ought to be kept below 1 Å/$s$.

Two different machines were used to sputter-coat thin films on the spinel substrates. GATAN PECS model 682 ion beam coating/etching system and Torr Compact Coater model CRC-600 featuring a higher vacuum chamber and capable of DC/RF mode coating with precision thickness control. GATAN PECS allows to set parameters such as accelerating voltage, guns current, deposition rate, base pressure, and sample rotation speed, tilt angle, and rocking speed. These parameters were set to 5 keV, 150 $\mu A$, 0.8 Å/$s$, $5 \times 10^{-5}$ $Torr$, 60 RPM, 0, and 0, respectively for depositing gold films. On the Torr Compact Coater machine, the base vacuum pressure was normally around $6.9 \times 10^{-6}$ $Torr$ and deposition vacuum pressure was around $6 \times 10^{-3}$ $Torr$. All depositions were conducted in DC voltage mode (V = 312 v and I = 30 mA). Ar flow rate adjusted at a constant 25 SCCM. Voltage and current were controlled and adjusted constantly based on deposition rate which was kept between 0.8-0.9 Å/$s$.

### 2.2.2 Thermal Evaporation Coating

Thermal evaporation coating also falls under the PVD category. In this apparatus, small amounts of target material is heated beyond its melting point until the vapor pressure on top of the target exceeds the ambient pressure of the deposition chamber, which is a vacuum of around $10^{-5}$ $Torr$, and a vapor flow can reach the chilled substrate and condensate to form the film. Deposition rate can be controlled by adjusting the superheating of the target which essentially regulates the vapor pressure.

Thermal evaporation in this work was conducted in a metalizer with a bell-jar chamber. Target metal (Gold) was placed in an alumina crucible mounted on a tungsten element. substrates were put upside down (facing the crucible) right on top of target with an approximate distance of 15 cm. Bell-jar was then placed on system and sealed to pump down the chamber to vacuum levels of around $10^{-4}$ $Torr$. Liquid nitrogen used to facilitate the depressurizing the chamber by creating a cold finger. Current applied to element which heated the crucible and the metal inside and caused

melting the target, crating the sufficient vapor pressure. Film deposition was only permitted when the condensation rate on a reliable thickness measuring unit (a quartz crystal microbalance - QCM) matched the desirable deposition rate by removing the substrate blanker.

The vacuum level on traditional bell-jar systems is not as high as in sputter coater or high-vacuum e-beam evaporation coater due to inferior sealing. On the other hand, it is also more difficult to control the rate of deposition with accuracy of the other two depositing methods due to longer response time of vapor pressure to temperature adjustments. Overall, quality of films produced via this method cannot match with those of sputter coated and e-beam evaporation coated.

### 2.2.3 E-beam Evaporation Coating

Also categorized as a member of PVD family, e-beam evaporation technique exploits high energy electron beam to heat and evaporate a target material instead of resistive heating. In this method a beam of highly accelerated electrons (8-10 keV) impacts the target material and the high kinetic energy of the beam electrons deposits into the target's lattice causing it to melt and evaporate, however, since the depth of impact is very low, melting only occurs at the very top and rapidly re-condensate thus, resulting in very small amount of target to be consumed.

Electron beam is produced by a conventional electron gun very similar to those that are used in electron microscopes (e-gun description can found in electron microscopy section). Typical accelerating voltage in e-beam evaporation is about 8-10 keV. Inside the deposition chamber, the configuration of e-gun, target holder, and substrate is such that e-gun lies out of target's line-of-sight and the substrate and target material directly face to each other. This configuration guaranties the uniform coating of substrate surface in a Lambertian emission. To reach the target that is normally located on top of the e-gun, the electron beam must bend in a magnetic field provided by electromagnetic coils. There are also other coils used to wobble the beam off its axis in order to heat the target evenly.

The UHV Instruments e-beam evaporation apparatus was utilized to produce gold thin films. The instrument is located in a class 1000 clean room and benefits from a ultra-high vacuum (UHV) deposition chamber capable of depositing several metal films at the same run. The thickness of deposition were measured on a QCM. Deposition rate of 0.8 $\text{Å}/s$ was adapted to coat samples with constantly adjusting the operating

voltage around 10 kV and the beam current of 1.8 mA to properly evaporate gold. The base pressure was around $4 \times 10^{-8}$ $Torr$ and the deposition vacuum pressure was around $5 \times 10^{-6}$ $Torr$.

## 2.3 Heat Treatment Procedure

Thermal treatments implemented to induce dewetting and self-assembly of metal thin films coated onto spinel substrates. All of thermal processes were carried out using a Lindberg Hevi-Duty "clam-shell" furnace nesting a quartz tube. Electrically heated tungsten elements provide the furnace heat. A thermocouple, placed in the center of the top shell connected to a CN4800 temperature controller provided real-time temperature readouts. Temperature measurements were received and analyzed on a LabVIEW program which was also used to program the heating process and gas flow in the tube.

Almost all of the heat treatments were under 99.9995 % purity argon flows at 100 standard cubic centimeters per minute (sccm) from the an Air Liquide Medical gas cylinder. Exhausted argon was passed through a two-stage gas bubbler filled with vacuum oil before being vented to air from outlet. Most of thermal processes were carried out after the tube was completely purged with argon for two hours.

To verify accuracy of the temperature, furnace was run to its maximum temperature (1200 ℃) and all readings were referenced to a bath of ice water, using a reference junction type R (Pt-13 % Rh vs. Pt) thermocouple. It was observed that the furnace is capable of delivering the input temperatures within a ±5% of tolerance.

Investigated temperature profiles in this work mainly emulate those trends adopted by Devenyi [76] and Majdi [77] for the gold-spinel samples. These profiles are designed with two important temperatures in mind: one is the melting point of the metal thin film and the second is the temperature in which spinel undergoes a surface reconstruction. The temperature of spinel's surface reconstruction is reported to be around 1150 ℃[29]. One would expect to observe high mobility of spinel's atoms in this temperature which might also explain the reassembly of these atoms into frustums and pyramids in presence of gold.

The general trend in each heat treatment profile is a ramp from room temperature to first soaking stage and soak for a certain time, following a ramp to the second soaking stage and soak again for a certain time, and finally ramp to room temperature.

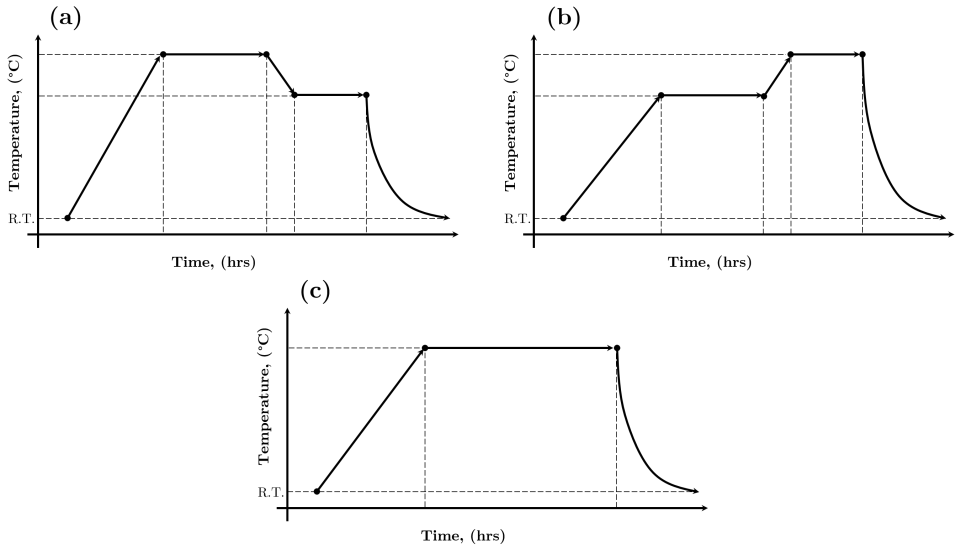


Figure 2.1: Schematic graphs of different types of heat treatment process in this work: (a) Double soaking stage with the first stage of higher temperature, (b) Double soaking stage with the second stage of higher temperature, and (c) Single soaking stage.

Two-stage heat treatment process is ostensibly crucial to formation of spinel necking structures as argued by Devenyi and Majdi [76, 77]. However, experiments in this work have shown that single stage heat treatments in longer hours are as effective in formation of those structures. Figure below shows a schematic of different types of heat treatment profiles.

## 2.4 Characterization Methods

### 2.4.1 SEM and Related Analyses

Scanning electron microscopy utilized to mainly conduct topographic surveys via secondary-electron mode, as well as, chemical analysis via EDS. All SEM characterizations conducted by a JEOL JSM-7000F machine.

Accelerating voltages of mostly 3-5 kV, probe currents of medium to high levels, and working distance (WD) of mostly 6 mm used for top-view flat imaging with E-T detector. To further investigate the topographic features, tilt mode imaging conducted using 45° and 70° tilt angles in working distances not less than 15 mm (due to chamber restrictions).

Chemical analysis was performed first with acquiring BSE signal images at accelerating voltages of more than 10 kV, medium probe current, and WD of 10 mm on a BSE solid-state detector. Then, EDS conducted for qualitative and quantitative chemical analysis of specimen constituents.

### 2.4.2 Specimen Preparation

Specimens were first glued to aluminum SEM stubs using silver paste. After several hours of drying period in room temperature, samples were sputter-coated by conductive coatings of carbon (mainly) and platinum with thickness of around 5 nm.

### 2.4.3 HR-STEM and Related Analyses

HAADF imaging and EELS analysis conducted to investigate the gold-spinel interface using an aberration-corrected FEI Titan 80-300 HB instrument. Operation conducted at 300 kV acceleration voltage with beam convergence semi-angle of 90 mrad and collection semi-angle of 36 mrad. EELS analysis performed using Gatan Quantum EELS spectrometer operating at the same convergence semi-angle and collection semi-angle. The beam exposure time per pixel (*i.e.* per probe spot on the specimen) was 0.01 ms.

### 2.4.4 Specimen Preparation for HR-STEM

FIB system (ZEISS Gemini) has been used to prepare samples of gold-spinel interface with thicknesses less than 100 nm for transmission electron microscopy. A region of interested were selected on specimen containing a row of gold-spinel intricate structures. Then tungsten coating applied to completely cover the region in a form of rectangle block. Ga-ion milling used to cut the region and thin it down to less than 100 nm. An automated micro-arm used to position the sample on a TEM half-grid made of molybdenum.

### 2.4.5 Atom Probe Tomography

Atom probe tomography carried out to examine the chemical features of the gold-spinel interfaces using a CAMECA LEAP 4000 XHR series APT machine. Needle like specimens of tip diameter around 50-60 nm were posited on conical posts of a silicon

coupon and inserted to UHV chamber ($P_{base} = 3.69 \times 10^{-11} Torr$) under cryogenic temperatures (tip temperature = 60-65 K).

Field evaporation conducted in pulse laser mode using a solid-state UV pulsed laser with wavelength of 355 nm. Pulse rate of 160 kHz and laser energy of about 80 pJ were the main input parameters for laser. Time of flight measurements were carried out in electrostatic field of acceleration and acceleration voltage was started from 1.8 kV and increased automatically with tip diameter increase to keep the evaporation rate somewhat constant.

Stop voltage was set to 10 KV, 3-4 kV higher than the voltage that experimentally known to cause fracture. In successful runs voltage rose to about 3-4 kV where on average about 15-17 million ions were collected, well through the gold particle, gold-spinel interface, and spinel necking, so the run was considered successful and stopped manually. Chromium coatings were applied on the samples with thickness of about 50-60 nm and they were found beneficiary in preventing fracture by ameliorating the excess heat dissipation to silicon post.

In the course of evaporation, the detection rate set be about 0.005 ions/pulse (0.5 %) considering a detection efficiency of about 36 % (instrument intrinsic). The golden ration of the single ions to overall evaporated species was on average about 90 %. A successful APT run of the gold-spinel samples running at the aforementioned setup parameters would usually take about 5-8 hours.

Reconstruction of the data performed via IVAS 3.6.12 software of CAMECA company using conventional reconstruction algorithms as described in [60]. The process started with identifying the peaks of mass spectrum and then reproducing the 3D shape based on the available chemical identifications. The most accurate and reasonable reconstruction achieved on the basis of tip profiles from FIB images which provided an approximation for tip diameter evolution by considering the shank angle of specimen and the depth of evaporation. Reconstructions based on d-spacing of gold planes or ratio of voltage/tip radius were not representative of specimens as the samples were not consist of a homogeneous phase throughout.

### 2.4.6 Specimen Preparation for APT

FIB system used again to produce needle-shaped samples. The process was similar to one used for TEM samples except here, instead of thinning the the whole block of region of interest, individual gold-spinel structures were set on each silicon post

by cutting and welding the rectangular block and trying to center the gold-spinel intricate structures on posts. Then annular Ga-ion milling applied to shape needles with diameters in range of 50-60 nm suitable for ATP analysis. A further low-energy top view ion imaging conducted on individual samples to carve away W coating and expose the gold underneath so that the APT run would take shorter time to reach gold-spinel interface without depositing to much heat and stress in the sample.

# Chapter 3

# Results and Discussion

## 3.1 Formation of Gold-Spinel Intricate Structures

As noted in Section 1.8.2, Devenyi *et al.* had reported formation of intricate 'sphere-on-pyramid' intricate nanostructures of dewetted gold on spinel substrates. Further studies by Majdi *et al.* disputed the Devenyi *et al.* proposition of monolithic intricate structures based on experimental evidence of electron microscopy and crystallography (from Zainab's EBSD work) that showed two separate bottom and top parts in the structures [53, 76–78].

It was the main objective of current study to reproduce the results of Majdi and further advance them to gain better insight at the unprecedented phenomenon of formation of gold-spinel intricate structures and the following novel episodes such as formation of quasi-phase interface complexion. During this project, various experimentations were carried out, as described in Chapter 2 'Equipment and Methodologies', the results of which are accounted in the following parts. It is shown that results of Devenyi and Majdi works are reproducible when carefully following their proposed methodology, however, in light of additional experimental evidences, some of the previous conclusions as to mechanism of the spinel self-assembly underneath gold and the formation of interface complexion are challenged.

## 3.2 Effect of Heat Treatment

Two-staged annealing profiles were adopted by Devenyi and then Majdi in order to form gold-spinel intricate structures. These profiles have the following general trend: a ramp to high temperature of about 1050-1100 ℃ (close to the temperature of spinel's surface reconstruction), keeping the sample at that temperature for 1-2 hours, cooling down to temperatures about 950-1000 ℃ (just below the melting point of gold, 1064 ℃), keeping the sample at that temperature for another 1-2 hours, and then cooling it down to room temperature. The effectiveness of this trend is argued to be crucial in formation of gold-spinel intricate structures since adatom kinetic energy is kept in a desirable level of surface migration while gold particles undergoing solidification [76].

Most of the work on investigating the effect of annealing parameter is done by Majdi which mainly includes studying the range of temperatures and durations in various gold film thicknesses and observing the morphology and crystallinity of dewetted gold particles. In general, Majdi has concluded that first, there is a lower bound of temperature for onset of gold-spinel intricate structures formation and second, increasing the annealing temperature and duration to certain point causes an increase in the size of those structures, especially in the spinel necking, however beyond that point, the size increase of structures is hindered (and reversed) and the spinel necking structures alter from tall frustums to almost flat triangular pits. The Lower temperature and time limits are argued to be within 1050-1100 ℃ and 1-2 hours for the first soaking stage in which the spinel's surface begins to appreciably change due to reconstruction. Maintaining such high temperatures for longer hours would cause severe gold evaporation and consequent shrinkage in size of spinel frustums [77].

In the current work, we investigated the suggested effectiveness of two stage soaking profile, then the effect of extreme soaking temperatures and durations, and finally the effect of a rapid ramp from room temperature to the high temperature by means of introducing the sample into a preheated furnace. These results complete and slightly modify the picture given by Devenyi and Majdi in terms of annealing effects on gold-spinel structures.

It should be noted that the main objective of studying heat treatment parameters is based upon the following assumption: heating the system to temperatures in a range of 1100-1150 ℃ provides the energy to activate the spinel surface for reconstruction process while melting gold (or increasing its diffusivity in solid state) in spinel's

adjacency. The vicinity of these two processes results in gold catalyzing a surface reaction involving the loosened components of spinel to self-assemble in a fashion that also satisfies surface relaxation of unreconstructed spinel. The formation of complexion layer is also argued to be the thermodynamical driving force for the whole process as the surface tensions of both spinel and gold are reduced when a boundary layer complexion is present. Thus, the reaction continues as long as the adequate thermal energy is provided. The validity of this picture is, however, disputed in subsequent sections.

### 3.2.1 Effect of Single Soaking Stage Heat Treatment on Formation of Gold-Spinel Intricate Structures

Figure 3.1 illustrates the SEM images of two (100)-spinel samples sputter-coated with (a) 20 nm of gold and (b) 5 nm of gold and annealed at single soaking stage of (a) 1150 ℃ for 6 hours and (b) 900 ℃ for 6 hours. As can be seen, in both samples, gold films have dewetted and formed gold nanoparticles. However, in sample (a) intricate structures of spinel-gold have clearly formed whereas in sample (b) there is no sign of formation of such structures.

Intricate gold-spinel structures in sample (a) consist of a spinel frustum with square base, due to four-fold symmetry of (100) surface, with a gold spherical particle on top. Gold particles have developed a peculiar pear-like shapes with well-faceted surfaces. A general six-fold symmetry belonging to (111) surface of gold appears to have grown parallel to (100) surface of spinel, even though epitaxy force does not favor such relation. On the other hand, the gold particles appear to be polycrystalline rather than single crystalline which undermines the expected epitaxial growth. It is also noteworthy that most particles appear to be slanted that can be a result of prolonged duration of heat treatment which has caused formation of sharper spinel bases and gold particles to tip over.

Our observations in this case contradict those of Devenyi and Majdi that have argued single stage profiles cannot yield formation of intricate structures [76, 77]. This inconsistency can be explained when the initial thicknesses of the films are put into consideration. The initial film thickness in sample (a) is 20 nm which is four times higher than the normal thickness values reported by Majdi [77]. Higher film thicknesses allow for running harsher thermal processes without significant loss of

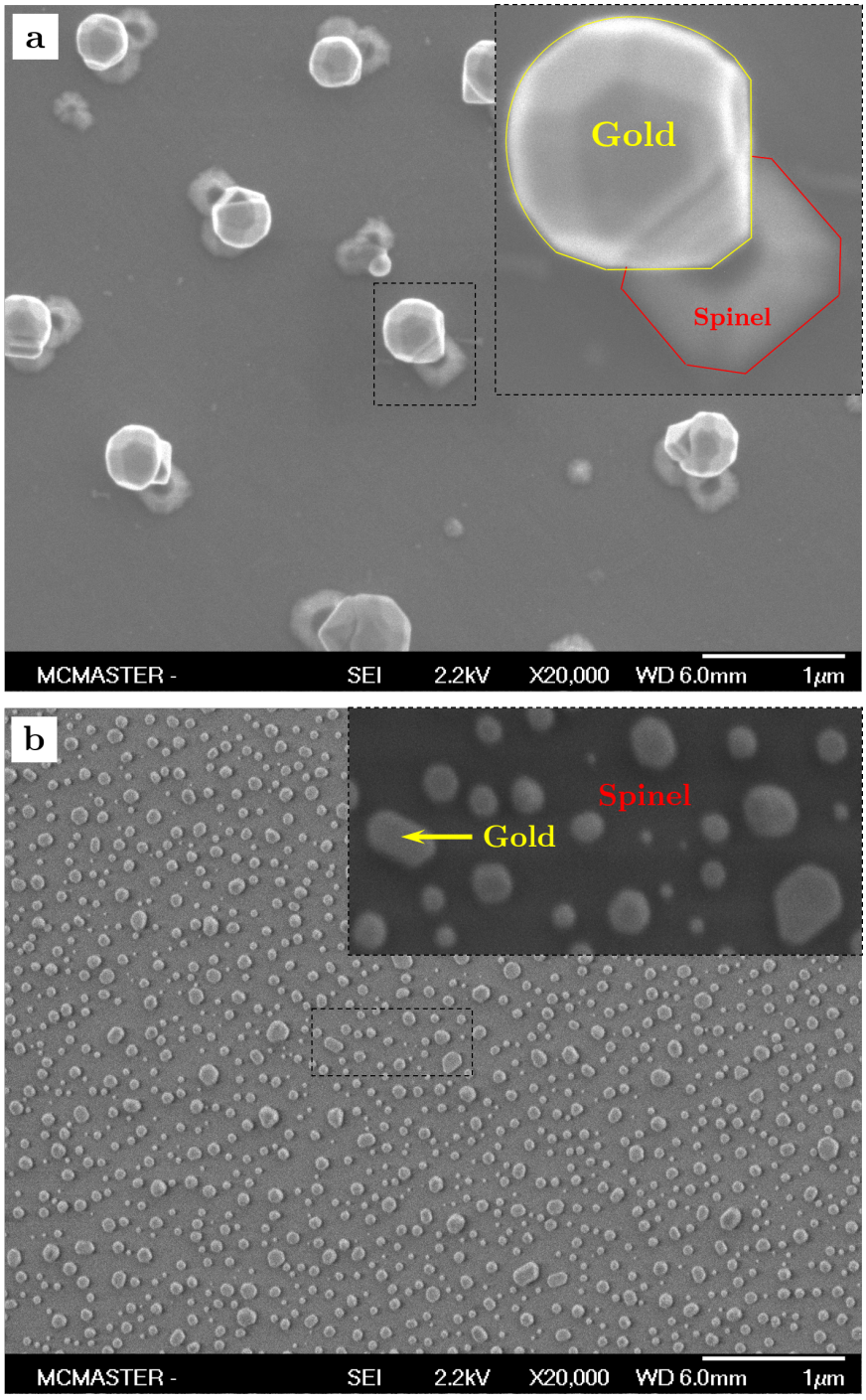


Figure 3.1: (a) (100)-spinel sputter-coated with 20 nm of gold and annealed at single soaking stage of 1150 ℃ for 6 hours, and (b) (100)-spinel sputter-coated with 5 nm of gold and annealed at single soaking stage of 900 ℃ for 6 hours.

gold to evaporation, which in turn, expedites the process of formation of intricate structures.

In sample (b), however, the initial gold film has barely dewetted resulting in rather squat particles. Since 900 ℃ is considerably lower than the melting point of gold ($T_m$ = 1064 ℃), even when accounted for the nanoscale size effects, it is therefore expected that the gold film has undergone a solid-state dewetting process which results in particles with irregular shapes and high disparity in average diameter. These findings are compatible with those of Majdi on samples annealed at low temperatures [77]. The gold particles are densely packed on the surface of sample (b) whereas the intricate structures are quite dispersed in sample (a), however, the average size of gold particles in sample (a) is larger than that of particles in sample (b).

It should be noted however, that double stage heat treatment process is somewhat more effective in self-assembly of larger spinel necking structures (starting with an initially thinner gold film) by reducing the evaporation of gold. Therefore, most of the heat treatments conducted in this research have two soaking stages and the results can be compared and contrasted with those of Devenyi's and Majdi's.

### 3.2.2 Effect of Extreme Annealing Temperature and Duration on Formation of Gold-Spinel Intricate Structures

To investigate the effects of extreme thermal conditions, a (111)-spinel substrate was sputter coated with 50 nm of gold and annealed at 1190 ℃ for 4 hours, cooled down to 1050 ℃ and held at that temperature for another 4 hours. 1190 ℃ was chosen in order to not damage the quartz tube which has a nominal temperature limit of 1200 ℃. Electron micrographs of this sample are presented in Figure 3.2.

As can be seen, the extreme annealing conditions have effectively caused gold thin film dewet and form gold-spinel intricate structures. The gold particles are spherical and less faceted with average size of about 500 nm. Some of the larger gold particles appear to have irregular protrusions on their sides corresponding to a different grain that is infused to the main particle. The nature of these protrusions is explained in subsequent sections. Moreover, the spinel frustums appear to be stubby with several layers stacked upon each other. Most of the frustums are capped with gold particles but some of them have no gold particle on top. These bare spinel structures are exposed

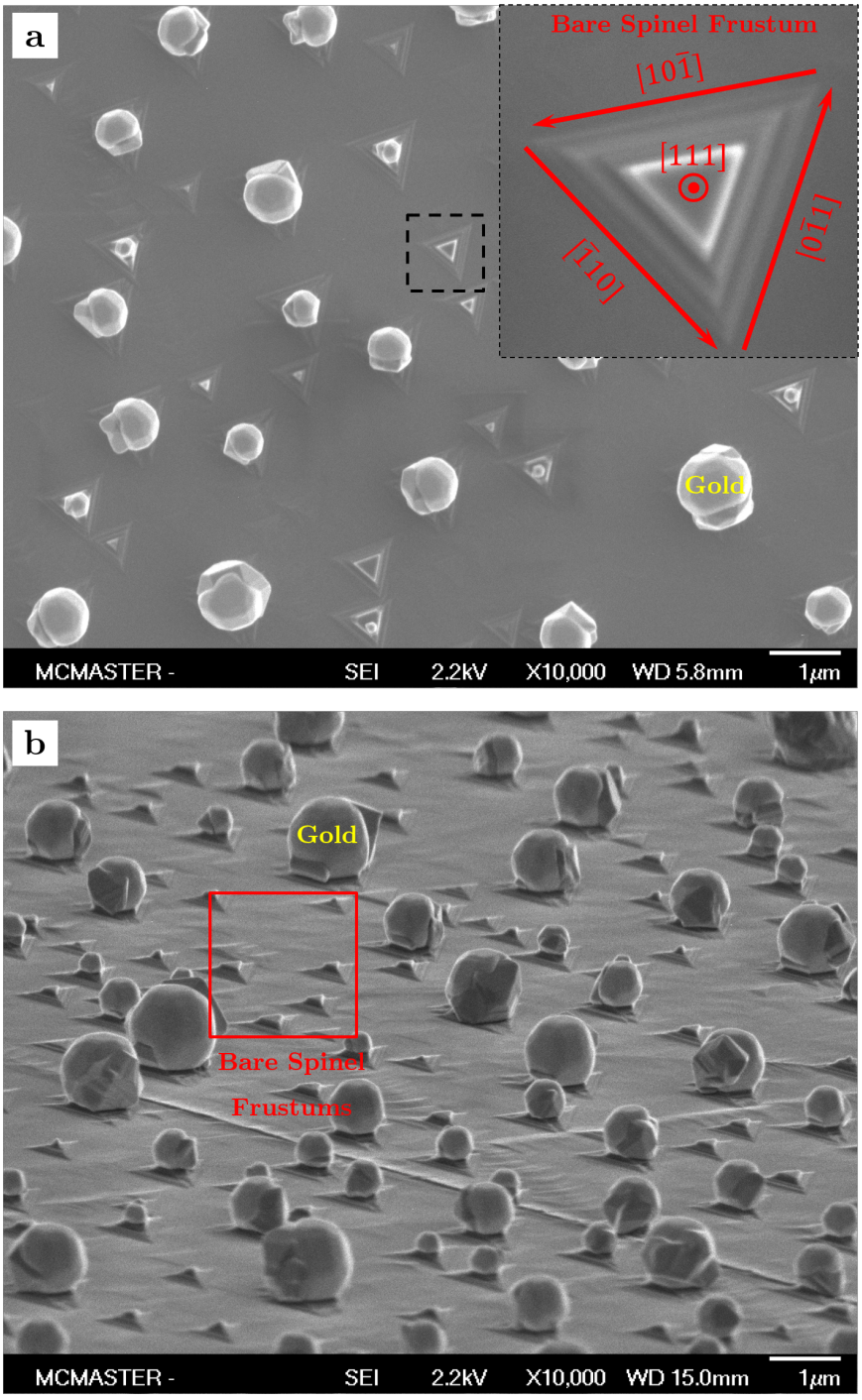


Figure 3.2: (111)-spinel substrate sputter coated with 50 nm of gold and annealed at 1190 ℃ for 4 hours, cooled down to 1050 ℃ and held at that temperature for 4 hours; (a) Top view and (b) 70°-tilted view.

due to significant loss of gold through evaporation. Such structures were also reported by Majdi in case of samples that were heat treated at harsh annealing profiles resulting in complete loss of gold [77]. However, in the case of our sample, due to the higher thickness of initial gold film, some particles have withstood the extreme temperature and duration of heat treatment. These particles are those that have inherited more gold during the formation of liquid gold islands and the process of Ostwald ripening.

One can conclude from these results that the extreme heat treatment temperatures and durations are not inherently detrimental to formation of intricate structures, as suggested by Majdi, but on the contrary, higher temperatures and prolonged durations promote the formation of such structures as long as there is enough gold remaining on spinel to carry on the process. This also underlines the essential role of gold film in any potential mechanism through which the intricate structures are developed.

### 3.2.3 Effect of Rapid Initial Heating on Gold-Spinel Intricate Structures

Based on discussions in Section 1.2.3, 'Wetting and Dewetting Phenomena', high thermal gradient (via rapidly heating the system to high temperatures) may alter the evolution of dewetting process by inducing surfaces disturbances with lower wavelength and higher amplitude that temporally do not allow much diffusion to take place and long-range material displacement to occur. Consequently, it would follow that a much quicker film retraction and formation of smaller (dewetted) islands spreading with more uniformity and in closer spacing to happen.

To demonstrate the effect of initial rapid heating, a sample of 10 nm sputter-coated gold on (111) spinel substrate was inserted into the preheated furnace of 850 ℃ following the normal annealing profile thereafter by ramping up the temperature to 1150 ℃ and holding the sample at that temperature for 2 hours and then cooling it down to 1000 ℃ and holding it there for another 2 hours and then finishing the annealing process with cooling the ample down to room temperature. The sudden introduction of sample from room temperature to 850 ℃ provides a high thermal gradient by rapid equilibration to high temperature without inducing significant thermal shocks in spinel that may cause substrate fracture.

In Figure 3.3, SEM images from a sample annealed based on rapid and normal initial ramp profiles are presented. Images 3.3(a) and 3.3(b) are top and tilted view

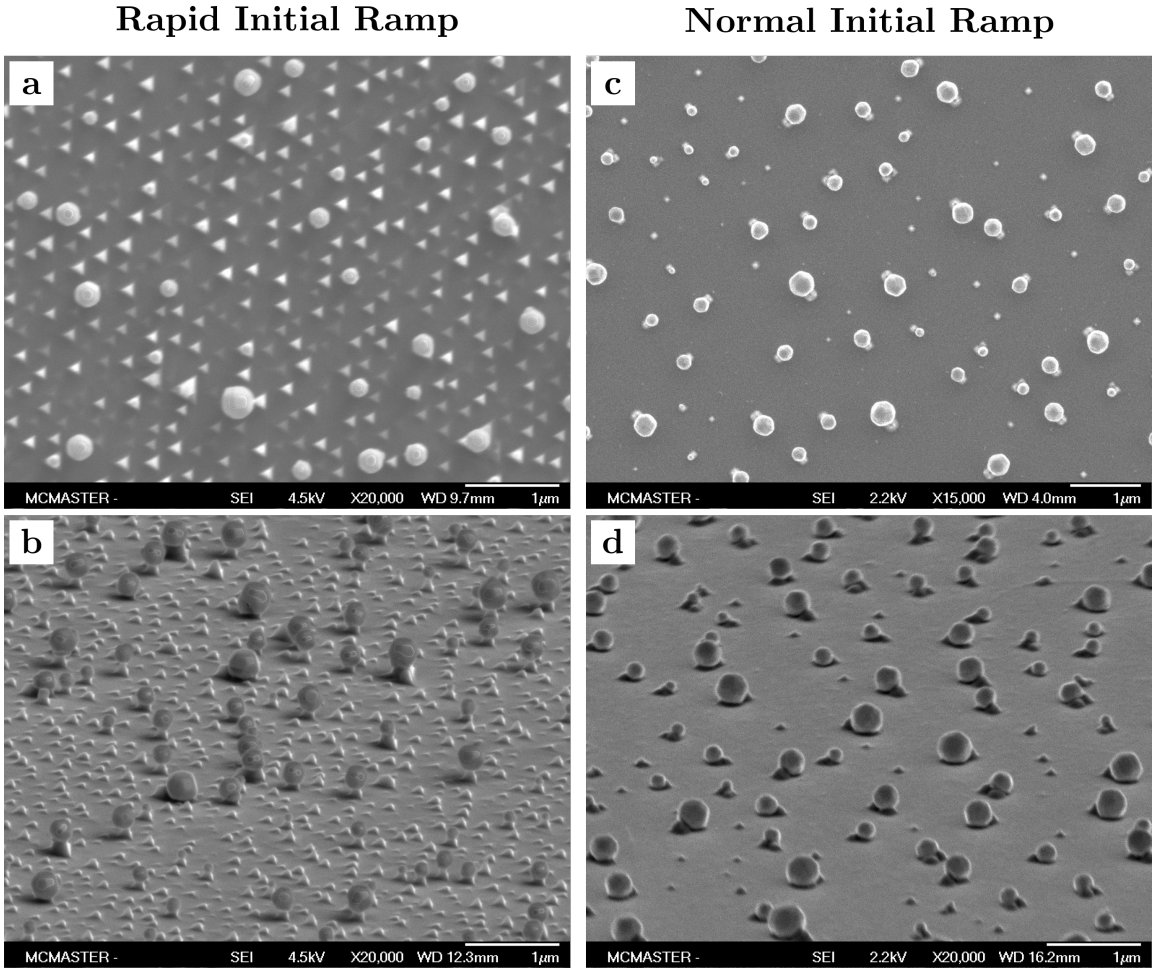


Figure 3.3: (a) & (b) top and 70°-tilted views from (111)-spinel with 10 nm of initial gold film, annealed at 1150 ℃ for 2 hours, cooled down to 1000 ℃ and held at that temperature for 2, starting from 850 ℃ pre-heated furnace (high thermal gradient anneal); (c) & (d) top and 70°-tilted views from (111)-spinel with 10 nm of initial gold film, annealed at 1150 ℃ for 2 hours, cooled down to 1000 ℃ and held at that temperature for 2, starting from room temperature (normal thermal gradient anneal).

images of the sample heat treated as per rapid initial ramping. As a reference, (top and tilted view) images of an identical sample, heat treated as per normal initial ramping, are also presented in images(3.3(c) and 3.3(d)).

The samples are similar in that they both have developed self-assembled intricate structures. The size distribution and the average size of the gold particles also seem to roughly be the same, which suggests that these parameters are not chiefly affected

by heating rate and are more likely to be dependent upon the maximum temperature and the duration of annealing profile. Crystallinity of the gold particles are also much alike as they all seem to be single-crystalline with facets of a equilibrium fcc shape.

The samples are different in that they have drastically distinct surface density of intricate structures. The one annealed according to high thermal gradient profile has developed a high density of spinel self-assembly. The self-assembled spinel structures are mostly in shape of full pyramids but, occasionally, frustums appear to have formed. Some of the spinel self-assembled structures are rather large and tall and frequently capped with large gold particles. Moreover, most of spinel pyramids have no gold on top and overall, the sample is less abundant of gold particles compared to the sample annealed at normal heating rate. So it can be concluded that rapid initial ramp hastens the self-assembly reaction whilst exacerbates the evaporation rate of gold.

The self-assembly of large and tall spinel structures cannot be directly attributed to high thermal gradient from rapid heat treatment however, the surface density of those structures on the substrate is mainly dependent on heating rate which, in resemblance to laser induced dewetting processes, creates a uniform pattern of dewetted metal islands with small spacings that approach the characteristic lengths of spinodal dewetting mechanism. This gives an opportunity to the spinel self-assembly reaction to carry forward on a larger fraction of spinel surface as the activation energy is provided through soaking stages of annealing profile [79].

## 3.3 Effect of Acid Treatment

Acid treatment of the gold-spinel system was primarily devised to bleach the gold particles from samples and examine a clean self-assembled surface of spinel. To this purpose, aqua regia solution, a 1:3 volumetric mixture of nitric and hydrochloric acids, (see Section 1.4.2, 'Physical and Chemical Properties of Gold') was prepared to strip gold particles off the substrate. The etching rate of aqua regia is about 10 $\mu m.min^{-1}$. So, it is expected, in matter of a few seconds, all of gold nanoparticles will be removed from the surface of sample.

Figure 3.4 illustrates SEM images of a (111) spinel sputter-coated with 10 nm of gold, annealed at 1150 ℃ for 32 hours and then 1000 ℃ for 2 hours, and etched with aqua regia for 5 seconds. Aqua regia has successfully dissolved all of gold and bare spinel pedestals from gold-spinel intricate structures are revealed. These pedestals

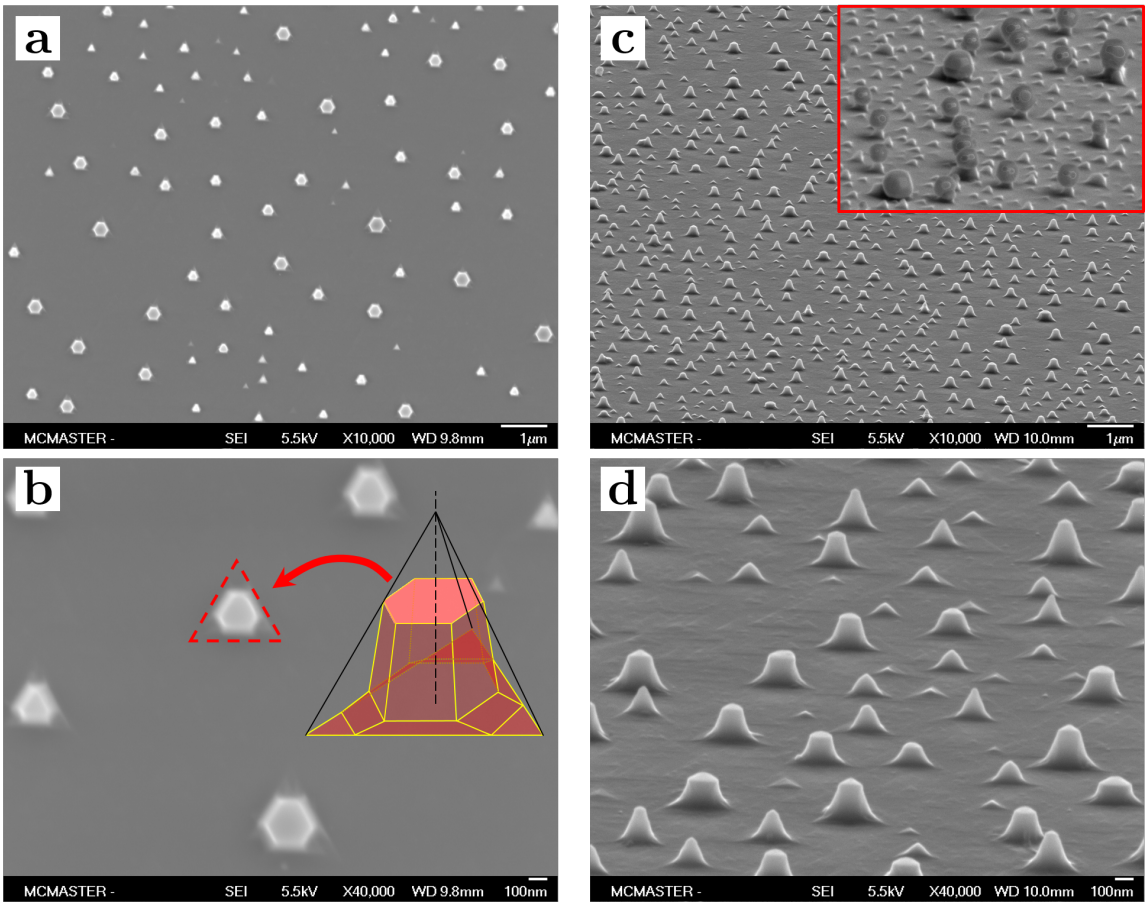


Figure 3.4: (a and b) Top- and (c and d) tilted-view (70°) SEM images from an auqa regia treated sample showing bare spinel pedestals. The inset on upper right corner is a view of sample before etching and shows gold-spinel intricate structures.

consist of a equilateral triangle footprint (mimicking the (111) surface 3-fold symmetry) with frustums of hexagonal base growing out the footprints. The average height of pedestals seem to be equal to side of triangle footprint and in range of 250-300 nm.

Since pedestals are single crystalline and are epitaxially grown from (111) plane of spinel with 3-fold symmetry, it is expected that all exposed surfaces, including top facet and walls, to be (111) planes. In fact, the pedestals can be contained inside a tetrahedron made out of (111) planes (as demonstrated schematically in Figure 3.4) which is the eventual equilibrium shape for these pedestals. Aqua regia etching also revealed that gold particles, most probably, cover some area from the side walls of spinel pedestals as well as top facets of frustums which can be distinguished in tilted-view

SEM images of the sample before and after the etching process.

The effect of aqua regia is not restricted to gold and appear to have also impacted spinel. Following the success of aqua regia treatment in removing gold particles, the process was adapted to recycle spinel substrates for repeated gold dewetting experiments. This should allow to check for dewetting behavior of a second gold layer through which, by comparing the contact angles of gold particles, formation of complexion layer can be verified. It was expected, if the complexion layer forms at the interface of gold and spinel, then dewetting another layer of gold on top of the sample would lead to a different contact angle of gold beads and underlying spinel substrate. Because it is suggested that formation of such layer decreases the surface tensions at adjacent phases, thus, due to higher surface affinity, any gold droplet would spread more on complexion layer than on spinel surface resulting in significantly smaller contact angle.

Accordingly, a (111) spinel substrate was sputter-coated with 10 nm gold, annealed at 1150 ℃ for 2 hours and then at 1000 ℃ for 2 more hours. The sample was then etched by aqua regia solution for 5 seconds. Another layer of sputter-coated gold film of 10 nm thickness applied and then the sample underwent a further round of annealing at 900 ℃ for 2 hours. For the second cycle of heat treatment, a lower temperature is chosen to not degrade any potentially complexion layer formed at the surface. Figure 3.5 represents the SEM images of the sample before and after second round of gold coating and heat treatment.

As seen in the images (a and b) from Figure 3.5, aqua regia treatment has successfully stripped all of gold on the sample and bare spinel pedestals are exposed. Images (c and d) from Figure 3.5 depict the sample after second cycle of gold coating and annealing. In this stage, gold film has been dewetted to highly faceted particles, however, due to moderate temperatures of annealing, the layer has barely dewetted and formed gold islands instead of equilibrium-shaped spherical gold particles. Nevertheless, contact angle of gold islands seems not to be different from the gold particles in intricate structures or from any dewetted gold particles on oxide substrates, for that matter. This is an evidence that either complexion layer has not formed from the beginning or has been destroyed in the process of etching and annealing.

A comparison can be made between the sample shown in Figure 3.5(c) with a another sample that was only coated once with 5 nm of gold and annealed at 900 ℃ for two hours in Figure 3.6. According to the images in this figure, the dewetting

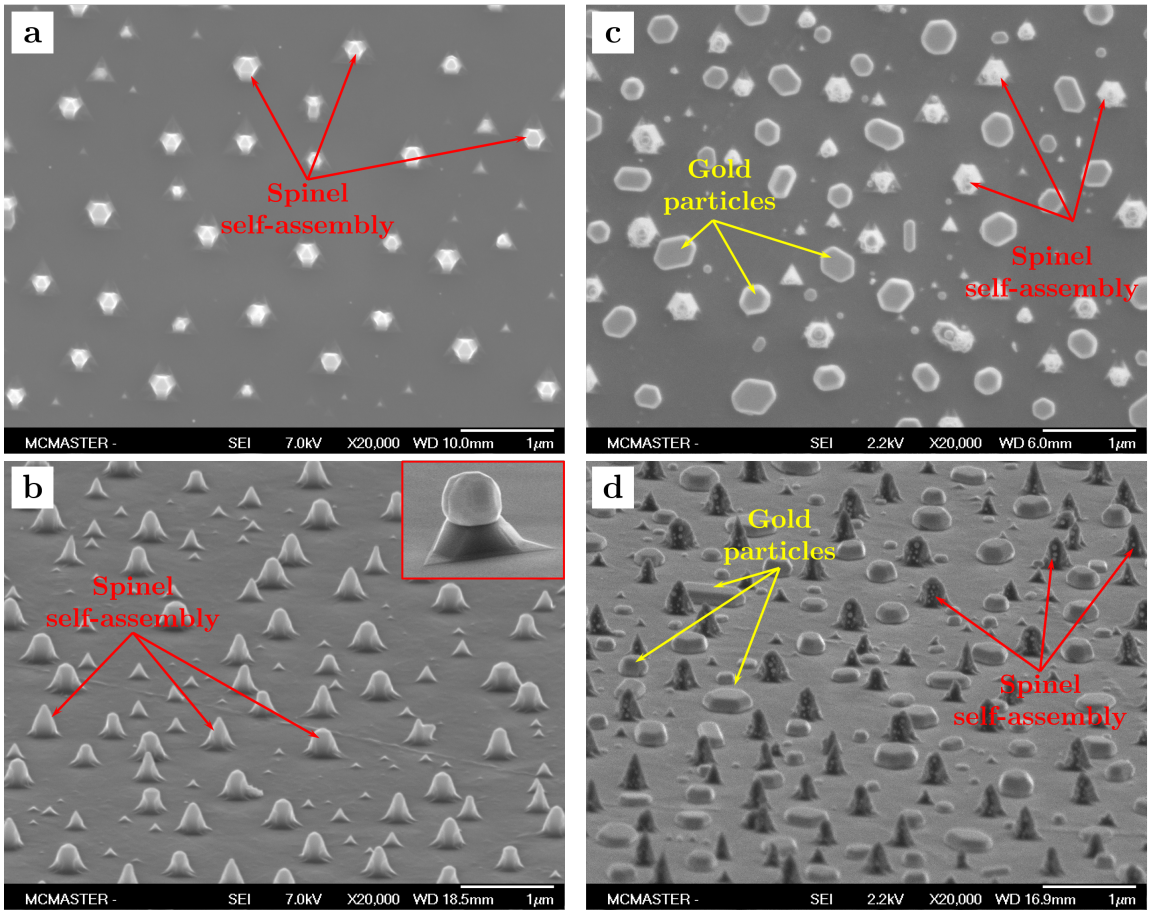


Figure 3.5: Top- and (70°) tilted-view SEM images from an aqua regia treated sample: (a) and (b), before, and (c) and (d), after second round of gold coating and heat treatment. Inset on (b) shows a gold spherical particle on top of spinel pedestal forming an intricate structure and well-resolved contact angle.

characteristics of both sample are the same, except the average size of the particles in image (a)-belonging to the sample coated and annealed twice-are larger than that of image (b)-belonging to the sample coated and annealed once. This can be justified based on the fact that the already grown spinel pedestals in image (a) are so sharp that they have punctured and tore the second gold coating during annealing thus, altering a natural dewetting process and the size of resultant gold islands according to the separation of pedestals. Whereas, the gold film on the other sample has undergone uninterrupted dewetting process driven solely by thermal annealing.

A more careful observation on Figure 3.5(d) reveals existence of very small particles

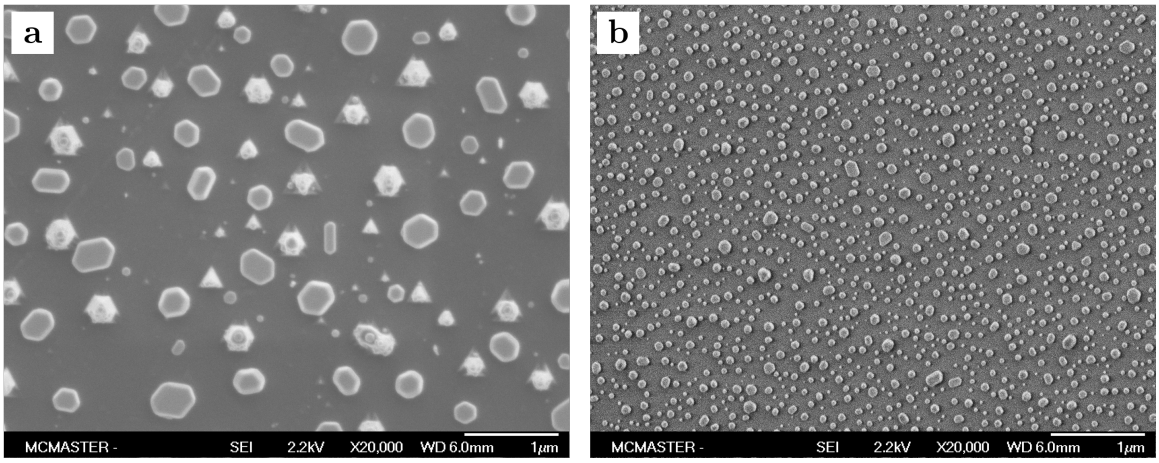


Figure 3.6: (a) SEM image of a (111) spinel sample coated with 5 nm of gold and annealed at 900 ℃ for 2 hours, and (b) SEM image of an aqua regia treated sample after second round of gold coating and heat treatment, identical to that of (a).

of gold (<50 nm) on the walls of spinel pedestals. Because of steep inclination, only very small particles can be equilibrated on the walls. It is also noticeable that the pedestals stand somewhat taller after second round of coating and annealing. This may be rationalized by accounting for the effect of aqua regia on spinel. The strong acid tends to break chemical bonds of surface atoms which might facilitate the self-assembly rate of spinel during heat treatment process. Although the effect of aqua regia, specifically, and the effect of nitric and hydrochloric acids, generally, have not been studied on spinel, there are reports of chemically polishing spinel's surfaces by application of sulfuric-phosphoric acid mixtures and pyrophosphoric acid at elevated temperatures [80, 81].

Given the harsh effects of aqua regia on both gold and spinel, it is perhaps unlikely that any complexion layer would survive the etching process. Therefore, another method has been devised to prevent the damage of chemical treatment on complexion layer and preserve it for further thermal processing. The following section describes another effort to realize this goal, this time through mechanical removal of initial gold particle(s).

## 3.4 Melting Bulk Gold on Spinel

To further examine the hypothesis of formation of gold-spinel complexion layer, a series of experiments designed and conducted with the aim of creating a large surface area of the complexion layer on the spinel with melting thin foil of gold (bulk) on spinel according to different annealing patterns. This time, removing gold through a mechanical route is possible due to macroscopic dimensions of resultant gold sphere after preliminary annealing process.

To realize this idea, a piece of gold foil with approximate thickness of 80 $\mu m$ was set on top of a (111) spinel and the system annealed at 1050 ℃ for 3 hours and then at 1175 ℃ for 5 more hours. At this stage, a large sphere of gold (along with several smaller ones) had formed on substrate that then imaged for more details via SEM. Next, the solid gold sphere removed from the surface (with physical force) to expose the complexion layer and a sputter-coated layer of gold (10 nm) deposited on the same sample and annealed according to a normal heat treatment profile used for dewetting thin films (1150 ℃ for 2 hours + 1000 ℃ for 2 hours). To avoid any interference from contaminants, a gold conductive coating applied on the samples for SEM imaging. Figure 3.7 shows the SEM images of first gold sphere(s) and the features formed at its vicinity after melting the gold foil.

Figure 3.8 shows the SEM images of dewetted second gold layer and formation of gold-spinel intricate structures inside and outside of the gold sphere footprint. Images show the formation of intricate structures on the surface with no apparent difference. Average size, surface density, and most importantly, the contact angle of the gold particles on spinel necking structures seem to be the same both inside and outside the gold sphere footprint. Therefore, all observations indicate either absence of complexion layer or destruction of such layer during gold removal and\or during second heat treatment process.

This experiment also repeated with another samples in which the second heat treatment profile to dewet the gold thin film was chosen to be milder in order to ensure the complexion layer is not damaged because of harsh annealing conditions. In this stage, if the dewetted particles from second gold layer still developed the same intricate structures with the same contact angles (between gold and spinel necking), then it may be assumed, confidently, that the complexion layer does not form or it is destroyed by removing the gold sphere by physical force. The use of physical force

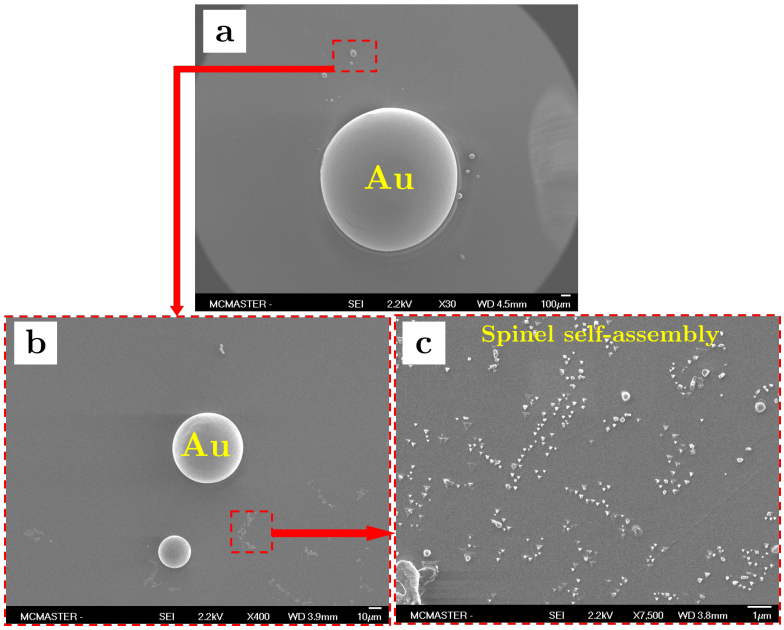


Figure 3.7: Formation of (a) macroscopic gold sphere, (b) several other '*satellite*' gold particles, and (c) spinel self-assembly features after melting the gold foil on top of spinel substrate.

was preferred over chemical routes of removing gold as the acids dissolving gold have very degrading impact on spinel as well (As explained in previous section). Thus, any delicate structure such as a complexion layer would be surely damaged as a result of such treatments.

To prepare the next sample, a piece of gold foil of the same thickness as previous experiment was melted on top of (111) spinel according to the annealing profile that used for melting gold foil in previous case. The solid gold sphere was again removed by means of physical force. 5 nm thick layer of gold film was sputter-coated on the same sample and annealed at 900 ℃ for 2 hours. Figure 3.9 shows the SEM images of resultant particles formed on the substrate.

Once again, the overall appearance of the structures formed, inside and outside the gold sphere rim, look the same. however, in this sample no spinel necking structures have formed underneath the gold particles due to low annealing temperatures. The average size of the particles also seem to be finer due to lower thickness of the initial gold thin film and lower heating duration. Those particles inside the gold sphere rim appear to be somewhat smaller in size, although, other SEM images from the

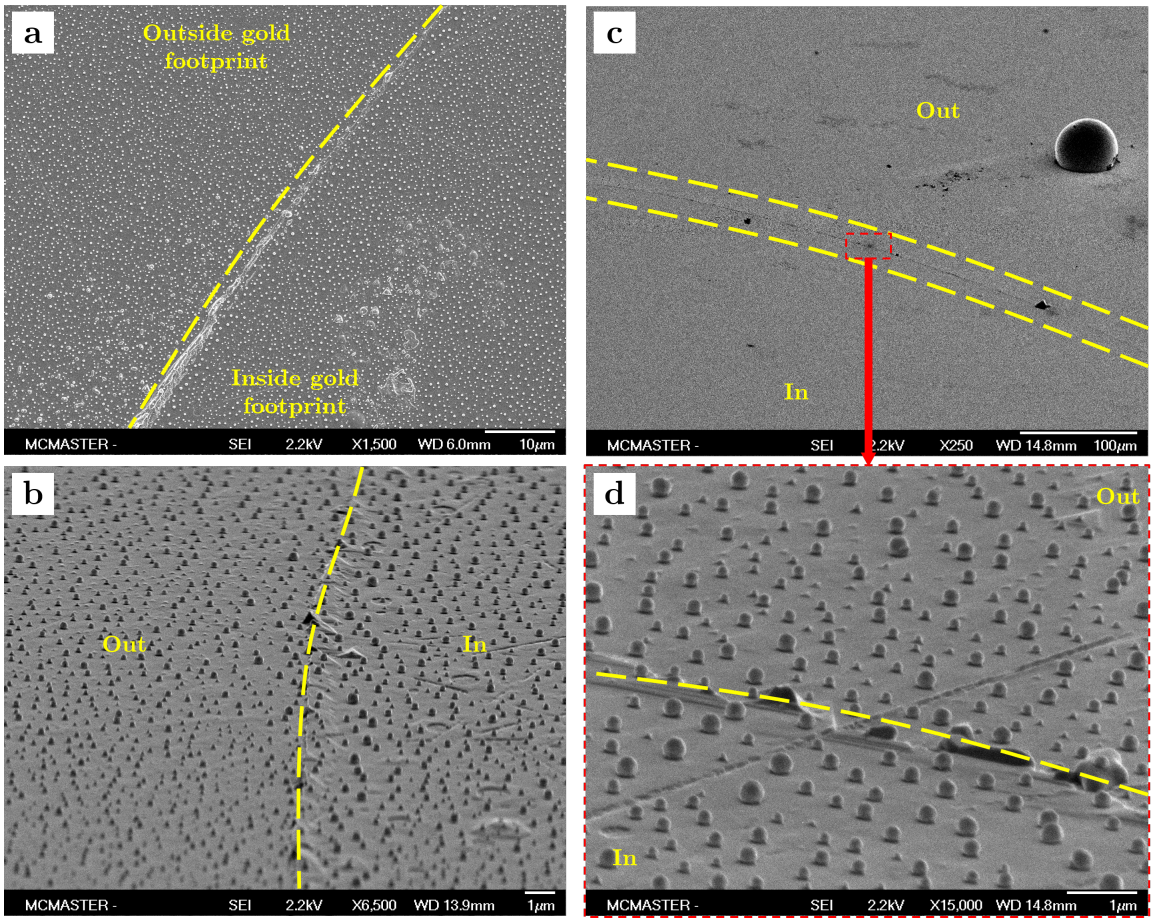


Figure 3.8: (a) Top- and (b,c, and d) tilted-view (70°) SEM images from final state of the sample after dewetting a second layer of gold on spinel subsequent to removal of gold sphere.

periphery of the rim do not make same impression. Although due to very small size, the edges of gold particles appear dim, but all gold particles, in and out of the footprint, demonstrate similar curved surfaces with the same contact angles which essentially can be interpreted as a normal gold-spinel interface with no indication of complexion layer.

## 3.5 Dewetting Non-Gold Metallic Films on Spinel

Formation of intricate structures has only reported in gold-spinel system and despite the efforts to investigate all aspects of this system, there is no evidence to restrict such

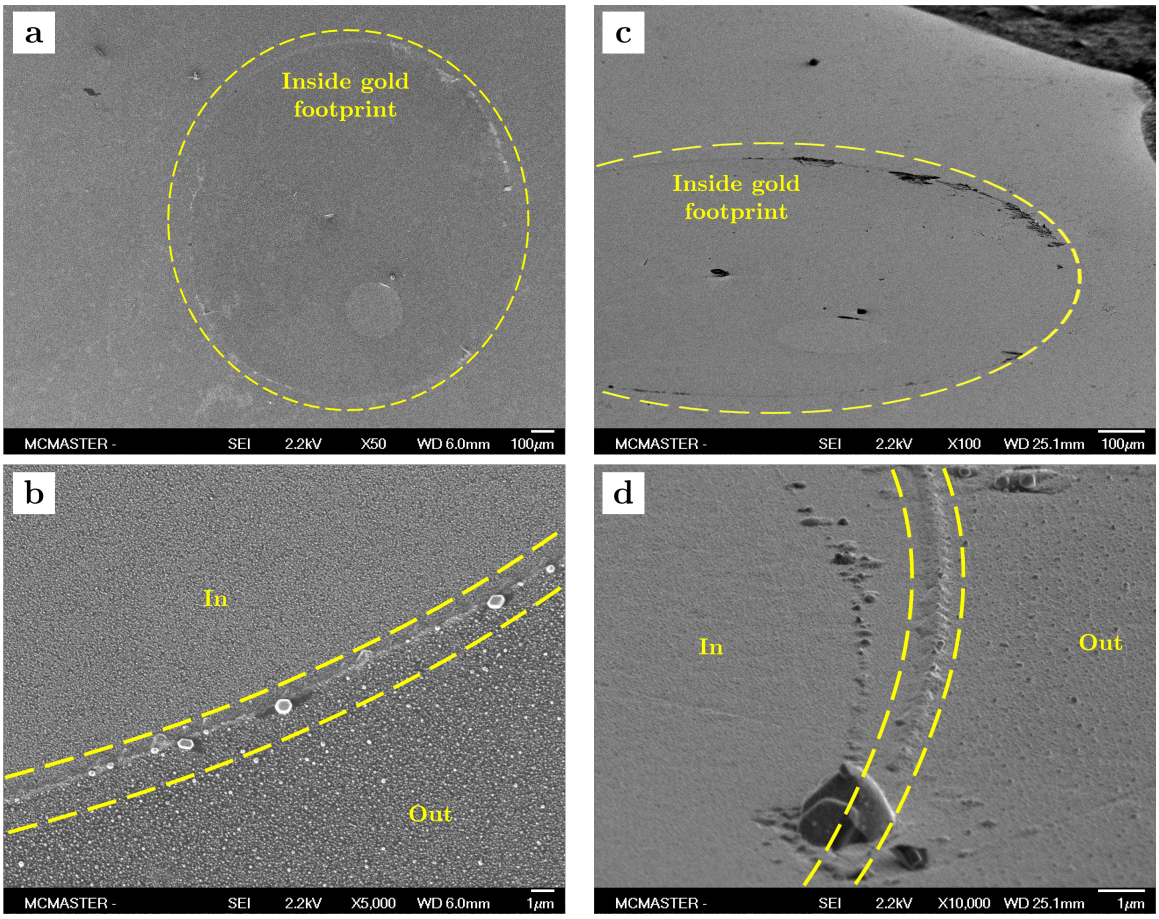


Figure 3.9: (a and b) Top- and (c and d) tilted-view (70°) SEM images from final state of the sample after dewetting a second layer of gold on spinel subsequent to removal of gold sphere.

behavior (formation of intricate structures) exclusively to gold-spinel. Therefore, it is interesting to test uniqueness of this behavior by using other metallic films, which might also help to understand more about the chemistry of such systems.

To examine whether dewetting other metallic films may yield to formation of intricate structures, different samples with platinum (Pt) and copper (Cu) coatings were prepared. The choice of Pt and Cu can be rationalized based on several reasons including: (i) Their high melting point that lies higher than or within the same range as gold's melting point and the temperature of spinel's surface reconstruction ($T_m^{Pt} = 1768$ ℃, $T_m^{Cu} = 1085$ ℃). (ii) The catalytic activity, as described in Section 1.4.4, '*Catalytic Activity*', which is reported for both Pt and Cu. (iii) Convenience of

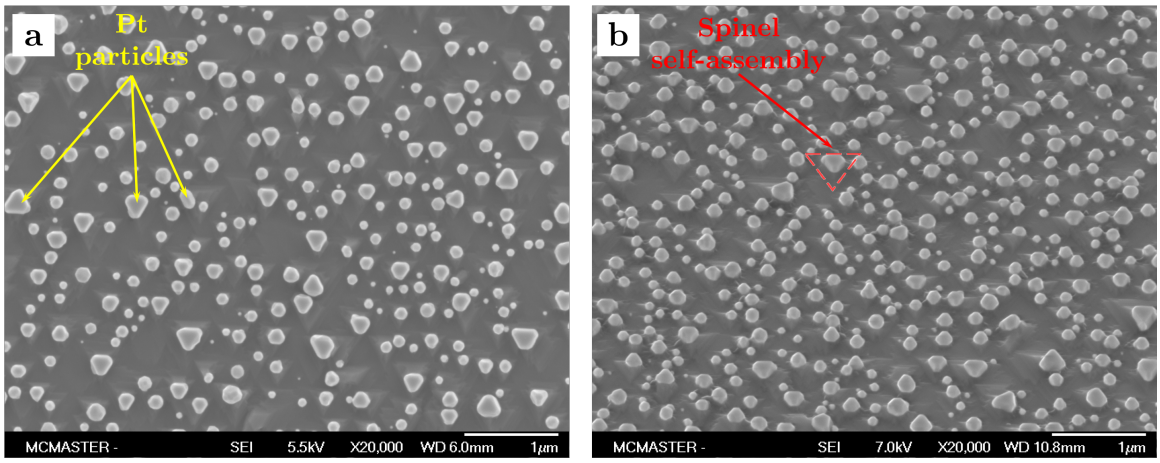


Figure 3.10: SEM image of (111) spinel with Pt film dewetted atop: (a) Top-view and (b) (45°) tilted-view.

applying thin films of both metal via sputtering instruments without the need for special settings such as controlled depositing atmosphere or utilization of magnetron-assisted systems.

A (111) spinel substrate was sputter-coated with 10 nm of Pt and heat treated at 1190 ℃ for 4 hours and then at 1050 ℃ for 4 hours. As the melting point of Pt is rather high and beyond the reach of our furnace (if not accounting for size effect), the highest possible temperature for a prolong annealing duration was chosen to make sure the Pt film completely dewets and has enough atomic mobility for interaction with underlying spinel substrate. Figure 3.10 represents the SEM (top- and tilted-view) images of the thus-prepared sample.

SEM images illustrate formation of fine Pt particles (compared to particles resulted from gold film of same thickness) of average diameter of $\sim 80$ nm. The particles are well-faceted and appear to have a triangular shape. Although, not fully embodying equilibrium shape of an fcc crystal, the particles have adapted 3-fold symmetry of underlying substrate and appear to be enclosed mostly in (111) planes which bear the identical symmetry with substrate surface and the lowest surface tension in Pt crystal [82, 83]. Therefore, particles are epitaxially grown against the (111) surface of spinel. Given that the lattice constant of Pt is very close to that of gold, ($a_{Au} = 4.06\text{Å}, a_{Pt} = 3.91\text{Å}$), a similar heteroepitaxial relationship with very small lattice mismatch ($a_{spinel} \cong 2a_{Pt}$) is also expected between Pt and spinel substrate.

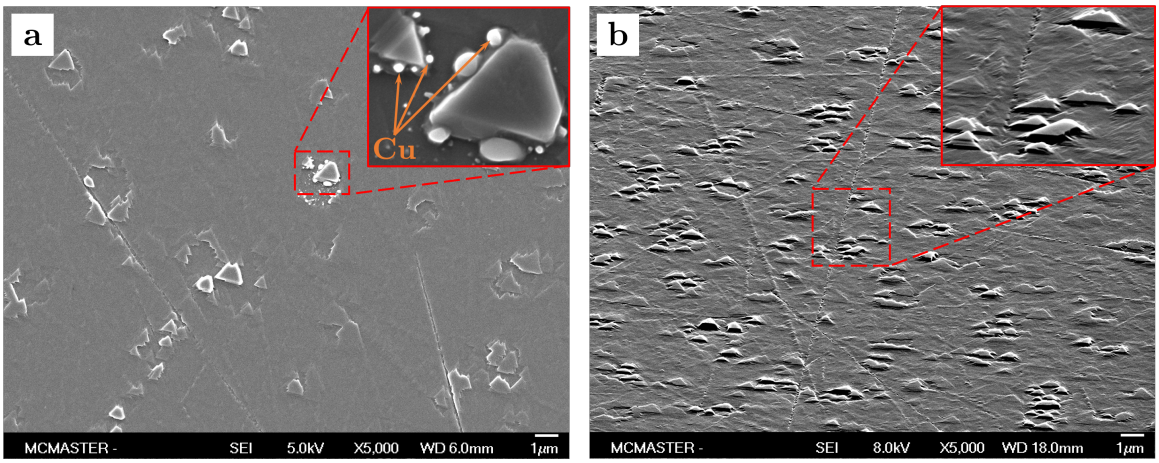


Figure 3.11: SEM image of (111) spinel with Cu film dewetted atop: (a) Top-view and (b) (70°) tilted-view. The insets are higher magnifications of the marked features.

SEM images also reveal formation of intricate platinum-spinel structures with spinel self-assembly underneath the Pt particles. These self-assembled spinel structure have the same frustum shape of spinel necking structures in gold-spinel system, but have relatively shorter heights. The intricate structures also appear to have partly merged into each other which is due to very close spacing of Pt particles.

This experiment was further repeated with copper (Cu) coating. A (111) spinel substrate was sputter-coated with 50 nm of Cu and heat treated at 1190 ℃ for 4 hours and then at 1050 ℃ for another 4 hours. To match the dewetting conditions with previous experiment, a higher thickness of Cu used to compensate the evaporation rate of film for the long annealing duration. Figure 3.11 illustrates the SEM (top- and tilted-view) images of this sample.

As seen in Figure 3.11, despite depositing a thicker film, almost all of Cu has evaporated and there are no signs of Cu particles except occasionally in the periphery of spinel frustums which appear brighter than spinel. However, existence of spinel self-assembly indicates that, at some point, intricate structures of copper-spinel have formed but any Cu particle on top of spinel frustums has vanished due to high evaporation rate. It is also possible that some of copper film has diffused into spinel crystal structure and/or substituted spinel cations due its smaller atomic radius and higher reactivity compared with gold and platinum.

The spinel self-assembled structures in this sample are also quite distinct from others observed in case of platinum and gold. In this sample, spinel has self-assembled

in patches of several frustums in some area and these patches are then spaced as the individual frustums had in Au and Pt samples. Moreover, the self-assembled structures stand shorter (as compared with Au and Pt samples) and have irregular edges and corners. Another distinct feature of the self-assembled structures in this sample is they all have flat tops and none of them have pyramidal shapes with sharp vertices. One reason to explain the aforementioned features in self-assembled structures in this sample could be that with evaporation of all of copper film, spinel self-assembly is stopped and then reversed by immersing back to the hosting substrate to reduce the surface area and surface tension, accordingly.

By putting the results of these two experiments (Pt and Cu) together and comparing them with the obtained results from gold experiments, it can be concluded that spinel self-assembly due to dewetting a metallic thin film is more prevalent than it was thought before. Gold, platinum, and copper are only the three candidates studied in this thesis and certainly a comprehensive study must include a broader range of metals to fully reveal the extent of self-assembly phenomenon. Although, topographical attributes of self-assembled spinel structures such as height, lateral size, and shape are different in each case, the formation of triangular protrusions mimicking 3-fold symmetry of the underlying substrate is common in all three cases.

Furthermore, these results are more indicative of a chemical cause for spinel's growth rather than the epitaxial or crystallographic relationships that were suggested by previous studies. Therefore, deeper analysis into the interface of metal-spinel intricate structures is essential for better insight as to how self-assembly of spinel is formed due to dewetting an overlaid thin metallic film. One way to achieve this is atomic analysis of the interface. The following section discusses the results of such analysis in the especial case of gold-spinel.

## 3.6 Investigation Into Interface of Gold-Spinel

As it seems that the chemical and thermodynamical factors are principally important in growth of self-assembled spinel structures, our focus has been fixated on the interface of gold and spinel in this section with the main objective of identifying the chemical composition of interface complexion. Previously, Majdi and Zhu *et. al.* [53, 84] had utilized high resolution STEM analysis in HAADF mode to unravel the formation of a bilayer complexion phase consisting of alternating gold and oxygen atoms that are

accommodated to (111) planes of underlying spinel and gold on top . This alternating gold-oxygen coordination suggests an abrupt change in chemical composition from gold through interface and into spinel. The complexion bilayer should then possess almost 50 % of each of oxygen and gold atom.

To analyze the chemical composition of the interface, APT analysis was conducted on a sample of gold-spinel. The sample was prepared by sputter-coating 50 nm of gold on (111) spinel and annealing at 1190 ℃ for 4 hours ad then at 1050 ℃ for another 4 hours. To stimulate formation of taller gold-spinel structures with higher surface density, annealing started from 850 ℃ rather than room temperature as the procedure explained in Section 3.2.3, "Effect of Rapid Initial Heating on Gold-Spinel Intricate Structures", for inducing high thermal gradient.

FIB technique was utilized to produce specimens for the APT analysis. A region of interest selected on the sample with 5 intricate structures located approximately on a straight line, each being at least 2 $\mu m$ apart. This region then coated with W to create a solid block in order to protect it from Ga ion bombardment during milling and lifting. The block was then carved out of sample and subsequently positioned on Si posts such that each intricate structure was centered on a post and the rest of the block was cut and repositioned onto other posts. The process repeated until all 5 intricate structures were located on a post. Then annular milling was utilized to shape the needle-like specimens required for APT analysis. The tip radius of each specimen was kept within the range of 50-60 nm. Finally, Cr coating was applied on specimens to reduce chance of failure. Figure 3.12 presents the step-by-step process of FIB preparation of the APT specimen.

Thus-prepared specimens were then taken to be coated with chromium in a sputter-coating system and then were introduced into APT analysis chamber. Instrument setups and specifications of the procedure are explained in Section 2.4.5, "Atom Probe Tomography". Figure 3.13 shows the mass spectrum of the sample with the peaks indexed to appropriate species according to Table 3.1.

Using Table 3.1 (ion index table), all elemental components of spinel as well as gold were detected in the mass spectrum. Complex ions of these elements were also detected which appear on the mass spectrum as a result of laser ablation and creation of a laser plume consist of various species in different sizes. Sometimes, ions also lump together as they fly towards the detector as result of collision in electrostatic field. There are also some other elements like Pt, Ga, N, H, and He that are detected. Pt

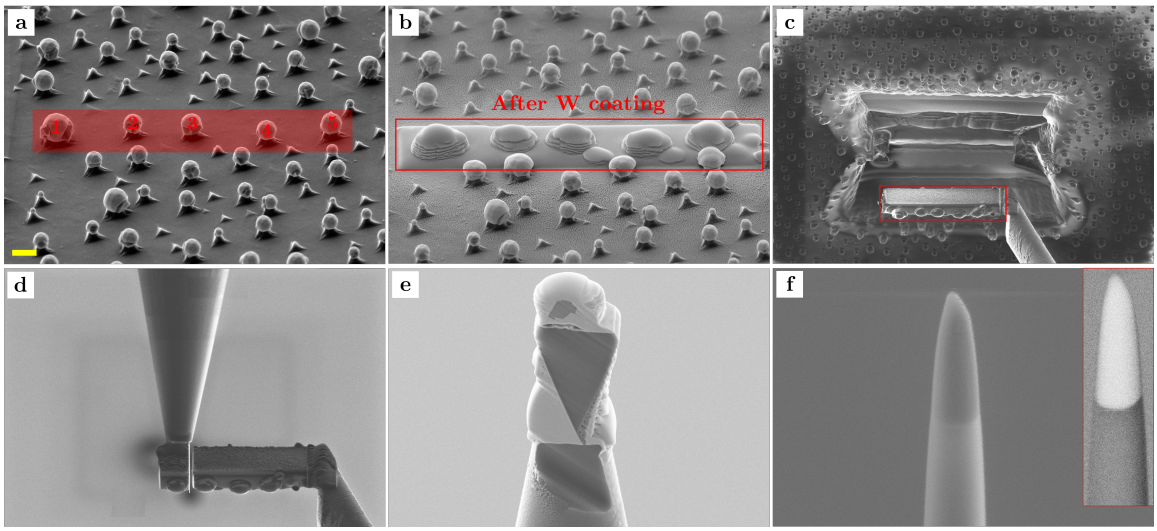


Figure 3.12: (a-f) FIB images of successive steps of preparation of ATP specimens. The yellow scale bar indicates 1 $\mu m$ on image (a). The tip diameter of specimen in image (f) is 60 nm.

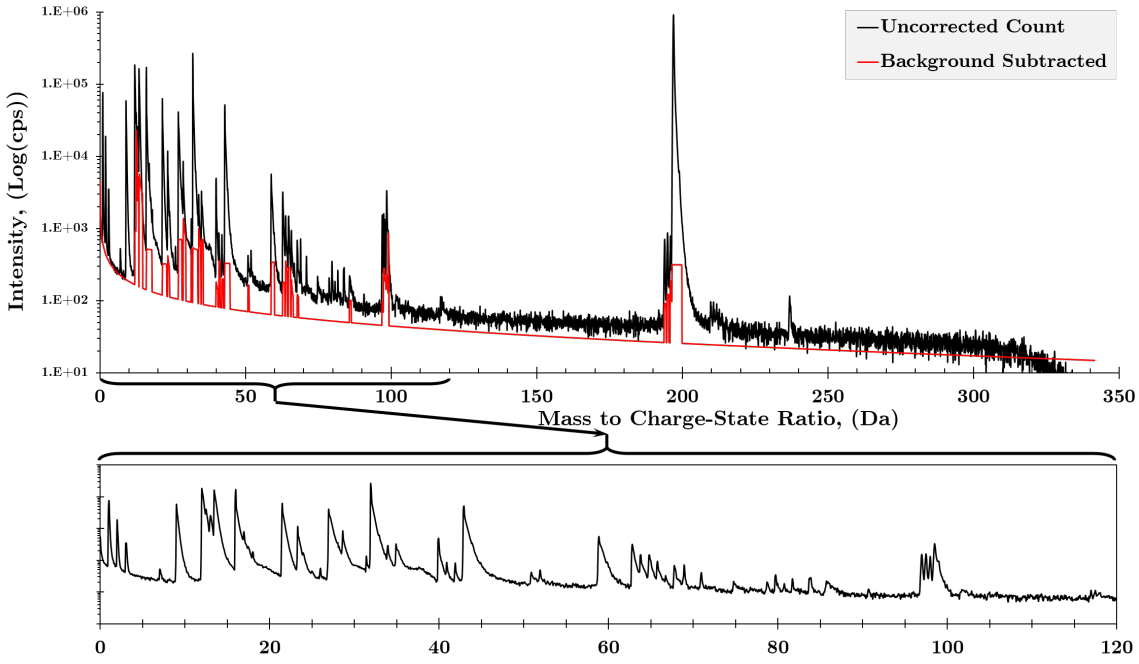


Figure 3.13: Mass spectrum of the APT sample. (Red line is a software estimate of the spectrum with background subtracted.)

comes from the conductive coating applied to prepare the sample for FIB operation. Ga also comes from the FIB environment as some of the FIB ion beam being implanted inside the sample. However, neither Pt nor Ga did appear in very early stages of field evaporation therefore they were discarded for reconstruction purpose as they would appear in outermost layers. N, H, Ar, and He are also ubiquitous impurities which exist in APT chamber which get ionized in the electrostatic field and appear in the mass spectrum. There is however, one impurity that belongs to the sample itself and that is copper which appears to be mostly accumulated at the interface.

Table 3.1: Ion-indexed peaks of mass spectrum.

| Species | Charge-state | Peak range (Da) | Species | Charge-state | Peak range (Da) |
|---|---|---|---|---|---|
| O | (+1) | 15.95-18.16 | Cu | (+1) (2 isotopes) | 64.71-65.48 |
| Au | (+1) | 196.35-199.79 | | | 62.73-63.47 |
| | (+2) | 98.29-98.89 | | (+2) | 31.31-31.51 |
| Al | (+3) | 8.97-10.32 | Pt | (+1) (3 isotopes) | 193.69-194.37 |
| | (+2) | 13.47-14.67 | | | 194.67-195.32 |
| | (+1) | 26.93-28.12 | | | 195.75-196.26 |
| Mg | (+2) (3 isotopes) | 11.97-12.45 | | (+2) (4 isotopes) | 98.93-99.16 |
| | | 12.45-12.87 | | | 96.82-97.27 |
| | | 12.97-13.32 | | | 97.34-97.79 |
| MgO | (+1) (3 isotopes) | 39.83-40.52 | | | 97.83-98.25 |
| | | 40.86-41.24 | N | (+2) | 6.99-7.06 |
| | | 41.84-42.36 | $AlO_2$ | (+1) | 58.79-59.91 |
| AlO | (+1) | 42.81-44.63 | $Al_2O_3$ | (+2) | 50.81-51.21 |
| | (+2) | 21.44-22.93 | AuAr | (+1) | 236.57-237.35 |
| $O_2$ | (+1) (2 isotopes) | 31.87-3359 | H | (+1) | 1.00-1.45 |
| | | 33.87-34.64 | He | (+2) | 2.00-2.32 |
| $Al_2O$ | (+3) | 23.26-23.91 | Ga | (+1) (2 isotopes) | 68.79-69.14 |
| | (+2) | 34.87-35.47 | | | 70.84-71.14 |
| $Al_2O_2$ | (+3) | 28.59-29.49 | | | |
| | (+1) | 85.65-86.27 | | | |
| $Mg_2O$ | (+1) (3 isotopes) | 63.72-64.33 | | | |
| | | 65.67-66.35 | | | |
| | | 67.70-68.18 | | | |

After identifying all species from the mass spectrum as accurately as possible, reconstruction was carried out (as described in 2.4.5, "Atom Probe Tomography") to recreate elemental composition of the sample in 3-D. Figure 3.14 shows the 3-D reconstruction of the sample.

As Figure 3.14 shows, Gold and spinel appear to have a sharp interface with minimal intermix expected as result of different evaporation behavior of the two in APT. It should be noted that the reconstructed shape is only a fraction of the size of specimen produced by FIB as the small detection rate of APT only allows the ions that lie close to the specimen axis to be detected. Therefore, it is can be said that the reconstructed sample represent an inner core of the field evaporated specimen.

To better demonstrate the distribution of copper contamination, a reconstructions of only copper ions and copper isosurface of 1 Wt% inside diluted gold and spinel were generated which are illustrated in Figure 3.15.

As can be seen from Figure 3.15, copper is mostly concentrated at the interface, but it is also detected inside gold and spinel crystals with surprisingly more concentration inside spinel. Since spinel substrates are single crystalline $MgAl_2O_4$, any contamination such copper impurities, even in trace amounts, would drastically affect substrates' physical appearance such as color and transparency, which should be visually detectable. Thus, spinel substrates themselves cannot be the source of copper contamination. This means that a copper contamination can only be introduced from the gold film during sputtering or annealing. The copper inside the gold film has then diffused into the spinel substrate in the course of heat treatment.

To better illustrate the copper concentration along the specimen axis (z-axis), a 1-D concentration profile was created across the interface showing concentration curves of Au, O, Al, Mg, and Cu as a function of distance. The graph of profile is shown in Figure 3.16.

As can be seen from Figure 3.16, all elements, except copper, demonstrate a sigmoid distribution. As a result, a line along 50 % gold assumed as the virtual interface of gold and spinel. A distance of roughly 1.5 nm from each side of the line may also be assumed to be the thickness of interface containing an area between 10 and 90 % gold. Copper, on the other hand, has a Gaussian distribution with maximum peak of 4 % inside the gold very close to the presumptive interface line. Beyond that, as moving further towards gold and spinel, concentration of copper drops dramatically.

The distribution lines of gold and spinel components are smooth and no sudden

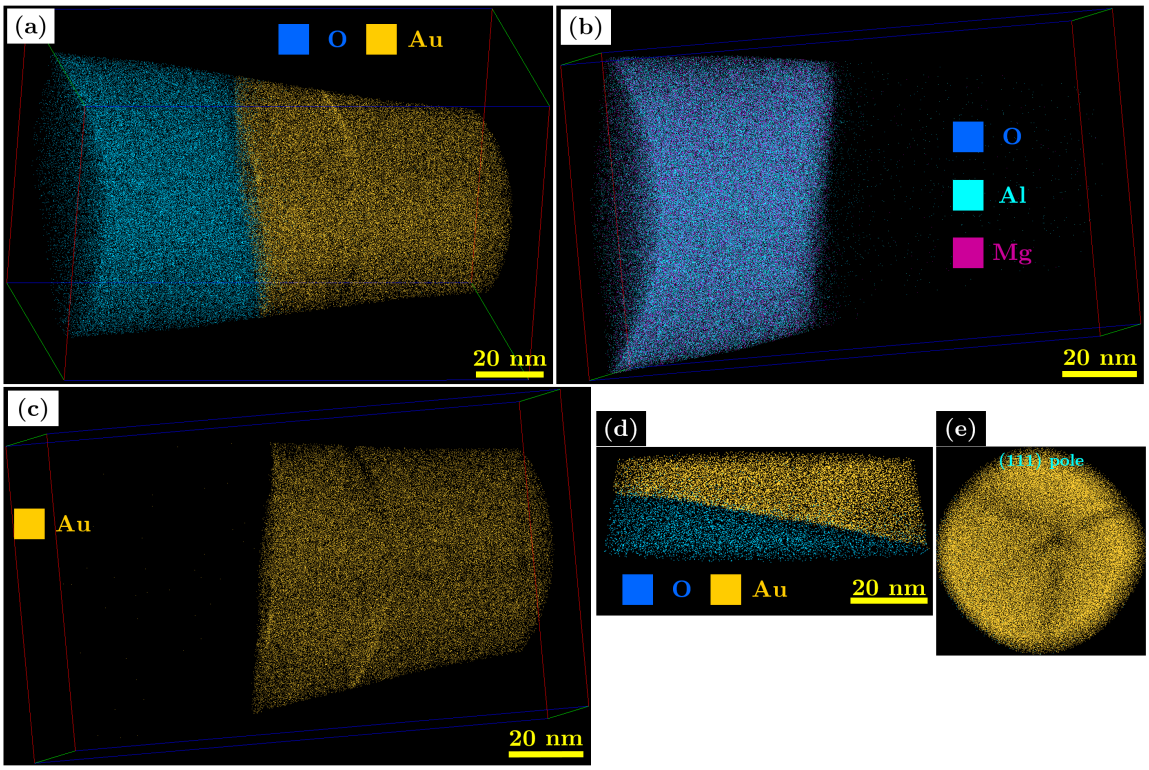


Figure 3.14: (a) Full reconstruction showing only O and Au for the sake of clarity; (b) Spinel reconstruction; (c) Gold reconstruction; (d) Front view from gold-spinel interface; and (e) (111) pole figure of gold crystal perpendicular to spinel surface.

jump can be observed in the concentration curve at the interface. This indicates a chemically sharp interface boundary between gold and spinel, which does not appear to support the hypothesis of Au-O bilayer complexion. If such complexion layer existed, some kind of disturbance in gold concentration profile at around 50 % of gold profile should have been detected.

Based on APT chemical analysis, it cannot be decisively concluded that a complexion layer exists in gold-spinel interface. Moreover, accumulated presence of Cu contaminant at the interface casts doubt on any speculation about formation of complexion bilayer at the interface. Since chemical sensitivity and resolution of APT analysis is much superior to that of EELS, it is highly unlikely to successfully resolve such quantities of contamination in STEM-based EELS analysis. Therefore, conclusions made by Majdi and Zhu cannot be evaluated confidently, as all samples produced for those studies had utilized sputter-coating method to deposit gold films. However, it is still interesting to

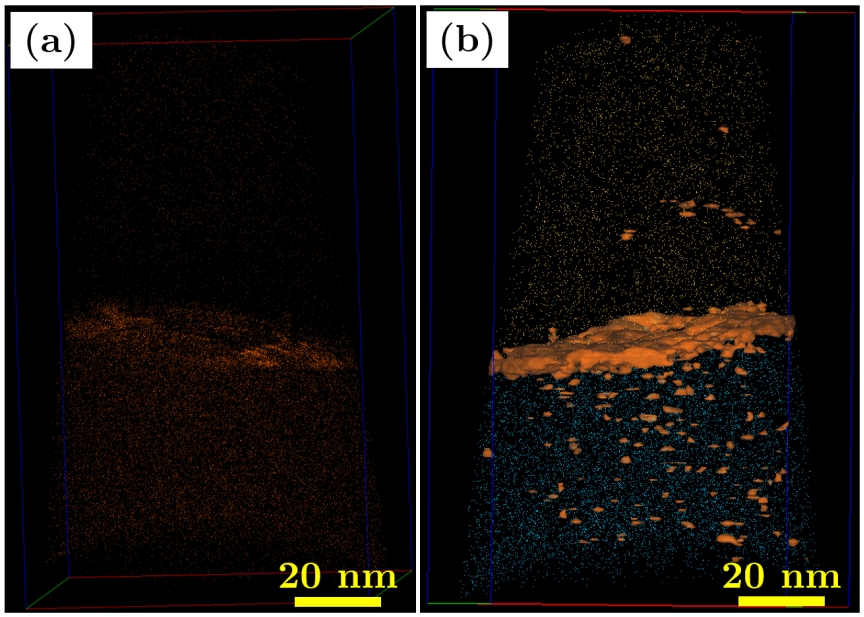


Figure 3.15: (a) Copper reconstruction showing its distribution throughout spinel and gold and at interface; (b) 1 Wt% isosurfaced copper ions accentuating its concentration.

be able to reproduce the visual (crystallographic) features of the complexion layer at interface in STEM analysis. For this purpose, HAADF mode STEM conducted on the specimen created from the same sample used for APT analysis.

Once again, FIB system utilized to cut and lift off a region of interest on the sample where there are 4 intricate structures aligned on a line. By applying W coating a solid block formed which was then carved and lifted off from the substrate and welded to an appropriate TEM grid made out of molybdenum. Eventually, the specimen thinned down to thickness of less than 100 nm by milling away material from both sides of the block by low energy milling. Figure 3.17 presents the step-by-step process of FIB preparation of STEM specimen.

The specimens were then analyzed with high resolution STEM in HAADF mode and the EELS spectra of the sample were collected simultaneously. Figure 3.18 represents the atomic resolution STEM images of the sample. The cross-section of the intricate structure shows a gold particle sitting on top of spinel necking. There are two other areas, appeared in gray contrast, at each side of gold that EELS analysis determined to be copper (II) oxide phases.

The boundary between gold and spinel has been atomically resolved in image 3.18(d)

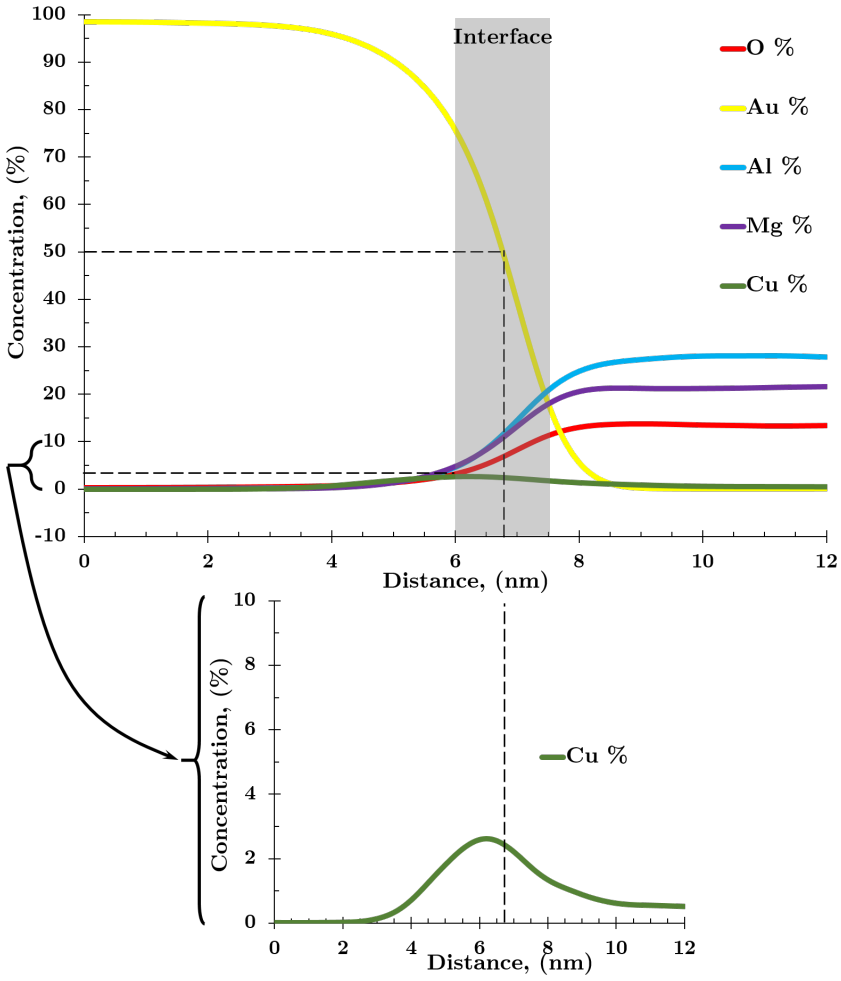


Figure 3.16: Concentration profile of Au, O, Al, Mg, and Cu across interface.

which shows a clear atomically harp layer between gold and spinel with no inter-diffusion between gold and spinel. There is however a row of gold atoms, shown with red arrow in image 3.18(d), in which the gold atoms may seem to have the characteristic arrangement of a complexion layer as described by Majdi and Zhu. But this cannot be satisfactorily justified as an interface complexion since a careful observation reveals that the gold atoms in that layer follow the line of gold atoms in their respective crystallographic plane, as indicated in the image by red dotted-lines. Additionally, if the layer was in fact an interface complexion, then it should have extended uniformly all across the boundary and should not be disrupted.

The existence of this row of gold atoms may be a result of undulations of ion beam

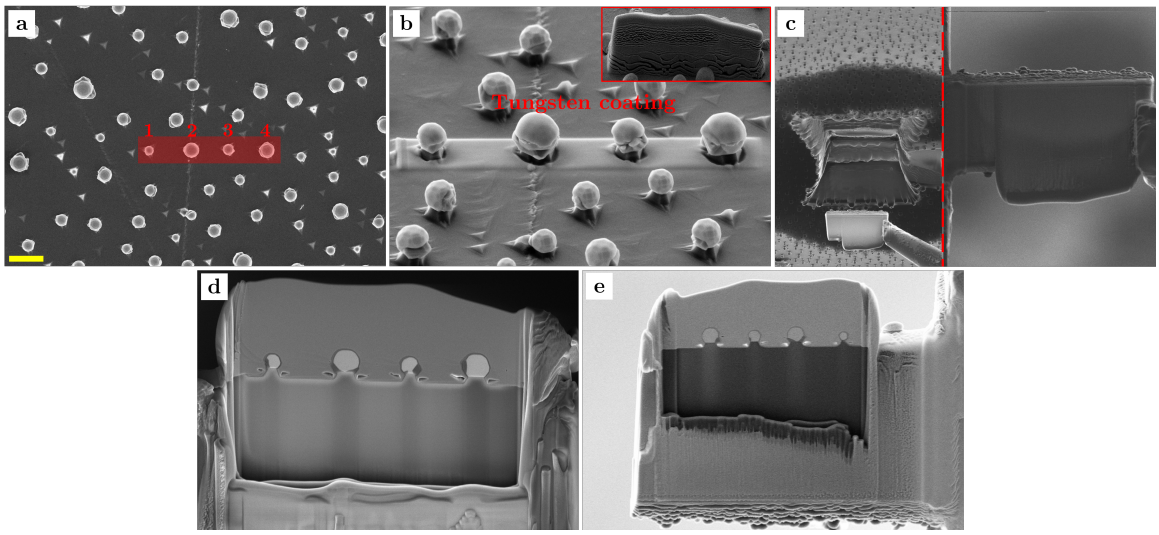


Figure 3.17: (a-e) FIB images of successive steps of preparation of STEM specimens. The yellow scale bar indicates 2 $\mu m$ on image (a).

in FIB system that has led to irregular removal of material and a surface that is not atomically smooth. It is also possible that the FIB cut is made on the wall of spinel necking rather than on the flat surface of its top so that the thin layers of gold and spinel are overlapping at the interface and the slight variations in the thickness may result in spinel atoms at some parts of the edge to become electron transparent.

It should also be noted that in Figure 3.18:image(d) only gold phase is resolved in real atomic representation, because the specimen is tilted such that a zone axis of gold is aligned with beam direction and the contrast in gold phase represent actual columns of atoms. Despite epitaxial alignment of gold and spinel in in-plane (upwards) direction, there are no zone axes of both phases coinciding in out-of-plane direction, because the FIB cut through the intricate structure was in an arbitrary direction. Therefore, spinel contrast, albeit structurally representative, is an unrealistic illustration of its constituents.

EELS analysis was also conducted on the specimen which confirms the presence of significant amounts of copper, mostly concentrated to the irregular protrusions at each side of the gold particle. Figure 3.19 shows the elemental maps acquired from the sample. Overall, the existence of gold, oxygen, aluminum, magnesium, copper, and tungsten (map is not shown here) is confirmed. The presence of gold, as expected, is only confined to the spherical particle. The necking structure underneath gold

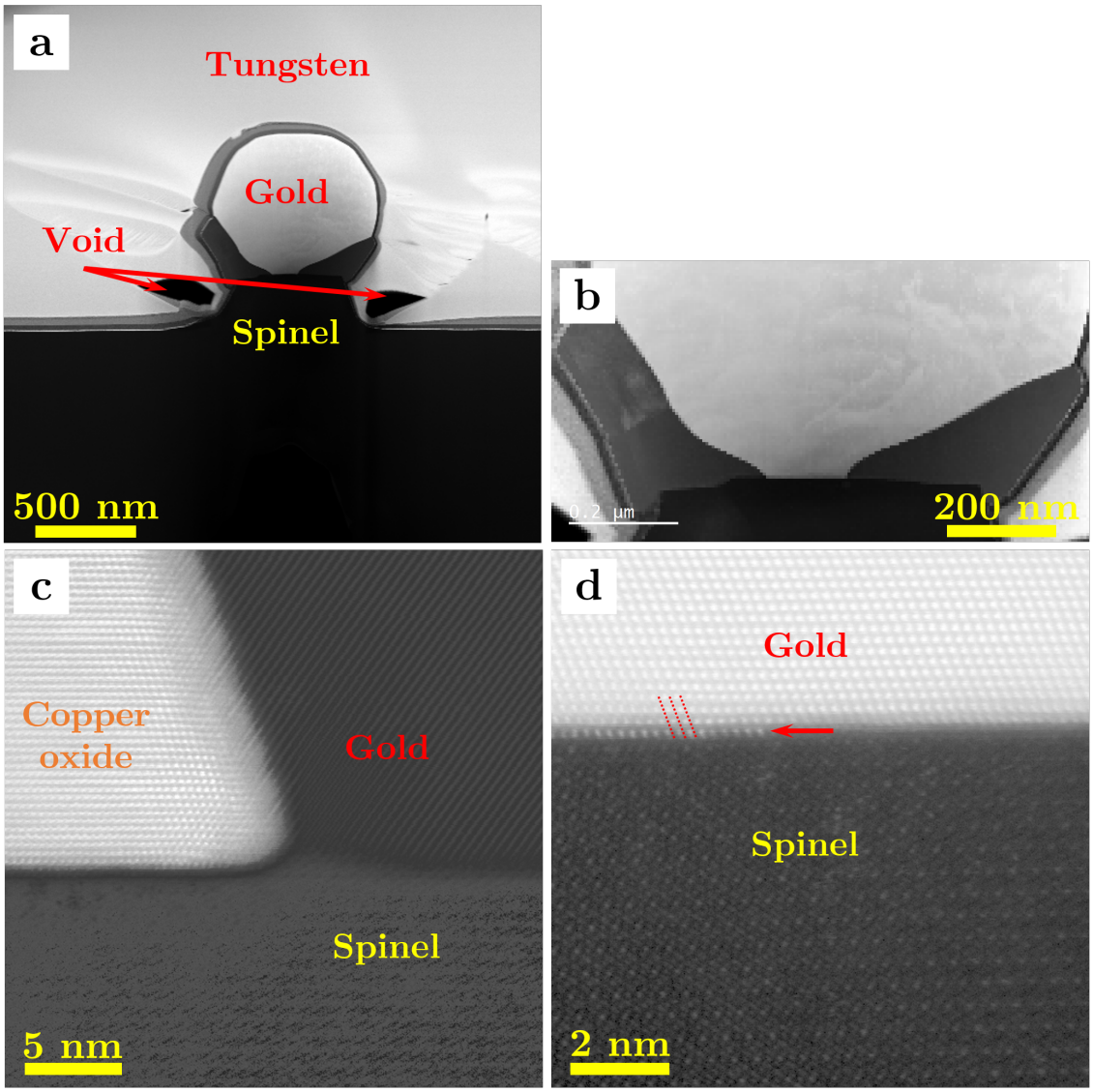


Figure 3.18: HAADF STEM images of (a) cross-section of gold-spinel intricate structure, (b) magnified interface region, (c) gold-copper oxide-spinel triple junction, and (d) gold-spinel interface. The arrow in image (d) shows a row of gold atoms stacked in front of spinel surface layer.

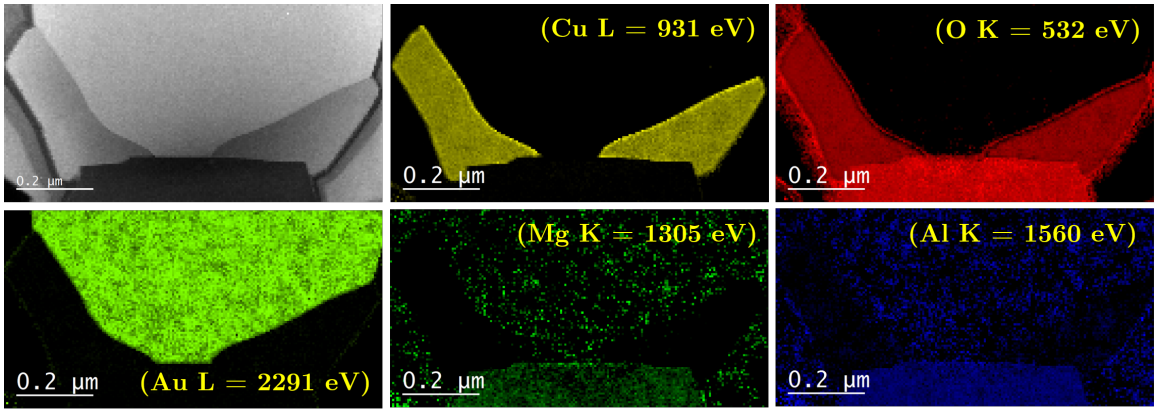


Figure 3.19: EELS elemental maps of the specimen. Characteristic edge energy of each element is also shown on the corresponding map.

consists of Al, Mg, and O, which are the constituents of spinel. Tungsten appears at the sample's surrounding as result of coating applied from FIB step. The irregular protrusions between gold and spinel consist of copper and oxygen.

Magnesium and aluminum appear to be spread into other areas than spinel which is likely because of redeposition of these species after being sputtered during FIB ion milling. Oxygen, on the other hand, has a significant presence in the irregular protrusions along side copper. This might indicate that those protrusions are actually copper oxide phases rather than pure Cu, which also explains the fact that they have segregated to periphery of the gold. This means that during the process of annealing, most of the copper solute inside the gold has oxidized and therefore became insoluble in gold and segregated to separate phases. However, trace amounts of copper still remains inside the gold particle and especially at the interface as indicated from APT. It should be noted that concentrations detected by EELS are much higher than those detected by APT as the sensitivity of EELS lies somewhere around 5 Wt%.

Figure 3.20(a) shows a diffraction pattern of the region containing Cu and O, which is acquired by fast Fourier transforming (FFT) the HAADF image of that region. Unfortunately, since rows and columns of atoms are not clearly resolved, the diffraction pattern is only one dimensional and is not a full representation of the crystal structure. However, if one accepts that existence of roughly equal amounts of Cu and O atoms at the region indicates existence of CuO phase, then knowing that CuO has a monoclinic lattice and considering the symmetry and packing of the atom, the crystallographic plane that faces out could be (0,1,0) and thus the oblique planes are $(\bar{1},0,1)$. It is

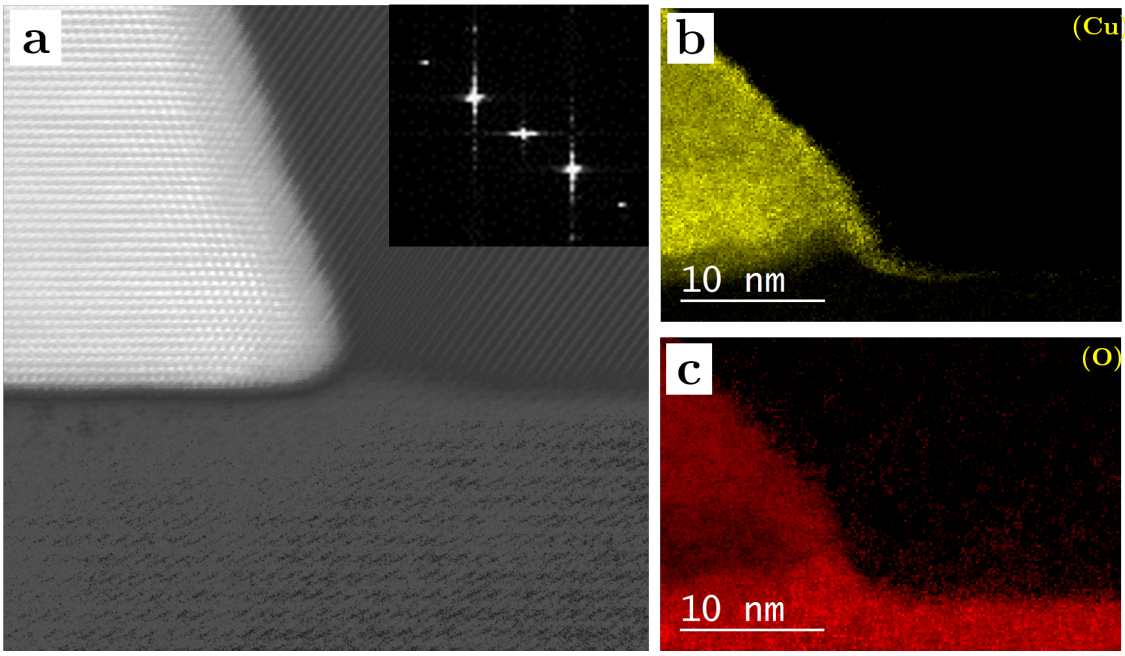


Figure 3.20: (a) Diffraction pattern and d-spacing of ($\bar{1}$,0,1) plane measured from copper oxide region; (b) elemental map of Cu showing the extension of copper to interface of gold and spinel; and (c) higher magnification of oxygen map at the triple junction of gold, spinel, and copper oxide.

therefore, highly likely that the Cu and O containing phase is copper (II) oxide, which is also thermodynamically the most stable oxide phase of copper. However, to exactly identify the phase of Cu-O containing region high resolution electron diffraction is required.

Based on the APT results, HAADF atomic resolution images, and EELS analysis, it can be proposed that presence of Cu contamination in the samples may alter the boundary of gold spinel (by creation of triple junctions) and, in particular, the formation of interface complexion. However, based on HAADF images, even at the direct interface of gold and spinel no evidence of a complexion layer was observed. It is also in contradiction with other reports of complexion phases where impurity atoms tend to migrate into complexion phase, increasing the thickness of interface complexions. Therefore, the proposal that impurities inhibit formation of complexions seems implausible.

It should also be noted, in case of interface complexions discovered so far, definite complexion compositions which are distinct from their adjacent phases have been

reported [47]. In some cases, there is even a "*third phase*" involved in formation of the interface complexion [50]. Thus, formation of gold-spinel bilayer complexion, which does not possess a different composition than its neighboring phases nor does it involve a third phase equilibrated between the adjacent phases, can be regarded as a phenomenon different from complexion quasi-phases.

Moreover, fundamental theory of complexions is based on Gibbs adsorption theorem, as discussed in Section 1.5, "Complexions at Interfaces". Gibbs adsorption theorem states that if the product of surface excess and a differential increase in chemical potential of a component is positive, then the surface tension reduces by the same amount of that product. It is then deduced that by satisfying the conditions of Gibbs adsorption theorem, reduction of surface tensions and consequent spread of one phase on the other to take place. This is particularly true about interface complexions which emerge as a result of satisfied conditions of Gibbs theorem. Therefore, in any interface complexion, it is expected to observe a larger surface area of complexion at the interface causing lowered contact angle between adjacent phases as opposed to a situation where no complexion has formed. None of these expectations were experimentally confirmed in case of gold-spinel interface.

As chemical analyses indicated, significant amounts of unintentional copper contaminations were present in the samples, which as known so far, affect the shape of gold particles. Therefore, it is interesting to study the effect of Cu contamination in the samples. All samples studied so far were produced by sputter coating and it is suspected that the source of contamination might come from sputtered copper containing components of the instruments that are close to target material and are affected by Ar plasma. To eliminate Cu contamination in the samples, other methods of film deposition were employed to produce gold films the results of which are discussed in following section.

## 3.7 Effect of Elemental Contaminants in Development of Intricate Structures

To further investigate the effect of copper contamination in the samples, a series of experiments comparing gold thin films with deposited by thermal evaporation and e-beam evaporation coating methods was carried out. To effectively eliminate any

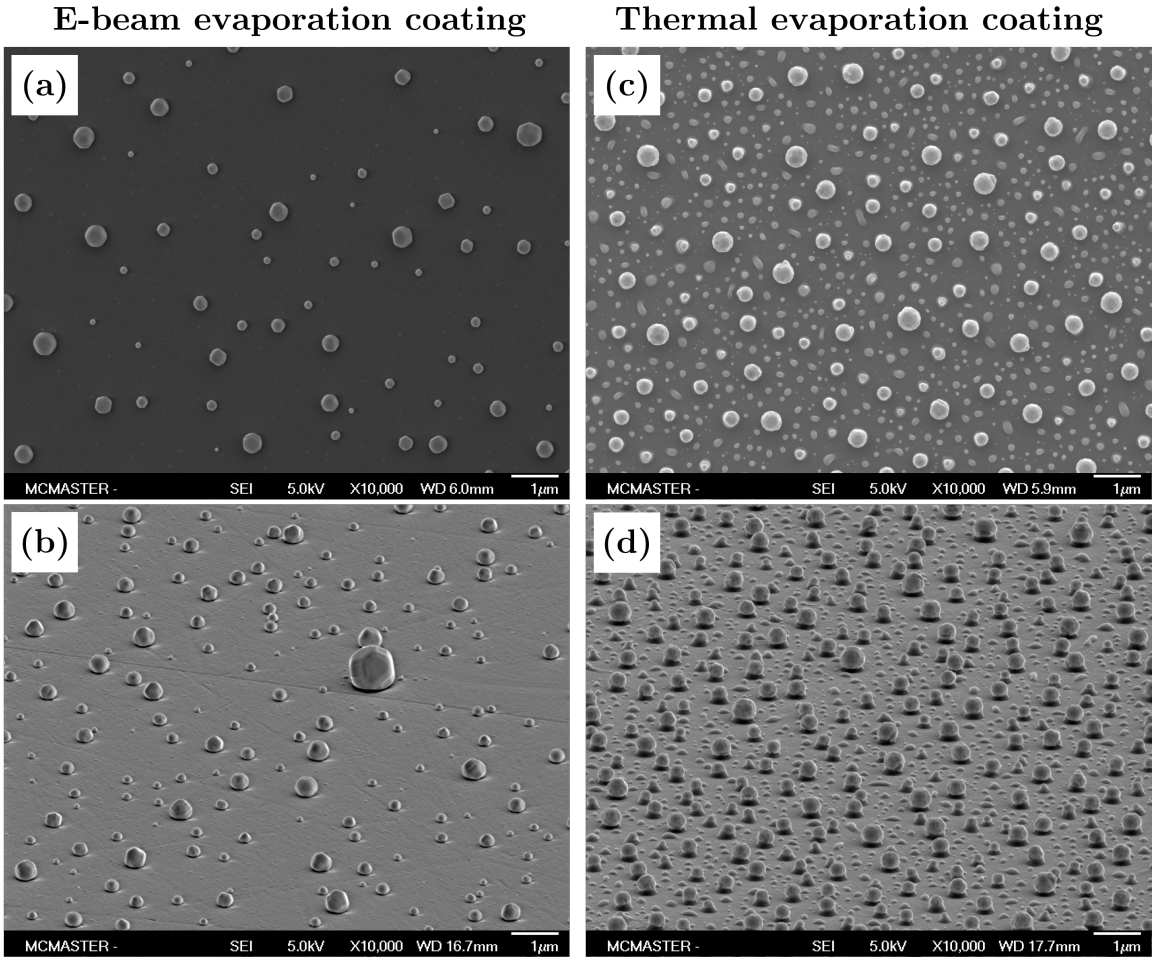


Figure 3.21: (a) Top-view and (b) 70° tilted-view SEM images of the sample prepared via e-beam evaporation coating. (c) Top-view and (d) 70° tilted-view SEM images of the sample prepared via thermal evaporation coating.

other elemental impurities like copper, the heat treatment process also conducted in a new furnace setup with a new quartz tube. Two (111) spinel substrates were coated with 10 nm of gold, deposited by thermal evaporation and e-beam evaporation coating apparatuses. Both samples were heat treated at 1150 ℃ for 2 two hours (starting from room temperature) and then at 1000 ℃ for another two hours. Figure 3.21 shows SEM images of the so-prepared samples.

Comparing the SEM images of the samples, one can find striking differences between the two. First, the sample produced via e-beam evaporation coating (3.21(a & b)) shows faceted gold particles (equilibrium facets of (111) and (110) planes) with no

irregular protrusions. This topographic observation hints that there effectively are no copper-like contaminations that might form oxide phases during annealing and segregate from the main body of gold particles. Secondly, there is no evidence of formation of any spinel necking structure underneath the gold particles in the sample prepared via e-beam evaporation coating. This suggests that there is a strong link between elemental contaminations such as copper and self-assembly of spinel.

On the other hand, in the sample produced via thermal evaporation coating (3.21(c & d)), most of gold particles appear to be associated with irregular protrusions of copper oxide phase at their periphery. Almost all of gold particles seem to be situated on a necking structure which is self-assembled spinel, thus proving the formation of intricate structures. There are numerous other particles in between the intricate structures with shape of droplets which are most likely of silicon oxide nature and are introduced to the sample during heat treatment process from the quartz tube of furnace. There can be found seldom sign of such particles in the sample created through e-beam evaporation coating which was annealed in the same furnace (with the same tube) after the thermal evaporation coated sample. However, there seem to be no interference of the formation of intricate structures with existence of Si-O species in the samples.

To confirm the existence of copper in the thermal evaporation coated sample, EDS chemical analysis along with BSE mode microscopy were implemented on the sample. Figure 3.22 shows a BSE image (BSI) and the EDS spectra of two spots on one of the gold particles that was perceived to be copper-rich (on the irregular protrusion) and otherwise (on the main body of the gold particle). The contrast of the BSI is atomic mass sensitive and therefore any contrast differences indicates a different phase. This contrast difference was the main guidance as to where acquire proper EDS spectra.

As can be seen from the EDS spectra, gold and spinel components (Al, Mg, O) as well as carbon (C), platinum (Pt), silicon (Si), and copper (Cu) are detected in the sample. Pt is anticipated because it was applied as a conductive coating prior to SEM imaging. However, the peak location is tightly shared with a gold characteristic line and the peak intensity is a convolution of Au $M_\gamma$ line at 2.40 keV and Pt $M_\gamma$ at 2.33 keV. A carbon peak also appears as a result of deposition of organic residue in the SEM chamber which after getting exposed to high-energy electron beam "burn" and create a coating on the sample. The Si peak is attributed to the droplets that were introduced by quartz tube of the furnace as it discussed before.

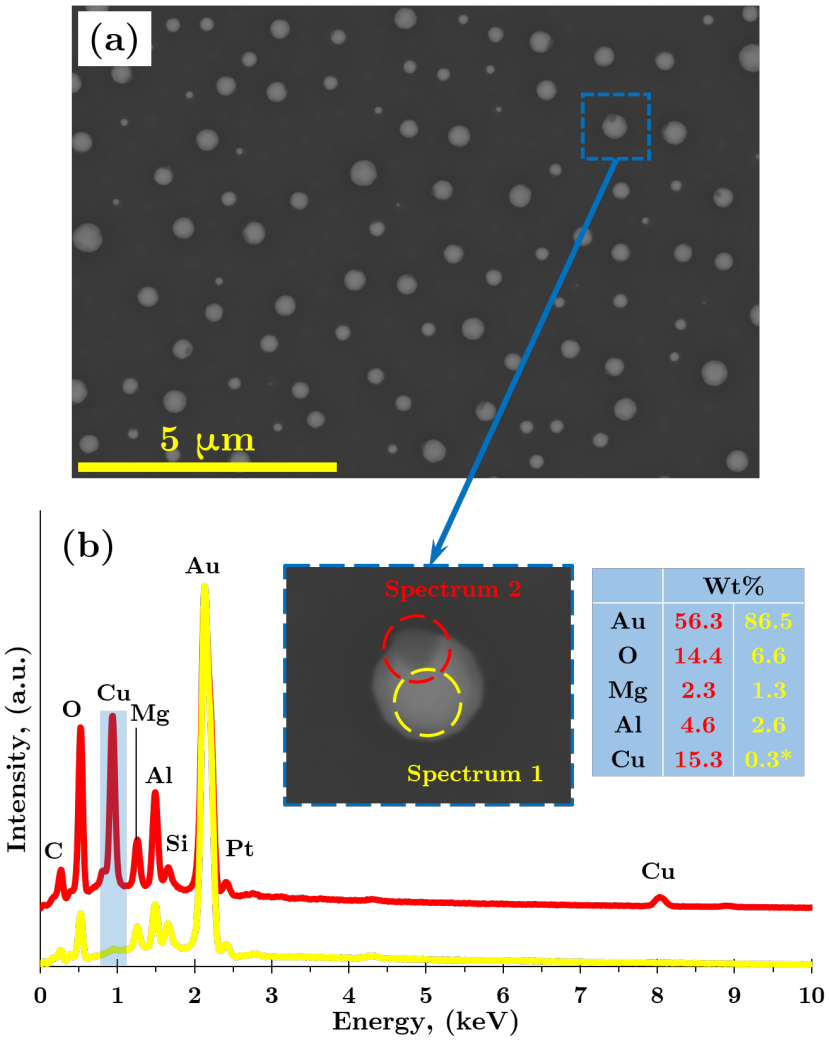


Figure 3.22: (a) BSI of a the sample produced via thermal evaporation coating, (b) EDS spectra from two spots on one of the gold particles featuring an irregular protrusion at its side.(The asterisk on Wt% of Cu at the table indicates a value that is lower than the standard deviation of the quantitative analysis)

The Si peak sometimes appears in EDS spectra as an artifact that is caused by excitement of characteristic X-rays of Si in silicon drift detector (SDD). However, several other EDS spectra that were acquired strictly from droplets on the surface of the sample show the Si peak whereas, those spectra acquired from very large gold particle that can fully contain the interaction volume and effectively block X-rays coming from beyond the particle, do not show the same peak.

It is noticed from comparing the two EDS spectra that by moving from center of gold particle towards what appears to be one of the irregular protrusions on the sides of gold particle, the intensity of Cu, as well as oxygen peak significantly increases and the intensity of the gold peak drops. The quantitative analysis (inset table in 3.22(b)) also corroborates this observation indicating an increase in Cu weight percentage from effectively zero to 15.3. The weight percentage of oxygen cannot be fully attributed to Cu containing phase, because the detector is also picking up signals from the spinel underneath the particle.

The same analyses were conducted on the sample coated via e-beam evaporation deposition. Figure 3.23 shows a BSI and the EDS spectra of one large and one small gold particle. Once again, just considering the contrast of the BSI, only two different phases can be distinguished on this sample; pure gold particles and spinel substrate. There are no signs of CuO accumulations as irregular segregates at the sides of gold particles.

Since there were no apparent irregular protrusions on the sides of gold particles, EDS data acquired on the central points of gold particles. Two different sized gold particles were chosen to also reflect the effect of signals coming from spinel background. As seen in the magnified inset BSI in 3.23(b), the dashed circles approximate the lateral dimensions of interaction volume of the primary electron beam and the sample at 10 keV. EDS spectra again indicates characteristic emissions of spinel components and gold as well as carbon from organic residues. However, there are no apparent peaks at location fo the Cu characteristic $L_\alpha$ line at 0.93 keV and $L_\alpha$ line at 8.02 keV which are marked by blue boxes on the spectra.

Comparing the two EDS analyses from two samples coated with thermal and e-beam evaporation deposition methods, it is obvious that high purity coatings may be achieved from strictly controlled deposition environment as in deposition chamber of e-beam evaporation apparatus which offers a very high vacuum levels, a magnetically confined pathway for evaporated target material to solely condense on the substrate,

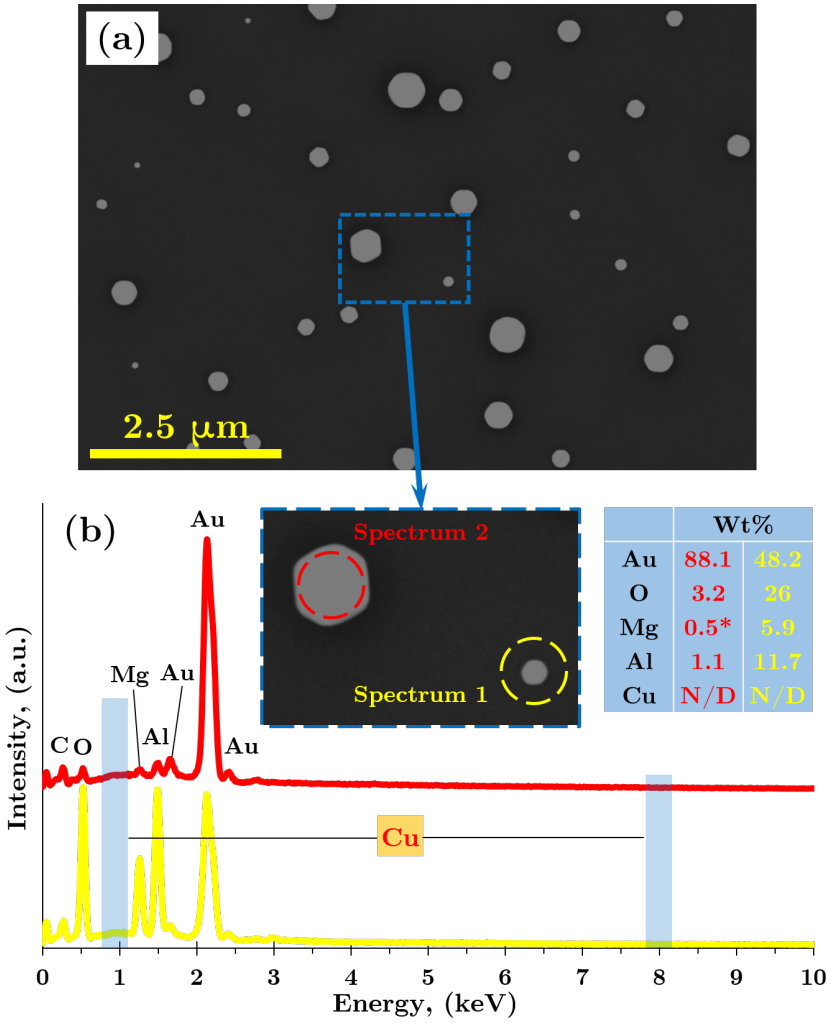


Figure 3.23: (a) BSI of the sample produced via e-beam evaporation coating, (b) EDS spectra from one large and one small gold particle. (The asterisk on Wt% of Mg at the table indicates a value that is lower than the standard deviation of the quantitative analysis – N/D = Not Detected)

and effective reduction of redeposition of other substances from chamber walls onto the substrate.

Moreover, by juxtaposing EDS and SEM results of the samples produced from two methods, it is clear that two otherwise identical samples can illustrate very different self-assembly features caused only by introduction of copper contamination. The results suggest the sensitivity of this process to any contaminations, especially elemental impurities. In this case, lack of copper contamination has prohibited formation of

spinel self-assemblies.

As it was discussed previously, heat treatment parameters also have crucial impact on self-assembly of intricate structures and their size. Therefore, it is important to ensure the influence of copper contamination is still consistent in extreme heat treatment conditions. For this purpose, once more, two (111) spinel substrates were coated with 50 nm of gold; one by thermal evaporation and the other by e-beam evaporation deposition methods. Both samples were separately annealed according to the harshest heat treatment profiles conducted in this work, in which the samples were inserted into furnace at 850 ℃ ramped up to 1190 ℃ and soaked at that temperature for 4 hours, then cooled down to 1050 ℃ and again soaked there for 4 more hours and then cooled to room temperature.

So-prepared samples were then taken for further SEM and EDS analyses. Figure 3.24 shows the SEM images, top- and tilted-view, acquired from the samples that were produced via thermal and e-beam evaporation coating in identical initial gold film thicknesses and were annealed identically as well.

As the SEM images show the results are similar to what was observed in case of the previous samples coated with thiner gold layer and annealed at lower temperatures in 3.21. Once again, the e-beam evaporation coated sample (3.24(a & b)) shows faceted gold particles with no irregular protrusions. Consequently, as expected, there is no evidence of formation of any spinel self-assembly underneath the gold particles in this sample confirming the link between copper contaminations and self-assembly of spinel regardless of what heat treatment profile used to anneal the samples.

On the other hand, in the sample produced via thermal evaporation coating (3.24(c & d)), each gold particle appears to be associated with several irregular protrusions of copper oxide phase at their peripheries, indicating a higher ratio of copper existence in the initial gold film. These copper contaminated gold particles are sitting on self-assembled spinel structures. There are also numerous other much smaller intricate structures in between the spacings of larger ones that appear to connect a path between two adjacent large intricate structures as observed in top-view image (3.24(c)). Tilted-view image and the magnified inset, on the other hand, reveal the intricate shape of these smaller particles (3.24(d)).

To further substantiate existence of copper contamination and its link to growth of intricate structures, BSE mode microscopy and EDS spectroscopy implemented on the samples. Figure 3.25 shows a BSI and the EDS spectra on different spots on a gold

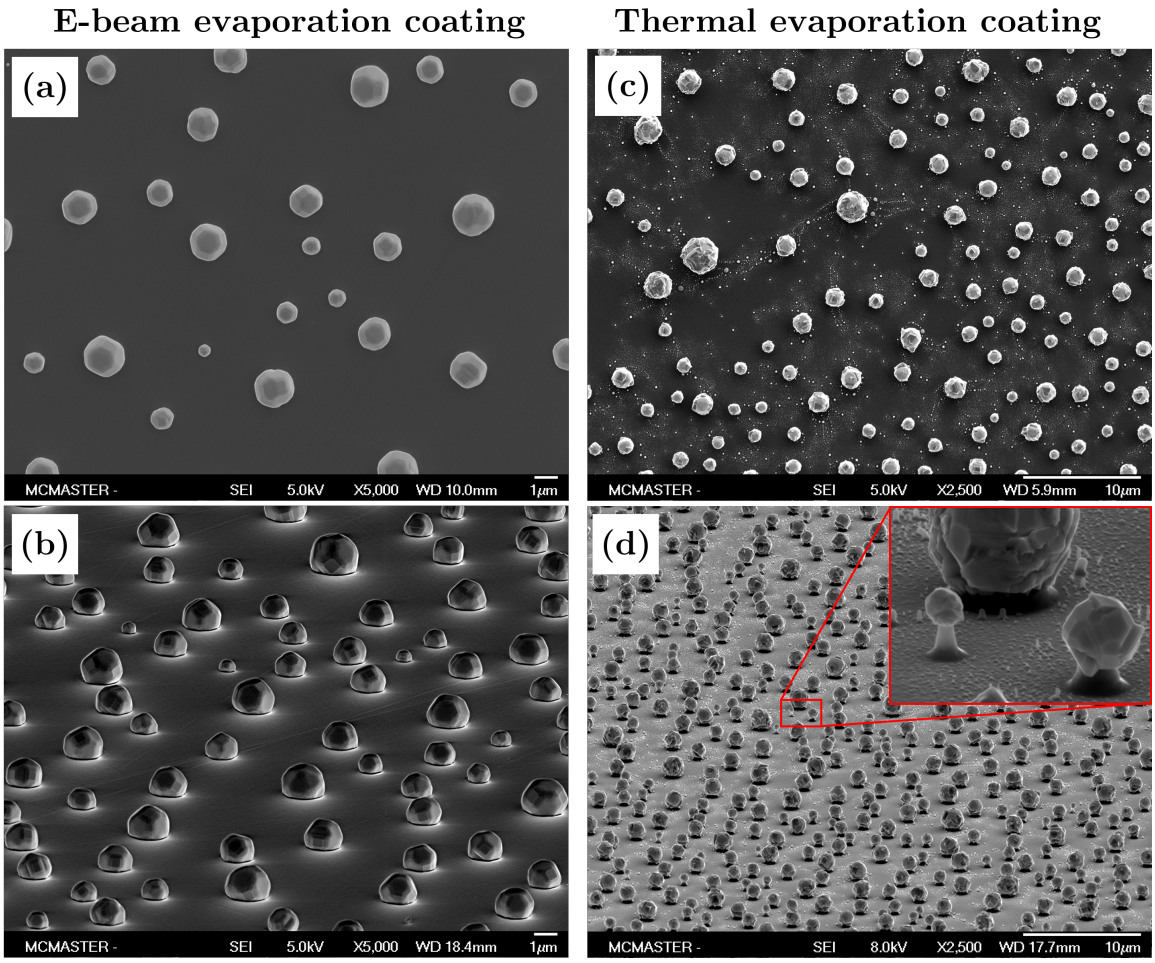


Figure 3.24: (a) Top-view and (b) 70° tilted-view SEM images of the sample prepared via e-beam evaporation coating. (c) Top-view and (d) 70° tilted-view SEM images of the sample prepared via thermal evaporation coating.

particle, following the difference in the brightnesses of each region to approximately position the electron beam and produce characteristic X-rays from each phase.

As seen from BSI, the irregular protrusions appear in darker contrast on different regions of the gold particle which appears brighter due to the fact that gold is heavier than copper and can generate more BSE signals. Moreover, the EDS spectra also support this observation by showing a pair characteristic Cu peaks in spectrum 2 which was acquired from darker protrusion. However, spectrum 1 has no such peaks corresponding to presence of copper and the gold characteristic peak dominantly appears as the only detected element (along with Al from spinel background).

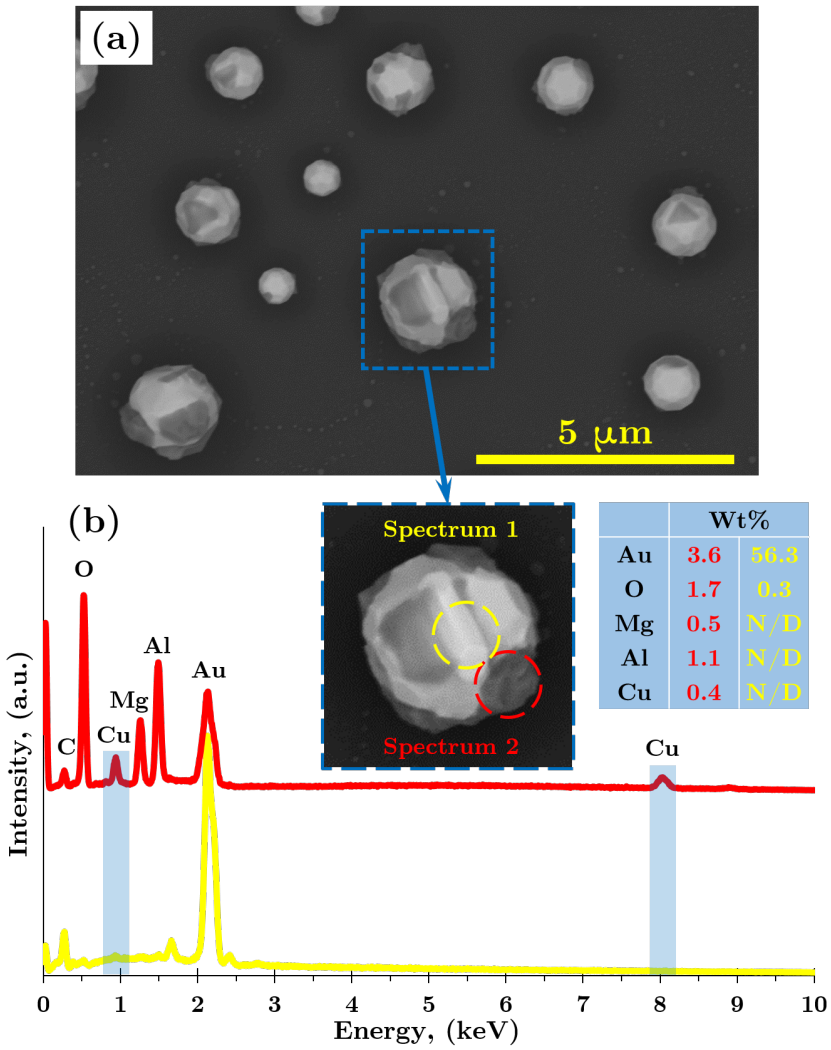


Figure 3.25: (a) BSI of a the sample produced via thermal evaporation coating, (b) EDS spectra from two spots on one of the gold particles featuring irregular protrusions at its outer surface. (N/D = Not Detected)

The results of same analyses from the sample coated via e-beam evaporation deposition are represented as Figure 3.26, which shows a BSI and the EDS spectra of two large and small gold particles. From the contrast of BSI, only two phases of pure gold and spinel substrate can be distinguished on this sample. There are no signs of CuO accumulations as irregular segregates at the sides of gold particles which is also confirmed by EDS spectra acquired from two different size particles. In the spectra of both particles, there are chiefly two peaks of carbon and gold present. A very weak

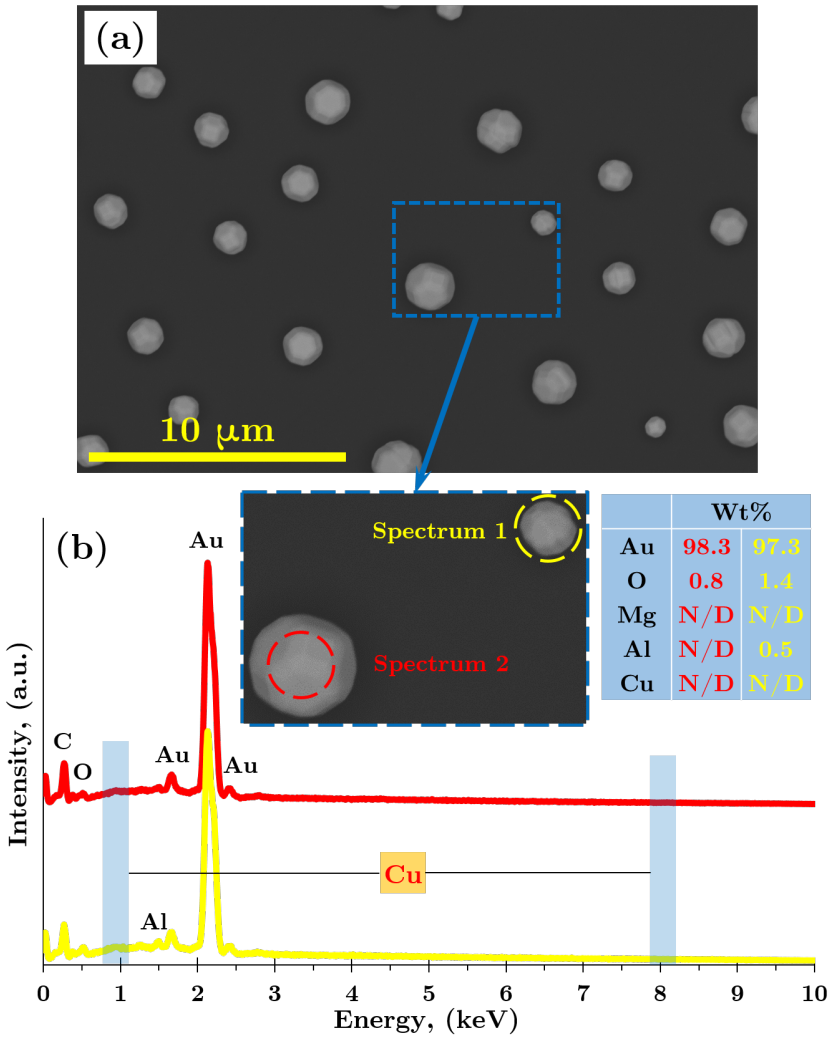


Figure 3.26: (a) BSI of a the sample produced via e-beam evaporation coating, (b) EDS spectra from two large and small gold particles. (N/D = Not Detected)

oxygen peak is also detected in both particles which again can be attributed to the spinel background. Some aluminum is also detected in spectrum 1 from the small particle which also belongs to the spinel at background.

Overall, the BSE microscopy and EDS chemical analysis of the samples produced from different coating routes indicates the substantial impact of copper contamination in formation of intricate structures on the samples that are identical in all aspects except for containing copper. Copper contamination appeared in form of CuO, as HAADF STEM and EELS indicated, and segregated as irregular protrusions at the

surface gold particles. It was shown that the samples coated with thermal evaporation and sputtering methods could contain significant amounts of copper which later during heat treatment process oxidizes and also leads to formation of intricate structures. On the other hand, e-beam evaporation coating proved to be superior in providing very clean and pure thin films of gold.

The effect of copper contamination in development of intricate structures may be regarded as a chemical one. In one hypothesis, it could be assumed that copper atoms at the interface of gold and spinel reacts with the oxygen that is leaving the surface of spinel as a result of relaxation through reconstruction during the heat treatment process. But, since copper is dissolved in gold and aluminum and magnesium can readily reduce copper (due to their more negative enthalpy of oxidization), Cu-O bonds break apart and Al and Mg substitute Cu. The newly formed Al-O and Mg-O oxide species are not soluble in gold and therefore sediment back onto the substrate and during this process, they epitaxially grow as pyramidal spinel structures.

As it was observed that heat treatment at high temperatures and long durations leads to formation of larger self-assemblies, it is proposed that the process of oxidization/reduction of copper continues as long as the energy to carry the reactions forward is provided. As system reach the end of annealing time the reactions also stop, dewetted gold solidifies, and intricate structures form. This also explains why some self-assembled spinel structures are bare full pyramids with sharp apex and some are in form of frustums capped with gold particles. Sharp pyramids are those which formed at early stages of heat treatment and therefore had enough time to be developed to full shape. On the contrary, frustums either start to develop later or due to having larger footprints (directly related to the size of dewetted gold particle on top), take a long time to fully get shaped as a pyramid. As temperature drops below temperature of surface reconstruction of spinel which causes reduction in oxygen concentration or when it drops below the required activation energy of oxidization/reduction reactions, frustums stop to grow. This is nevertheless a hypothetical speculation and to evidently substantiate such a growth mechanism, there must be further in-situ analytical tests conducted.

# Chapter 4

# Conclusions

The self-assembly of intricate gold-spinel structures were investigated as a result of dewetting gold thin films on single-crystalline magnesium aluminate substrates. Earliest reports had attributed the whole composition of these structures to gold but recent studies had found that the intricate structures are actually made of a spherical gold particle sitting on top of self-assembled spinel necking. It was reported that the boundary of gold particles and spinel necking structures are of interface complexion nature in which, a bilayer of alternating gold and oxygen atoms instead of atomically sharp gold and spinel boundary is formed. Consequently, self-assembly of spinel necking structures were attributed to presence of this complexion layer.

However, these results could not be reproduced in this study, as high resolution HAADF STEM evidence illustrated. In fact, based on our experimental evidence, the boundary layer is atomically sharp and no sign of interface complexion was realized. As previously argued, it is possible that overlap of spinel and gold boundaries at the interface has produced an artifact that led to a false perception of interface complexion. Theoretical foundations and experimental evidence of interface complexions that were manifested in other systems, are also at odds with what has been reported about the interface of gold and spinel in intricate structures.

It was also observed that presence of copper contamination in gold film is the main cause for formation of spinel self-assembly. It was observed that in identical conditions dewetting a copper containing gold film would lead to formation of self-assembled structures, whereas dewetting pure gold films did not result in self-assembly of spinel. Therefore, it was concluded that self-assembly of spinel is caused by a chemical reaction

that involves presence of both gold and copper.

The heat treatment conditions were also found to affect the shape of intricate gold-spinel structures. It was observed that the samples which were annealed based on a high thermal gradient profile had developed higher surface density of intricate structures with taller spinel self-assemblies. Thus, it was concluded that thermal gradient remarkably affect the kinetics of the reaction that cause self-assembly of spinel.

# Chapter 5

# Future Outlook

This study has been in continuation of a series of previous investigations into the novel phenomenon of self-assembly of intricate gold-spinel structures. As it was discussed, some previously held perceptions about this phenomenon were disputed and rejected in the current work, some of the conclusions were modified, and some new ideas put forward which have advanced the overall understanding of the phenomenon. However, this work cannot claim to have presented a complete picture of the case and there are numerous issues to be researched and discovered in order to further develop the understanding of the phenomenon. There are particularly two areas of research that stand out as primary candidates of future studies. Following paragraphs introduce these subjects and lay out potential arrangements of what, in author's belief, can lead to results that could significantly improve the current vision.

## 5.1 Other Metal-Oxide Case Studies

Although the novel phenomenon of self-assembly of intricate structures are discovered only in case of gold-spinel system, but there does not seem to exist any fundamentally restricting issues that may preclude other metal-oxide systems from developing such structures. There has been number of features about gold and spinel system such as surface reconstruction of spinel at temperatures within the range of what has been conducted in this study, catalytic properties of gold nanostructures especially at its interface with oxide crystals, and most importantly, presence of copper contaminations in gold film that so far, known to be causing such unique effects in gold-spinel system.

Also, dewetting behavior of other metals on spinel such as pure copper and platinum thin films were briefly studied in current work that showed promising results in terms of illustrating the same self-assembly features. But, that study was far from comprehensive and could potentially advanced to include an extended range of metals. Furthermore, it is reasonable to first check for the proper overlays of metal and possibly alloy thin films on spinel surface. Then, the study can advance towards other choices of oxide substrates that have similar properties as magnesium aluminate spinel such as surface relaxation through reconstruction. Two interesting candidates for this matter could be sapphire and magnesium oxide.

## 5.2 In-situ Investigations into Potential Mechanisms

Different aspects of gold-spinel self-assembly in the form of intricate structures have been studied in current and previous works. For instance, effect of different profiles of heat treatment and thermal gradient, effect of thickness of initial metallic thin film, and effect of chemical composition of initial metallic thin film have been investigated so for. Amongst the aforementioned subjects, the factor of chemical composition seems to be the most crucial in development of intricate structures.

Therefore, it is highly likely that any self-assembly mechanism involves some forms of chemical reaction(s) at the interface when the system undergoes heat treatment process. However, to map a detailed and step-by-step procedure as to how different potential processes such as surface diffusion, catalytic effects at the interface, and elctrochemistry of different components and especially that of copper would play out in the course of heat treatment to develop intricate structures requires a systematic study of the interface on atomic scale during the annealing process.

A starting point ot realize such study may be performing in-situ high resolution STEM equipped with a hot stage that an heat the system to temperatures around 1100-1200 ℃ and is capable of resolving atoms and their motions in the course of heat treatment. Such experiment could illustrate any diffusion process at the interface and self-assembly of spinel necking structures. Simultaneous electron energy loss spectroscopy coupled with convergent-beam electron diffraction could further advance the understandings of the mechanism of intricate structures' self-assembly.

# Bibliography


[1] M Rudolph and ASK Hashmi. "Gold catalysis in total synthesis – an update". In: *Chemical Society Reviews* 41.6 (2012), pp. 2448–2462 (cit. on p. 1).

[2] NR Jana, L Gearheart, and CJ Murphy. "Seed-mediated growth approach for shape-controlled synthesis of spheroidal and rod-like gold nanoparticles using a surfactant template". In: *Advanced Materials* 13.18 (2001), p. 1389 (cit. on p. 1).

[3] AL Giermann and CV Thompson. "Solid-state dewetting for ordered arrays of crystallographically oriented metal particles". In: *Applied Physics Letters* 86.12 (2005), p. 121903 (cit. on p. 1).

[4] David Phillip Woodruff. *The Solid-Liquid Interface*. Cambridge Monographs on Physics. Cambridge University Press, 1973. ISBN: 9780521201230. URL: https://books.google.ca/books?id=wKk8AAAAIAAJ (cit. on pp. 2, 4, 5).

[5] Kenjiro Oura, VG Lifshits, Alexander Saranin, AV Zotov, and M Katayama. *Surface Science: An Introduction*. Springer Science & Business Media, 2013 (cit. on p. 4).

[6] Harald Ibach. *Physics of surfaces and interfaces*. Vol. 10. Springer, 2006 (cit. on p. 5).

[7] PG de Gennes, F Brochard-Wyart, and D Quere. *Capillarity and Wetting Phenomena: Drops, Bubbles, Pearls, Waves*. Springer, 2004. ISBN: 9780387005928. URL: https://books.google.ca/books?id=MxLQk8vms-kC (cit. on pp. 6, 8–18).

[8] D Bonn, J Eggers, J Indekeu, J Meunier, and E Rolley. "Wetting and spreading". In: *Reviews of Modern Physics* 81.2 (2009), p. 739 (cit. on pp. 7, 8, 14).

[9] PG De Gennes. "Wetting: statics and dynamics". In: *Reviews of Modern Physics* 57.3 (1985), p. 827 (cit. on p. 8).

[10] VM Starov, MG. Velarde, and CJ Radke. *Wetting and Spreading Dynamics*. Surfactant Science. CRC Press, 2007. ISBN: 9781420016178. URL: `https://books.google.ca/books?id=NT6KPxETpPMC` (cit. on pp. 10, 12, 13).

[11] R Clearfield, JG Railsback, RC Pearce, DK Hensley, JD Fowlkes, M Fuentes-Cabrera, ML Simpson, PD Rack, and Anatoli V Melechko. "Reactive solid-state dewetting of Cu–Ni films on silicon". In: *Applied Physics Letters* 97.25 (2010), p. 253101 (cit. on p. 19).

[12] D Kim, AL Giermann, and CV Thompson. "Solid-state dewetting of patterned thin films". In: *Applied Physics Letters* 95.25 (2009), p. 251903 (cit. on p. 19).

[13] Jongpil Ye. "Solid-state dewetting of continuous and patterned single crystal Ni thin films". PhD thesis. Massachusetts Institute of Technology, 2011 (cit. on pp. 19, 20).

[14] CV Thompson. "Solid-state dewetting of thin films". In: *Annual Review of Materials Research* 42 (2012), pp. 399–434 (cit. on pp. 19–21).

[15] WW Mullins. "Flattening of a nearly plane solid surface due to capillarity". In: *Journal of Applied Physics* 30.1 (1959), pp. 77–83 (cit. on p. 19).

[16] DJ Srolovitz and SA Safran. "Capillary instabilities in thin films. I. Energetics". In: *Journal of Applied Physics* 60.1 (1986), pp. 247–254 (cit. on p. 21).

[17] KE Sickafus, JM Wills, and NW Grimes. "Structure of spinel". In: *Journal of the American Ceramic Society* 82.12 (1999), pp. 3279–3292 (cit. on pp. 22, 23).

[18] EJW Verwey and EL Heilmann. "Physical properties and cation arrangement of oxides with spinel structures: I. Cation arrangement in spinels". In: *The Journal of Chemical Physics* 15.4 (1947), pp. 174–180 (cit. on p. 22).

[19] JB Goodenough and AL Loeb. "Theory of ionic ordering, crystal distortion, and magnetic exchange due to covalent forces in spinels". In: *Physical Review* 98.2 (1955), p. 391 (cit. on p. 22).

[20] C Păcurariu, I Lazău, Z Ecsedi, R Lazău, P Barvinschi, and G Mărginean. "New synthesis methods of $MgAl_2O_4$ spinel". In: *Journal of the European Ceramic Society* 27.2 (2007), pp. 707–710 (cit. on p. 22).

[21] CWarner Parmelee, AE Badger, and GA Ballam. "A study of a group of typical spinels". In: *University of Illinois bulletin; Vol. 29, No. 84* (1932) (cit. on p. 22).

[22] R Sarkar. "Refractory applications of magnesium aluminate spinel". In: *Interceram* (2010) (cit. on p. 22).

[23] M A Khan, CJ Sun, JW Yang, Q Chen, BW Lim, MZ Anwar, A Osinsky, and H Temkin. "Cleaved cavity optically pumped InGaN–GaN laser grown on spinel substrates". In: *Applied Physics Letters* 69.16 (1996), pp. 2418–2420 (cit. on p. 22).

[24] MR Kokta and HT Ong. *Spinel substrate and heteroepitaxial growth of III-V materials thereon.* US Patent 6,844,084. 2005 (cit. on p. 22).

[25] CJ Sun, JW Yang, Q Chen, MA Khan, T George, P Chang-Chien, and S Mahajan. "Deposition of high quality Wurtzite GaN films over cubic (111) $MgAl_2O_4$ substrates using low pressure metalorganic chemical vapor deposition". In: *Applied Physics Letters* 68.8 (1996), pp. 1129–1131 (cit. on p. 22).

[26] CM Fang, SC Parker, and G De With. "Atomistic Simulation of the Surface Energy of Spinel $MgAl_2O_4$". In: *Journal of American Ceramic Society* 83.8 (2000), pp. 2082–2084 (cit. on p. 23).

[27] S Carbonin, F Martignago, G Menegazzo, and A Dal Negro. "X-ray single-crystal study of spinels: in situ heating". In: *Physics and Chemistry of Minerals* 29.8 (2002), pp. 503–514 (cit. on p. 24).

[28] C Noguera. "Polar oxide surfaces". In: *Journal of Physics: Condensed Matter* 12.31 (2000), R367 (cit. on p. 23).

[29] MK Rasmussen, K Meinander, F Besenbacher, and JV Lauritsen. "Noncontact atomic force microscopy study of the spinel $MgAl_2O_4$ (111) surface". In: *Beilstein Journal of Nanotechnology* 3.1 (2012), pp. 192–197 (cit. on pp. 23, 25, 26, 63).

[30] Yeonseop Yu. "Diffusion reactions at metal-oxide interfaces and the effect of an applied electric field". PhD thesis. Case Western Reserve University, 2005 (cit. on p. 25).

[31] WP Davey. "Precision measurements of the lattice constants of twelve common metals". In: *Physical Review* 25.6 (1925), p. 753 (cit. on p. 27).

[32] I Galanakis, N Papanikolaou, and P Dederichs. "Applicability of the broken-bond rule to the surface energy of the fcc metals". In: *Surface Science* 511.1 (2002), pp. 1–12 (cit. on p. 27).

[33] AS Barnard, XM Lin, and LA Curtiss. "Equilibrium morphology of face-centered cubic gold nanoparticles > 3 nm and the shape changes induced by temperature". In: *The Journal of Physical Chemistry B* 109.51 (2005), pp. 24465–24472 (cit. on p. 27).

[34] F Bonaccorso, G Calogero, G Di Marco, OM Marago, PG Gucciardi, U Giorgianni, K Channon, and G Sabatino. "Fabrication of gold tips by chemical etching in aqua regia". In: *Review of Scientific Instruments* 78.10 (2007), p. 103702 (cit. on p. 29).

[35] JA Dean and NA Lange. *Lange's Handbook of Chemistry*. Lange's Handbook of Chemistry. McGraw-Hill, 1992. ISBN: 9780070161948. URL: `https://books.google.ca/books?id=XpxUAAAAMAAJ` (cit. on p. 29).

[36] PH Buffat and JP Borel. "Size effect on the melting temperature of gold particles". In: *Physical Review A* 13.6 (1976), p. 2287 (cit. on pp. 29, 30).

[37] EJ Baerends, WHE Schwarz, P Schwerdtfeger, and JG Snijders. "Relativistic atomic orbital contractions and expansions: magnitudes and explanations". In: *Journal of Physics B: Atomic, Molecular and Optical Physics* 23.19 (1990), p. 3225 (cit. on p. 29).

[38] R Coquet, KL Howard, and DJ Willock. "Theory and simulation in heterogeneous gold catalysis". In: *Chemical Society Reviews* 37.9 (2008), pp. 2046–2076 (cit. on pp. 30, 31).

[39] DJ Gorin and FD Toste. "Relativistic effects in homogeneous gold catalysis". In: *Nature* 446.7134 (2007), pp. 395–403 (cit. on p. 30).

[40] D Thompson. "New advances in gold catalysis: Part I". In: *Gold Bulletin* 31.4 (1998), pp. 111–118 (cit. on p. 31).

[41] S Galvagno and G Parravano. "Chemical reactivity of supported gold: IV. Reduction of NO by $H_2$". In: *Journal of Catalysis* 55.2 (1978), pp. 178–190 (cit. on p. 31).

[42] DY Cha and G Parravano. "Surface reactivity of supported gold: I. Oxygen transfer between CO and $CO_2$". In: *Journal of Catalysis* 18.2 (1970), pp. 200–211 (cit. on p. 31).

[43] M Okumura, S Nakamura, S Tsubota, T Nakamura, M Azuma, and M Haruta. "Chemical vapor deposition of gold on $Al_2O_3$, $SiO_2$, and $TiO_2$ for the oxidation of CO and of $H_2$". In: *Catalysis Letters* 51.1-2 (1998), pp. 53–58 (cit. on p. 32).

[44] M Haruta. "Size-and support-dependency in the catalysis of gold". In: *Catalysis Today* 36.1 (1997), pp. 153–166 (cit. on pp. 32, 55).

[45] ASK Hashmi and GJ Hutchings. "Gold catalysis". In: *Angewandte Chemie International Edition* 45.47 (2006), pp. 7896–7936 (cit. on p. 32).

[46] KA Dick. "A review of nanowire growth promoted by alloys and non-alloying elements with emphasis on Au-assisted III–V nanowires". In: *Progress in Crystal Growth and Characterization of Materials* 54.3 (2008), pp. 138–173 (cit. on pp. 32, 33, 55).

[47] SJ Dillon, M Tang, WC Carter, and MP Harmer. "Complexion: A new concept for kinetic engineering in materials science". In: *Acta Materialia* 55.18 (2007), pp. 6208–6218 (cit. on pp. 33–35, 101).

[48] J Luo, H Cheng, K Meshinchi-Asl, CJ Kiely, and MP Harmer. "The role of a bilayer interfacial phase on liquid metal embrittlement". In: *Science* 333.6050 (2011), pp. 1730–1733 (cit. on p. 33).

[49] MP Harmer. "The phase behavior of interfaces". In: *Science* 332.6026 (2011), pp. 182–183 (cit. on pp. 33, 34).

[50] M Baram, D Chatain, and WD Kaplan. "Nanometer-thick equilibrium films: The interface between thermodynamics and atomistics". In: *Science* 332.6026 (2011), pp. 206–209 (cit. on pp. 34, 35, 101).

[51] J Luo and YM Chiang. "Existence and stability of nanometer-thick disordered films on oxide surfaces". In: *Acta Materialia* 48.18 (2000), pp. 4501–4515 (cit. on pp. 35, 36).

[52] J Luo and YM Chiang. "Wetting and prewetting on ceramic surfaces". In: *Annual Review of Materials Research* 38 (2008), pp. 227–249 (cit. on p. 35).

[53] T Majdi, GZ Zhu, J Carvalho, V Jarvis, K Meinander, JF Britten, G Botton, and JS Preston. "Evidence for an equilibrium epitaxial complexion at the Au-$MgAl_2O_4$ interface". In: *Applied Physics Letters* 107.24 (2015), p. 241601 (cit. on pp. 36, 56, 57, 69, 88).

[54] Peter J Goodhew, John Humphreys, and Richard Beanland. *Electron microscopy and analysis*. CRC Press, 2000 (cit. on pp. 37–40, 42, 43, 45).

[55] Joseph Goldstein, Dale E Newbury, Patrick Echlin, David C Joy, Alton D Romig Jr, Charles E Lyman, Charles Fiori, and Eric Lifshin. *Scanning electron microscopy and X-ray microanalysis: a text for biologists, materials scientists, and geologists*. Springer Science & Business Media, 2012 (cit. on pp. 37–43).

[56] Lucille A Giannuzzi et al. *Introduction to focused ion beams: instrumentation, theory, techniques and practice*. Springer Science & Business Media, 2006 (cit. on pp. 44, 45).

[57] Brent Fultz and James M Howe. *Transmission electron microscopy and diffractometry of materials*. Springer Science & Business Media, 2012 (cit. on pp. 45, 48–50).

[58] Ray Egerton. *Electron energy-loss spectroscopy in the electron microscope*. Springer Science & Business Media, 2011 (cit. on pp. 46, 47).

[59] G Zhu. "High-resolution characterization of low-dimensional defects in $SrTiO_3$". Ph.D. Thesis. McMaster University, 2012 (cit. on pp. 49, 50).

[60] Baptiste Gault, Michael P Moody, Julie M Cairney, and Simon P Ringer. *Atom Probe Microscopy*. Vol. 160. Springer Science & Business Media, 2012 (cit. on pp. 51–54, 66).

[61] Michael K Miller and Richard G Forbes. *Atom-Probe Tomography: The Local Electrode Atom Probe*. Springer, 2014 (cit. on pp. 51–54).

[62] Christopher Favazza, Ramki Kalyanaraman, and Radhakrishna Sureshkumar. "Robust nanopatterning by laser-induced dewetting of metal nanofilms". In: *Nanotechnology* 17.16 (2006), p. 4229 (cit. on p. 55).

[63] F Ruffino and MG Grimaldi. "Template-confined dewetting of Au and Ag nanoscale films on mica substrate". In: *Applied Surface Science* 270 (2013), pp. 697–706 (cit. on p. 55).

[64] J Petersen and SG Mayr. "Dewetting of Ni and NiAg solid thin films and formation of nanowires on ripple patterned substrates". In: *Journal of Applied Physics* 103.2 (2008), p. 023520 (cit. on p. 55).

[65] H Krishna, R Sachan, J Strader, C Favazza, M Khenner, and R Kalyanaraman. "Thickness-dependent spontaneous dewetting morphology of ultrathin Ag films". In: *Nanotechnology* 21.15 (2010), p. 155601 (cit. on p. 55).

[66] E Rabkin, D Amram, and E Alster. "Solid state dewetting and stress relaxation in a thin single crystalline Ni film on sapphire". In: *Acta Materialia* 74 (2014), pp. 30–38 (cit. on p. 55).

[67] J Bischof, D Scherer, S Herminghaus, and P Leiderer. "Dewetting modes of thin metallic films: Nucleation of holes and spinodal dewetting". In: *Physical Review Letters* 77.8 (1996), p. 1536 (cit. on p. 55).

[68] JE Yoo, K Lee, M Altomare, E Selli, and P Schmuki. "Self-organized arrays of single-metal catalyst particles in $TiO_2$ cavities: A highly efficient photocatalytic system". In: *Angewandte Chemie International Edition* 52.29 (2013), pp. 7514–7517 (cit. on p. 55).

[69] F Silly and MR Castell. "Bimodal growth of Au on $SrTiO_3$ (001)". In: *Physical Review Letters* 96.8 (2006), p. 086104 (cit. on p. 55).

[70] C Favazza, J Trice, H Krishna, R Kalyanaraman, and R Sureshkumar. "Laser-induced short-and long-range orderings of Co nanoparticles on $SiO_2$". In: *Applied Physics Letters* 88.15 (2006) (cit. on p. 55).

[71] CY Hsu, JW Huang, S Gwo, and KJ Lin. "The facile fabrication of tunable plasmonic gold nanostructure arrays using microwave plasma". In: *Nanotechnology* 21.3 (2009), p. 035302 (cit. on p. 55).

[72] X Hu, DG Cahill, and RS Averback. "Nanoscale pattern formation in Pt thin films due to ion-beam-induced dewetting". In: *Applied Physics Letters* 76.22 (2000) (cit. on p. 55).

[73] S Yang, B Cao, L Kong, and Z Wang. "Template-directed dewetting of a gold membrane to fabricate highly SERS-active substrates". In: *Journal of Materials Chemistry* 21.36 (2011), pp. 14031–14035 (cit. on p. 55).

[74] NC Lindquist, P Nagpal, KM McPeak, DJ Norris, and SH Oh. "Engineering metallic nanostructures for plasmonics and nanophotonics". In: *Reports on Progress in Physics* 75.3 (2012), p. 036501 (cit. on p. 55).

[75] VM Shalaev. "Optical negative-index metamaterials". In: *Nature Photonics* 1.1 (2007), pp. 41–48 (cit. on p. 55).

[76] GA Devenyi, J Li, RA Hughes, AC Shi, P Mascher, and JS Preston. "Epitaxially driven formation of intricate supported gold nanostructures on a lattice-matched oxide substrate". In: *Nano Letters* 9.12 (2009), pp. 4258–4263 (cit. on pp. 55, 56, 63, 64, 69–71).

[77] T Majdi. "Novel self-assembly of crystalline $MgAl_2O_4$ nanostructures promoted by annealing a gold overlayer on a (111) $MgAl_2O_4$ substrate". Master's Thesis. McMaster University, 2013 (cit. on pp. 55–57, 63, 64, 69–71, 73, 75).

[78] SR Zainab. "Electron backscatter diffraction of gold nanoparticles". Master's Thesis. McMaster University, 2015 (cit. on pp. 57, 69).

[79] J Trice, C Favazza, D Thomas, H Garcia, R Kalyanaraman, and R Sureshkumar. "Novel self-organization mechanism in ultrathin liquid films: theory and experiment". In: *Physical Review Letters* 101.1 (2008), p. 017802 (cit. on p. 77).

[80] A Reisman, M Berkenblit, J Cuomo, and SA Chan. "The chemical polishing of sapphire and $MgAl_2O_4$ spinel". In: *Journal of The Electrochemical Society* 118.10 (1971), pp. 1653–1657 (cit. on p. 81).

[81] R Aeschlimann, F Gassmann, and TP Woodman. "The chemical polishing of magnesium aluminate spinel in pyrophosphoric acid". In: *Materials Research Bulletin* 5.3 (1970), pp. 167–171 (cit. on p. 81).

[82] RJ Needs and M Mansfield. "Calculations of the surface stress tensor and surface energy of the (111) surfaces of iridium, platinum and gold". In: *Journal of Physics: Condensed Matter* 1.41 (1989), p. 7555 (cit. on p. 86).

[83] TK Galeev, NN Bulgakov, GA Savelieva, and NM Popova. "Surface properties of platinum and palladium". In: *Reaction Kinetics and Catalysis Letters* 14.1 (1980), pp. 61–65 (cit. on p. 86).

[84] G Zhu, T Majdi, Y Shao, M Bugnet, JS Preston, and GA Botton. "Atomic structure and bonding of the interfacial bilayer between Au nanoparticles and epitaxially regrown $MgAl_2O_4$ substrates". In: *Applied Physics Letters* 105.23 (2014), p. 231607 (cit. on p. 88).